Interaction Effects and Disorder in Two-Dimensional Electron Systems

Matthias Baenninger

Fitzwilliam College

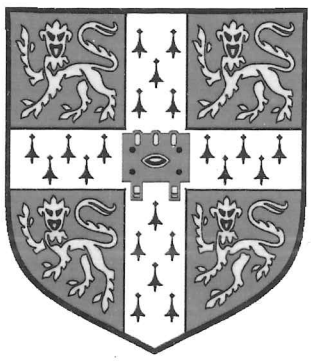

Dissertation submitted for the degree of
Doctor of Philosophy at the University of Cambridge

November 2007

Preface

This thesis concludes the work carried out at the Semiconductor Physics Group at the Cavendish Laboratory, University of Cambridge between October 2003 and November 2007.

Except where otherwise acknowledged, this dissertation is the result of my own work and includes nothing which is the outcome of work done in collaboration. It has not been submitted in part, or in whole, for any degree at this or another university. It is less than 60'000 words in length.

Matthias Baenninger, November 2007

Acknowledgements

My first thanks must go to my supervisor Prof Sir Michael Pepper, for giving me the opportunity to join the group and to work on an exciting topic. His enthusiasm, belief in my project, advice and encouragement have been extremely valuable.

I am greatly indebted to Dr Arindam Ghosh, who prepared the path for my experiments and who acted as my day-to-day supervisor throughout the largest part of my PhD. He introduced me to all the experimental techniques I needed, with knowledge, enthusiasm, commitment and patience. Our countless interesting and sometimes heated discussions greatly broadened my knowledge and sharpened my understanding of physics.

I would also like to thank both Mike and Arindam for giving me the chance for a five month visit at the Indian Institute of Science in Bangalore.

My experiments would not have been possible without the high quality wafers grown by Dr Ian Farrer, Dr Harvey Beere and Dr Paola Atkinson.

I greatly appreciated the readiness of the group members, from fellow students to post-docs and staff members, to help on many occasions with problems in the lab.

I am grateful to Dr Arindam Ghosh, Dr Ian Farrer and Dr Simon Hees for proof-reading this thesis.

During my PhD I was financially supported by the Sunburst Trust based at ETH Zurich, the EU funded COLLECT research network, the Cambridge Overseas Trust and in the fourth year by group funds.

Last but not least I would like to thank my family and friends from the group and college who have helped to keep my life in balance between work and leisure over the past four years.

Publications

The work described in this thesis has resulted in the following publications:

M. Baenninger, A. Ghosh, M. Pepper, H. E. Beere, I. Farrer, P. Atkinson and D. A. Ritchie
Local transport in a disorder-stabilized correlated insulating phase
Phys. Rev. B **72**, 241311(R) (2005)

M. Baenninger, A. Ghosh, M. Pepper, H. E. Beere, I. Farrer, P. Atkinson and D. A. Ritchie
Quantisation of hopping magnetoresistance prefactor in strongly correlated two-dimensional electron systems
doi:10.1016/j.physe.2007.08.099
Physica E, in press

M. Baenninger, A. Ghosh, M. Pepper, H. E. Beere, I. Farrer and D. A. Ritchie
Low-Temperature Collapse of Electron Localization in Two Dimensions
Phys. Rev. Lett. **100**, 16805 (2008)

Summary

This thesis reports an experimental study of transport on a mesoscopic length-scale in the localised regime of two-dimensional electron systems (2DES) with varying disorder. Devices with dimensions of a few microns were fabricated from modulation doped GaAs/AlGaAs heterostructures, where the strength of disorder was tuned by changing the width of the undoped spacer layer separating the 2DES from the charged dopants, which are the main source of disorder in these systems. The main motivation of the experiments was to study the interplay between electron-electron interactions and short-range disorder at low electron densities, while avoiding the impact of long-range charge inhomogeneities that are usually present in this regime.

Indeed, several new observations have been achieved with this approach: Chapter 5 reports an universal behaviour of hopping magnetoresistance, with evidence of the average hopping distance being equal to the average electron-electron separation, and a quantisation of the hopping prefactor in units of the quantum of resistance h/e^2. Chapter 6 discusses the temperature dependence of resistance. The main result is an apparent temperature driven metal-to-insulator transition with a crossover from activated transport at high temperatures to metallic transport at low temperatures. This observation persists to resistivities of several hundred times the quantum of resistance. In chapter 7 a new kind of resistance oscillations is reported, which appear as a function of electron density when a strong perpendicular magnetic field is applied. A strongly amplified pick-up of the Shubnikov-de Haas oscillation and a modification of the quantum Hall effect are reported in chapter 8. Furthermore, a new technique for measuring the electron density in mesoscopic 2DES is presented in chapter 4.

Contents

Chapter 1

Introduction

Ever since the first two-dimensional electron systems (2DES) were realised, they have been used extensively to investigate various theories and concepts of charge localisation. Anderson [1] and Mott [2, 3] pioneered the theoretical understanding of localisation, preparing the way for the seminal work by Abrahams *et al.* [4] on the scaling theory of localisation. This theory predicts that in two dimensions, all electron states are localised at zero temperature in presence of even infinitely small disorder.

These theoretical investigations were focusing on the single-particle localisation by disorder and did not take any significant electron-electron interactions into account. This was justified by early experimental studies of transport in 2D, where an insulating phase was observed and it was found that the transport behaviour could very well be described by a single-particle picture [5–7].

More recently, the focus has turned to the investigation of electron-electron interaction effects. A first success was the experimental observation of the Coulomb gap predicted by Efros and Shklovskii [8–10]. However, the Coulomb gap is only a modification of the single-particle density of states and does not introduce a fundamental change to the ground state of a 2DES and, in particular, its insulating nature.

In the limit of very strong interactions and weak or absent disorder, the formation of a Wigner crystal is expected [11, 12]. In this phase electrons are not localised by disorder, but by their mutual repulsion due to the Coulomb

force. The transition to the Wigner crystal is determined by the interaction parameter $r_s = E_C/E_F$, with E_C the Coulomb interaction energy between electrons and E_F their Fermi energy. For 2DES one finds $r_s = 1/a_B^* \sqrt{\pi n_s}$, with a_B^* the effective Bohr radius and n_s the electron sheet density. Hence, with decreasing electron density, the strength of the Coulomb interaction relative to the kinetic energy of the electrons becomes larger, eventually leading to the formation of the Wigner crystal. Experimentally, indications of a crystalline electronic phase have been reported [13–18], the approach mostly being a minimisation of disorder and/or application of a strong perpendicular magnetic field. However, conclusive evidence is still lacking.

The intermediate regime, where both disorder and electron-electron interactions are equally important, is very challenging to study theoretically and experimentally and is still not well understood.

It is of particular interest if, in presence of moderate disorder and electron-electron interactions, the scaling theory of localisation still holds. Despite a large amount of work, especially around a putative metal-insulator transition in 2D reported by Kravchenko *et al.* [19], this question is still controversial.

On the other hand, moderate disorder might be able to enhance interaction effects. A possible mechanism is that the disorder quenches the kinetic energy of the electrons, effectively increasing the interaction parameter r_s. This could lead to a stronger impact of electron-electron interactions at higher electron densities. Indeed, a possible formation of a Wigner crystal has been suggested in presence of disorder at much higher electron density than in the disorder-free case [20].

This thesis presents a study of transport in 2DES under systematic variation of the strength of both disorder and interactions. It is an attempt to fill the gap in experimental investigation of the regime of intermediate disorder and electron-electron interactions. The following section discusses the problems in previous investigations of this kind and introduces a new approach to overcome those problems: Mesoscopic two-dimensional electron systems in modulation doped GaAs/AlGaAs heterojunctions.

1.1 Mesoscopic 2DES in Modulation Doped GaAs/AlGaAs Heterostructures

A crucial property of disorder is the characteristic length-scale of its potential fluctuations. If the disorder is mainly long-range, the system becomes increasingly inhomogeneous at low electron densities. This can lead to formation of puddles of electrons separated by depopulated areas, where transport occurs according to classical percolation laws, masking any possible interaction effects between electrons [21]. Such charge inhomogeneities have been known for a long time to have a large impact on transport, e.g. in Si-MOSFETs [22], high mobility modulation doped GaAs/AlGaAs heterojunctions [23] and even undoped GaAs/AlGaAs heterojunctions [24]. An experimental approach for investigating interaction effects in presence of disorder should minimise the effects of long-range disorder and focus on short-range fluctuations.

In modulation doped GaAs/AlGaAs heterojunctions, the disorder mainly comes from the remote charged ions in the doping layer, and the strength of disorder depends strongly on the width δ_{sp} of the undoped spacer layer between 2DES and doping layer. The possibility of changing the strength of disorder by varying δ_{sp} provides a powerful tool in the investigation of disorder effects.

In theoretical treatment, an entirely random distribution of the dopants is generally assumed, giving an uniform spectral density of the potential fluctuations with only the fluctuations of length-scale $< \delta_{sp}$ exponentially damped in the 2DES [25]. However, recent imaging of the disorder landscape of 2DES suggests that the dominant length-scale in modulation doped GaAs/AlGaAs heterojunctions is, in fact, greater than $0.5\,\mu\text{m} \gg \delta_{sp}$ [26, 27]. This strongly indicates that in these systems long-range disorder dominates on a macroscopic length-scale.

In consideration of this problem, the experimental approach used in this PhD differs in two crucial ways from previous studies of charge localisation in 2D:

(1) Mesoscopic 2DES have been used, extending only over $0.5\,\mu\text{m}$ to a few microns, thereby strongly reducing the impact of long-range disorder and allowing a focus on the short-range fluctuations of order δ_{sp}. This is shown

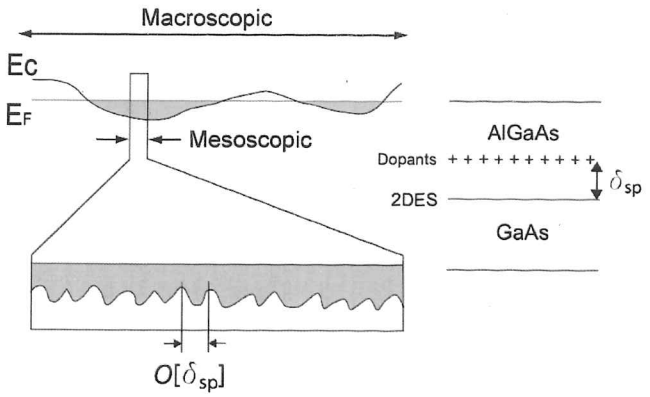

Figure 1.1: Schematic of dominant disorder on macroscopic and mesoscopic length-scale: While in a macroscopic device, long-range disorder leads to an inhomogeneous electron distribution, a mesoscopic device avoids or strongly reduces this problem. The mesoscopic 2DES is homogeneous and the dominant disorder is of short length-scale.

schematically in Fig. 1.1.
(2) Instead of outright minimisation, the strength of background potential fluctuations has been tuned systematically by varying the spacer width.
Furthermore, for a given spacer width the electron density and, therefore, interaction parameter r_s can be changed with a metallic topgate.

A very simple, but nevertheless revealing experiment is shown in Fig. 1.2. It compares the conductivity σ as a function of n_s for a macroscopic device with dimensions $W \times L = 100\,\mu\text{m} \times 900\,\mu\text{m}$ and a mesoscopic device ($W \times L = 8\,\mu\text{m} \times 3\,\mu\text{m}$) from the same wafer. Here, the width W and length L are the dimensions perpendicular and parallel to the current direction, respectively.

One can immediately see that a sharp downturn of conductivity starts at $n_s > 3 \times 10^{10}\,\text{cm}^{-2}$ in the macroscopic device (Fig. 1.2 a)). In the mesoscopic device (Fig. 1.2 b)), the downturn occurs at much lower electron density. This allows for transport measurements in the mesoscopic device at almost three times lower densities, making a new regime of disorder and interaction strength accessible in transport experiments.

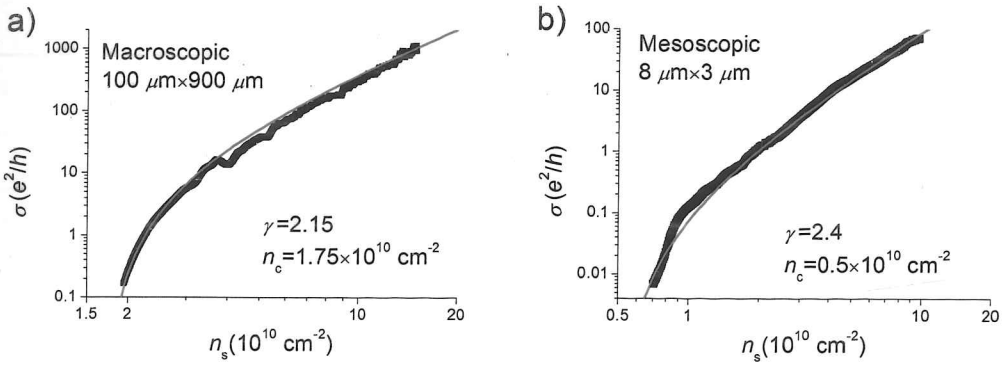

Figure 1.2: Conductivity σ as a function of electron density n_s at T=300 mK for a macroscopic (A77Lc) and a mesoscopic (A77a) device from the same wafer. The solid lines are fits of the percolation scaling relation $\sigma \propto (n_s - n_c)^\gamma$. The data from the macroscopic device shows excellent agreement, while the mesoscopic device shows a qualitatively different behaviour and, additionally, a freeze-out of transport at much lower n_s.

Furthermore, σ in the macroscopic device shows excellent classical percolation-like scaling $\sigma \propto (n_s - n_c)^\gamma$ with $n_c \cong 1.73 \times 10^{10}\,\mathrm{cm}^{-2}$ and $\gamma \cong 2.15$ (solid line in Fig. 1.2 a)). The value of γ is in reasonable agreement with the theoretical prediction of 4/3 and close to previously reported experimental values [24]. This confirms an inhomogeneity driven percolation transition in the macroscopic device.

By contrast, for the mesoscopic device, fitting of a scaling expression was found to be difficult. An attempted fit is shown as the solid line in Fig. 1.2 b) with a poor agreement. The parameters in this fit are $n_c \cong 0.5 \times 10^{10}\,\mathrm{cm}^{-2}$ and $\gamma \cong 2.4$. However, they should not be considered physically meaningful, as the scaling relation is clearly not the right expression to describe the behaviour of σ in the mesoscopic device. This disparity from the macroscopic device indicates a different localisation mechanism on a mesoscopic length-scale and raises hopes for attaining new insights into the nature of transport and localisation from experiments in this regime.

In the remaining parts of this thesis, I hope to convince the reader that the investigations of transport on a mesoscopic length-scale have, indeed, lead to the discovery of several exciting new phenomena in 2DES.

Chapter 2

Fundamentals: 2D Electron Systems in Semiconductors

This chapter tries to give a summary of previous work on two-dimensional electron systems (2DES) that is of relevance for this thesis. It treats both theory and experiments. The theoretical discussions give a rather general overview on 2DES with a focus on localisation and interaction effects, while more specific theory is included in the respective later chapters of the thesis. The experiments described represent by no means a complete history of experimental work done on 2DES but are only meant to give the background necessary to put the results presented in the thesis into perspective.

2.1 General Considerations

If electrons are confined in a narrow potential well, their motion in one dimension is restricted to discrete energy levels. If the separation between these energy levels is large compared to other relevant energies, in particular the thermal energy, the electrons will be frozen into the ground state and no motion in this dimension will be possible. If this is the case, one talks of a two-dimensional electron system.

2.1.1 Energy Dispersion and Density of States

The movement of an electron in such a 2DES can be modelled in a simple single particle picture: The dispersion relation of an electron in a quantum well without external field is $E = E_n + \frac{\hbar^2 k_\parallel^2}{2m^*}$ where E_n is the subband energy of the quantum well, $\boldsymbol{k}_\parallel$ the two dimensional electron wave vector, and m^* the effective electron mass. The subband energy depends on the exact shape of the confining potential, e.g. for a square potential well with infinitely high walls the analytical solution is $E_n = \frac{n^2 h^2}{8m^* d^2}$ with d the width of the well.

In three dimensions the density of states (DOS) is given by $N_{3D} = \frac{m\sqrt{2mE}}{\pi^2\hbar^3}$. In two dimensions, the density of states changes drastically and becomes a constant $N_{2D} = \frac{m^*}{\pi\hbar^2}$ for any given subband. Taking all subbands into account, this leads to a step function as shown in Fig. 2.1 with the steps occurring at the subband energies E_n. In the limit of weak confinement and, hence, small energy quantisation, the step function approaches the 3D DOS. All experiments presented in this thesis were carried out in the regime where only one subband was occupied. For this situation, the Fermi energy at $T = 0$ can easily be calculated from the DOS and one finds $E_F = \frac{\pi\hbar^2 n_s}{m^*}$. Through the relation $E_F = \frac{\hbar^2 k_F^2}{2m^*}$ the Fermi wave number $k_F = \sqrt{2\pi n_s}$ is derived. The Fermi velocity $v_F = \hbar k_F / m^*$ and the Fermi temperature $T_F = E_F / k_B$ with k_B the Boltzmann constant follow directly.

Taking disorder and thermal broadening into account the perfect step function does not hold. It loses its sharpness with the DOS being reduced at energies just above the step and increased just below. This leads to a finite number of states even below the lowest subband energy. These states are called the band tail. While higher energy states can be extended and mobile, the states in the band tail will generally be localised. Localisation will be discussed in more detail in Sect. 2.3. Additional modifications to the density of states can arise from interaction effects between electrons, these will also be discussed later (Sect. 2.3.3).

2.1.2 Mobility

The mobility of an electron is defined as $\mu = e\tau/m^*$ with e the electron charge, m^* the effective mass, and τ scattering or momentum relaxation time of the

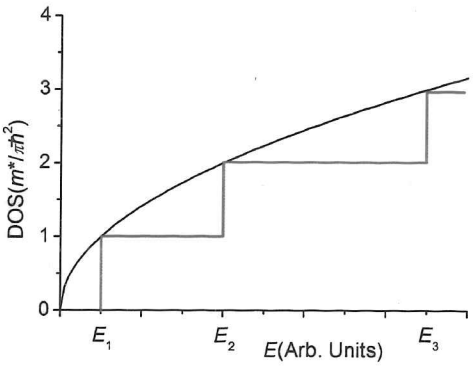

Figure 2.1: Density of states in two dimensions in a clean system at zero temperature. The black parabolic line indicates the DOS in a film of large thickness.

otherwise freely moving electron. In the Drude model this leads to the expression for the conductivity $\sigma = \frac{n_s e^2 \tau}{m^*} = n_s e \mu$. The mobility is an important quantity in the classification of 2DES, it is the most common way of specifying the quality of a 2DES. The scattering rate and, hence, the mobility depends strongly on the disorder. The lower the disorder, the higher the mobility. However, screening of the disorder potential by the electrons in the 2DES itself can hugely reduce the scattering and the mobility becomes a strongly electron density dependent quantity. For a comparison of wafers, the mobilities should therefore be compared at a constant electron density.

There are various sources of disorder and, hence, scattering, the most important ones are listed in Sect. 2.2.3. If the different scattering processes are independent of each other, the total scattering time τ can be calculated using Matthiessen's rule [28]:

$$\frac{1}{\tau} = \sum_i \frac{1}{\tau_i}. \tag{2.1}$$

The mobility is only well defined in the regime of extended states, i.e. freely moving electrons that only scatter occasionally, leading to a well defined scattering time τ. In the localised regime, where most of the experiments in this thesis were done, it does not make much sense to talk about the electron mobility since electrons are immobile and scattering can actually even increase

transport. Nevertheless, the mobility of a 2DES at higher n_s can give an estimate of the strength of disorder that keeps its significance even in the low density regime.

2.1.3 Interaction Parameter

The interaction parameter is defined as $r_s = 1/a_B^* \sqrt{\pi n_s}$ with $a_B^* = \frac{4\pi\hbar^2\epsilon\epsilon_0}{m^* e^2}$ the effective Bohr radius. This means that r_s is the radius of a circle that encloses each electron if they were arranged in a hexagonal lattice in units of a_B^*. Another meaning of r_s becomes clear when comparing the Fermi energy $E_F = \frac{\pi\hbar^2 n_s}{m^*}$ in two dimensions with the Coulomb interaction energy $E_C = \frac{e^2\sqrt{n_s\pi}}{4\pi\epsilon\epsilon_0}$. One can easily show that

$$r_s = \frac{1}{a_B^* \sqrt{\pi n_s}} = \frac{E_C}{E_F}. \tag{2.2}$$

This means that r_s gives a measure of the effective Coulomb interaction between electrons, i.e. the Coulomb energy compared to the Fermi and, hence, kinetic energy of the electrons. The proportionality of r_s to $1/\sqrt{n_s}$, therefore, means that Coulomb interaction effects should be stronger at lower electron densities.

2.2 Modulation Doped GaAs/AlGaAs Heterostructures

There are several ways of realising two-dimensional electron systems in semiconductors. Most widely used are silicon metal oxide semiconductor field effect transistors (Si-MOSFET) and GaAs/AlGaAs heterostructures. The second approach was used in this work and in this section, its theoretical prerequisites are given.

2.2.1 Bandstructure

The two semiconductors AlAs and GaAs are both arranged in a zincblende structure and they have a lattice mismatch of 0.2% at most. This enables the

growth of these two materials on top of each other with negligible strain. GaAs and AlAs have different band gaps and E_{gap} of the alloy $Al_xGa_{1-x}As$ varies as [29]

$$E_{\text{gap}} = (1.42 + 1.25x)\,\text{eV} \qquad \text{x} < 0.45 \tag{2.3}$$

The fact that for $x < 0.4$ $Al_xGa_{1-x}As$ is a direct gap semiconductor simplifies both theoretical and experimental investigations. These properties enable the realisation of arbitrary potential shapes by varying the concentration of aluminium. With modern growth technologies such as molecular beam epitaxy (MBE), layer thickness and composition can be controlled almost perfectly.

Two-dimensional electron systems (2DES) can be realised by bringing a bulk of GaAs in contact with a bulk of $Al_xGa_{1-x}As$. Generally, an Al content of $x = 0.33$ is used, providing a large conduction band offset but keeping the band gap direct. In modulation doped heterostructures the wide gap material AlGaAs is doped, but separated from the heterojunction by a spacer of undoped AlGaAs. In bulk-doping the dopants are distributed over an extended layer of AlGaAs. Alternatively, in δ-doping the dopants are deposited in one monolayer but may spread out into a few monolayers by diffusion. The most commonly used dopant is silicon. In order to keep the Fermi levels aligned, electrons diffuse from the doping layer to the narrow gap material GaAs. This leads to the formation of a positively charged layer in the AlGaAs side, which gives rise to a strong electric field causing a band tilting in the GaAs and the formation of a triangular potential well confining a two-dimensional electron system at the GaAs-AlGaAs interface. A schematic of a bandstructure of a δ-doped heterojunction is shown in Fig. 2.2. In 2DES formed at the heterointerface the electrons are free to move in the plane of the interface but are confined in the perpendicular direction.

2.2.2 *DX*-Centres

Silicon donor atoms in AlGaAs are not necessarily all positively charged. They can be in three different states, two shallow, hydrogenic donor states (d^+, d^0) and one deep donor state (DX^-), called *DX*-centre (Fig. 2.2). The *d* states are the usual donor states, ionised (d^+) or in the neutral state with a loosely bound electron (d^0). A *DX*-centre is a d^+ binding two electrons.

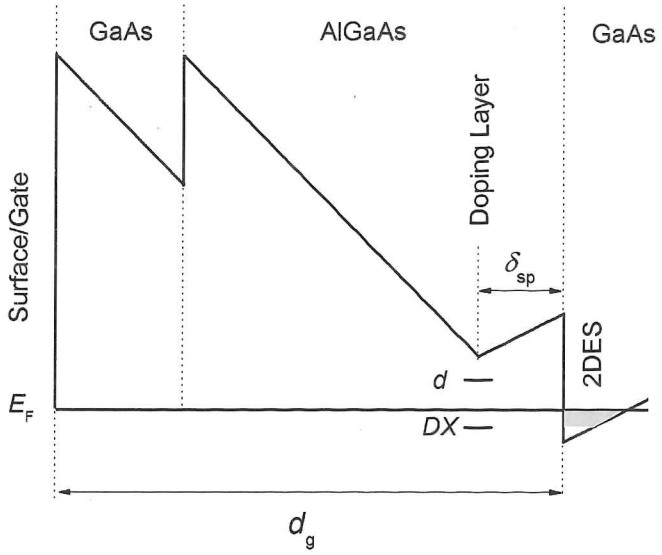

Figure 2.2: Band diagram of a δ-doped heterojunction of total depth d_g and spacer width δ_{sp} between doping layer and 2DES. Shallow (d) and deep (DX) donor states are indicated.

The "reaction" $2d^0 \rightarrow d^+ + DX^-$ is energetically favourable when it involves a defect formation with a Si-donor being displaced along the $\langle 111 \rangle$ direction away from the substitutional site [30–33]. These states lie in the $Al_xGa_{1-x}As$ band gap for $x \geq 0.2$. An important feature of DX-centres is the existence of a large barrier for the transition from and to the shallow states. This leads to an experimentally important property, namely a freeze-out temperature below which DX-centres can neither be formed, nor destroyed. Experimentally, this freeze-out temperature is found to be $T_{DX} \approx 130\,\mathrm{K}$ for $x = 0.37$ [33]. If the cooldown of the device is not too fast, one can assume that the vast majority of donors are either in the d^+ or DX^- state and no loosely bound electrons in d^0 exist, which are prone to cause switching events resulting in experimental instabilities. An electrostatic change at low temperatures (change of gate voltage) can alter this situation, e.g. applying a positive gate bias can lead to an accumulation of additional electrons in the dopant layer. These cannot be bound in DX-states anymore and flood the shallow donor states. On the

other hand, illumination after the cool-down can excite electrons out of the DX-centres, leading to photo-conductivity which is persistent since electrons cannot get trapped in DX-centres again.

Depending on details of the heterostructure and gate voltage during the cooldown, a rather large number of donor electrons remain in the doping layer, forming DX-centres. This gives rise to an interesting property of the doping layer: Donor atoms are randomly distributed and, therefore, if all of them are ionised, cause a random background disorder potential in the 2DES. However, this need not be the case if donors are both in d^+ and DX^- states. Since DX-centres are mobile at high temperatures they can rearrange themselves in order to minimise the electrostatic energy, thereby producing a degree of correlation of the charges in the doping layer and screening the disorder potential caused to some extent. Experimentally, this effect has been shown to lead to a strong enhancement of the mobility of two-dimensional electron systems [33]. The impact of remaining electrons in the dopant layer and possible correlations between them are further discussed in Sects. 3.3.3 and 9.2.1.

2.2.3 Disorder

Since the investigation of the interplay between disorder and electron-electron interactions forms a main part of this thesis, the sources and strength of disorder in GaAs/AlGaAs heterostructures deserve a closer look. Disorder is represented by any disturbance of the periodic potential of the GaAs crystal in the 2DES. There are various effects that can cause such disturbances and the most important ones are:

- Phonon scattering: Phonons are lattice vibrations that distort the lattice and can scatter electrons. This effect depends strongly on temperature and is not relevant at the low temperatures at which our experiment were carried out.

- Surface roughness: The surface between GaAs and AlGaAs is not perfectly flat. However, under good growth conditions very smooth surfaces can be achieved. Additionally, the closely matching lattice constants of GaAs and AlGaAs keep distortions arising from strain at the surface very small.

- Neutral impurities: A neutral impurity, such as Al in GaAs, distorts the lattice symmetry. In GaAs/AlGaAs heterostructures, where the 2DES is in the GaAs, grown without any intentional Al, this effect is very small. Even if some aluminium atoms diffuse into the GaAs, their impact is small due to their charge neutrality. Neutral impurities can become an important source of disorder if the 2DEG is formed in AlGaAs or any other alloy. Due to the large number of randomly distributed substituting atoms, the lattice distortion can become strong in spite of the neutrality of the impurities. The electron scattering caused by this phenomenon is called alloy scattering.

- Charged background impurities: During the growth process ionised donor and acceptor atoms are unintentionally incorporated into the otherwise undoped layers. Due to their charge, they can cause strong disturbance if they are close to the 2DES. However, in state-of-the-art MBE systems, the number of these impurities is so small (estimated 10^{14}cm^{-3}), that their impact in negligible in doped heterostructures.

- Charged donors in doping layer: Even though, in modulation doped heterostructures, the intentionally placed donors in the doping layer are separated from the 2DES, due to their number, they are the main source of disorder in the heterostructures used in this work [23, 33–39].

The fact that the dominant source of disorder arises from the dopants in the doping layer provides a tool for a investigation of the influence of varying disorder strength on the properties of the 2DES: By varying the width δ_{sp} of the spacer layer, the degree of disorder in the 2DES can be varied systematically, a smaller spacer width leading to stronger disorder.

Most theoretical [34–36] and experimental [23, 37, 38] studies of disorder effects investigate the mobilities in the high density regime with extended electron wave functions, where the mobility proves to be a good measure of the influence of disorder, since the mobility is reduced with increased disorder scattering. Fig. 2.3 shows the effect of a varying spacer width in terms of the mobility in δ-doped heterostructures at constant electron and doping density. A clear decrease in the mobility is seen as the spacer width is reduced.

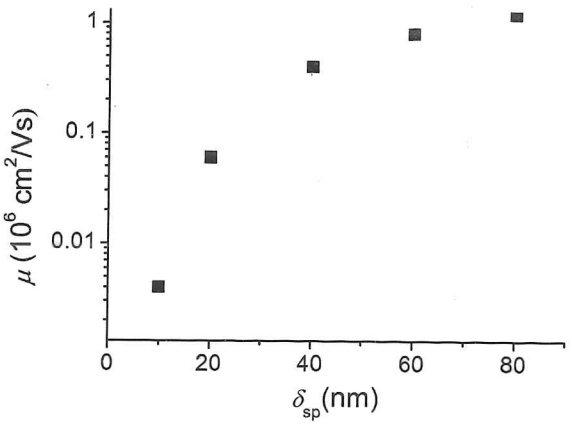

Figure 2.3: Mobility as a function of spacer width $\delta_{\rm sp}$ in δ-doped heterostructures at constant electron density $n_{\rm s} \approx 9\times10^{10}\,{\rm cm}^{-2}$ and doping concentration $n_\delta \approx 2.5 \times 10^{12}\,{\rm cm}^{-2}$. [Data provided by Dr. Arindam Ghosh]

In this thesis, the focus is on the investigation of disorder in the localised and interacting regime of 2DES where the mobility is not a meaningful quantity. However, the results of mobility investigations and, in particular, the dependence of μ on $\delta_{\rm sp}$ is relevant in the low density regime as well. It can be assumed that the relevant source of disorder comes from the doping layer as well and, hence, that the disorder strength strongly depends on the spacer width. In fact, experiments show that the influence of the spacer width becomes stronger with decreasing density within the extended regime [23]. Efros *et al.* studied theoretically the influence of the disorder arising from the dopant ions in both the linear and non-linear screening regime [39]. They considered that the unscreened potential arising from the dopant layer is damped exponentially on a length scale $R < \delta_{\rm sp}$ but all harmonics with a wavelength greater than $\delta_{\rm sp}$ contribute similarly to the potential. This leads to a logarithmic divergence of the bare mean square potential with system size L, $\langle F_{\rm b}^2 \rangle \propto C \log \frac{L}{2\delta_{\rm sp}}$, with C the average donor concentration. Electron screening removes this divergence. In the linear screening regime, the electron concentration is large compared to the changes in concentration caused by the fluctuations of the bare potential. Under this condition, the screened potential is $\langle F^2 \rangle \propto C/\delta_{sp}^2$

with a much smaller prefactor than the unscreened case. If the electron density fluctuations are not small compared to the average n_s, only wavelengths $R \gg R_c$ of the disorder are screened linearly. Here, $R_c = \sqrt{C}/n_s$ is the nonlinear screening length. Disorder on a length scale $R \ll R_c$ is screened poorly. In this regime, an analytical expression of the screened potential fluctuation is not given, but numerical calculations confirm the importance of δ_{sp}.

If correlations between charges in the doping layer exist, the donor concentration C has to be replaced with an effective reduced concentration C', and long range fluctuations may be suppressed [25].

2.3 Single Particle Localisation in Weakly or Non-Interacting 2DES

In the early stages of quantum mechanical studies of electronic behaviour in disordered crystals, electrons were generally assumed to be extended and transport properties were calculated by considering the scattering of Bloch waves by impurities. However, it soon became clear that this was not adequate in case of strong disorder and a different treatment was required.

2.3.1 Anderson Localisation and the Mobility Edge

In 1958, considering three dimensional systems, Anderson pointed out that the electron wave function could be fundamentally different from a Bloch state if disorder was sufficiently large [1]. He proposed that in very strong disorder the wave function become localised in that the envelope of the wave function decays exponentially from some point in space, i.e. $|\Psi(\mathbf{r})| \sim \exp(|\mathbf{r} - \mathbf{r}_0|/\xi)$ with ξ the localisation length.

He started from the assumption of randomly distributed sites with randomly distributed energies within a characteristic width W. Between the sites there is an interaction parameter $V_{ij}(r_{ij})$ which transfers carriers from one site to the next. Anderson showed that if $V(r)$ falls off fast at large distances, and if the average value of V is small enough compared to W, wave functions are

localised exponentially (Fig. 2.4). More quantitatively, he derived a critical value for W/V above which no transport occurs at all.

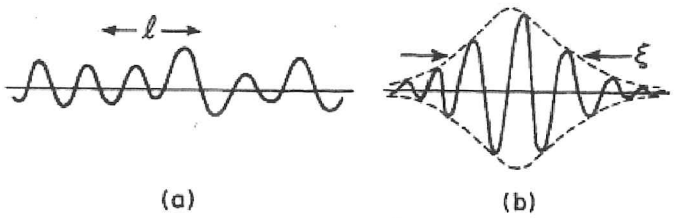

Figure 2.4: Comparison of extended state with mean free path l (a) and localised wave function with localisation length ξ (b). [From Ref. [40]]

The physical reason for this can be understood quite easily: On one hand, orbitals nearby in space with a significant wave function overlap, are generally very different in energy, so that admixture is small because of the large energy denominator. On the other hand, states that are close in energy are in general far apart in space, and have an exponentially small wave function overlap. Hence, in the strongly disordered limit, the states will be exponentially localised. In fact, it turns out that it is much easier to establish the existence of localised states than extended ones, as will be discussed in later sections.

Following Anderson's reasoning, one expects the states in the band tails to be localised, since these are states formed from localised orbitals bound in deep potential fluctuations. The states in the band centre have the best chance of being extended. Mott proposed that as a function of energy, the states must change their character from being localised to being extended [40]. The critical energy at which this change occurs is called the mobility edge, marking the transition between a metal and an insulator. However, for the two dimensional case, the scaling theory of localisation discussed in the next section calls the existence of a metallic state into question and predicts that all states are localised.

2.3.2 Scaling Theory of Localisation

This section roughly follows reference [40]. Scaling theory tries to understand localisation by looking at the behaviour of the dimensionless conductance $g = G/(e^2/\hbar)$ as a function of system size L. For $L \gg l$, with l the mean free path defined by the length over which the phase of the wave function fluctuates by about 2π, $g(L)$ has two asymptotic forms depending on the microscopic disorder. For a metallic state, the size dependence of the conductance is given by Ohm's law

$$g(L) = \sigma L^{d-2}, \tag{2.4}$$

with d the dimension and $\sigma = ne^2\tau/m$ derived by conventional transport theory. However, in the localised regime, transport occurs by an electron hopping from an occupied state to a unoccupied one with almost the same energy. In this case, for $L \gg \xi$ (ξ generally being larger than l), a completely different, non-Ohmic scale dependence applies:

$$g(L) \propto \exp(-L/\xi). \tag{2.5}$$

As L increases, $g(L)$ evolves smoothly, eventually going over to either form (2.4) or (2.5), depending on the microscopic disorder.

Abrahams *et al.* [4] argued that the logarithmic derivative of conductance $\beta(g) = d\ln g/d\ln L$ is a function of g alone. The idea is that the change in effective disorder when the system becomes a little bigger is determined by its value at the previous length scale, the only measure of this effective disorder being the conductance. They derived the scaling curves for d=1, 2, and 3 shown in Fig. 2.5.

For the case of two dimensions, interpretation of the diagram leads to a surprising conclusion: No truly extended electronic states are possible! Since $\beta(g) < 0$ an increase in L always leads to a decrease in β, asymptotically approaching $\beta(g) \sim \ln(g/g_c)$, with g_c a characteristic dimensionless conductance. This asymptotic behaviour is equivalent to condition (2.5) and predicts that for large enough L, even for small microscopic disorder, only localised behaviour is possible.

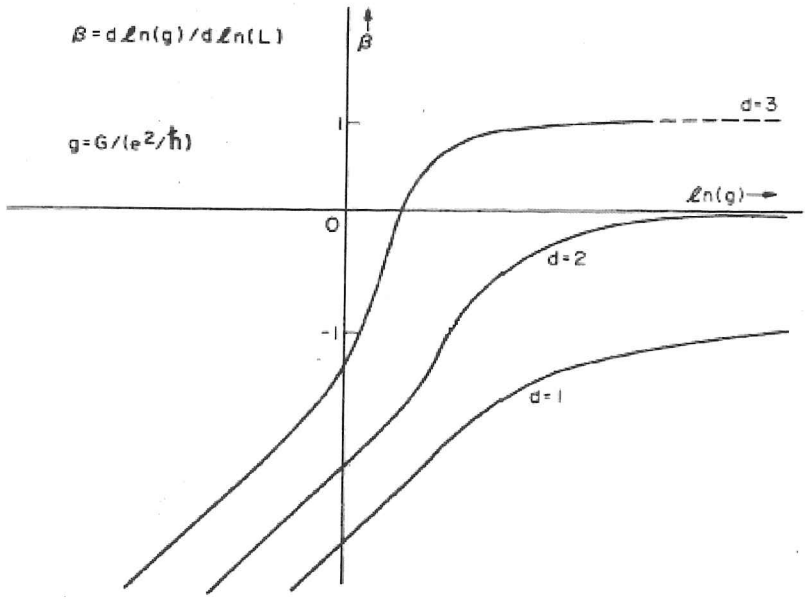

Figure 2.5: The scaling function $\beta(g)$ vs. the dimensionless conductance g for different dimensions. [From Ref. [40]]

2.3.3 Fermi Glass and the Coulomb Gap

The previous discussion leads us to the following picture for the ground state of a disordered, weakly or non-interacting 2DES: The disorder determines the electron states, which, according to the scaling theory are all localised. The available states with energies below the Fermi energy are occupied, while states above the Fermi energy are empty. This leads to a random distribution of occupied, localised single-electron states. This state is called Fermi glass.

Efros and Shklovskii showed that Coulomb interactions introduce a gap in the density of states at the Fermi level, the so-called Coulomb gap [8]. The qualitative reasoning for this is as follows: Consider two states i and j which are occupied and unoccupied, respectively, in the ground state, i.e. $E_\mathrm{i} < E_\mathrm{F} < E_\mathrm{j}$, with E_F the Fermi energy. If the electron occupying state i is removed, the energy of state j is lowered by e_ij, the Coulomb energy arising on state j due to the presence of an electron in state i. If $E_\mathrm{j} - e_\mathrm{ij} < E_\mathrm{i}$, it would now be energetically better for the electron to occupy state j, i.e. the energy of the system could be lowered by an electron moving from site i to j, which is a

contradiction since the system was assumed to be in the ground state. This means that the separation in energy between two states above and below the Fermi energy must be larger than their Coulomb interaction energy, i.e. the density of states at the Fermi level disappears. The introduction of a Coulomb gap does not alter the picture of single particle localisation. However, it has an influence on the low-temperature transport properties, which will be discussed in Sect. 2.6.

2.4 Strongly Interacting 2DES in the Absence of Disorder

Before moving on to the problem of strongly interacting electrons in the presence of background disorder, a summary of the case of complete absence of disorder is given. The advantage of studying disorder free systems is that they are less difficult (but by no means easy) to treat. The disadvantage, of course, is that their relevance for real systems is limited.

2.4.1 Wigner Crystal

Zero Magnetic Field

As early as 1934, Wigner predicted that at low densities, electrons in a metal should form a crystal [11], which is now called Wigner crystal (WC). The physics behind this phenomenon is essentially the competition between the classical Coulomb repulsion and the quantum mechanical zero-point energy. On one hand, electrons can reduce their Coulomb energy by avoiding each other through the formation of a crystal with localised individual wave functions. On the other hand, localisation of the wave function inevitably leads to an increase of the kinetic energy because of Heisenberg's uncertainty principle. Wigner showed that for low enough densities, the reduction in Coulomb energy wins over the increase in kinetic energy.

Tanatar and Ceperley used numerical methods to get a quantitative estimate of the density at which the transition between the liquid and crystal

phase occurs [12]. They compared the ground state energies between a liquid and a solid phase using a fixed-node quantum Monte Carlo (FN-QMC) method and found that the solid phase has a lower energy for $r_s \geq 37 \pm 5$. For an ultra high mobility (7×10^5 cm^2/Vs) two-dimensional hole system, a metal insulator transition was later observed at $r_s = 35.1 \pm 0.9$ and interpreted as the melting point of a Wigner crystal [15].

In QMC simulations the algorithm is fed with a guiding wave function (GWF) that should be as close as possible to the ground state of the system. The GWF is then projected onto the true ground state of the system. A serious challenge in this approach for fermions is the "fermion sign problem", which leads to an exponential decrease of the signal-to-noise ratio with increasing system size or decreasing temperature (see e.g. Refs. [41, 42]). A way to tackle this problem is the FN-QMC approach which applies the restriction to the algorithm that the sign of the wave function and, hence, its nodal structure remain unchanged. The disadvantage is that in calculations as reported in Ref. [12], where the energies of a liquid and a solid state are compared, one might overlook a third phase with even lower energy, which has a different nodal structure than either of the two GWFs.

Finite Magnetic Field

It was first pointed out by Lozovik and Yudson in 1975 that a strong perpendicular magnetic field might lead to crystallisation of a 2DES at much higher electron densities than it would be the case in zero field [43]. Their reasoning was that a crystal is stable when the amplitude Λ_0 of the zero-point oscillations of the electrons fulfils the criterion $\Lambda_0 \lesssim \gamma a_0$ with γ an empirical constant and a_0 the lattice constant. The effect of a strong perpendicular magnetic field is to limit Λ_0 to the magnetic length $l_B = \sqrt{\hbar/eB_\perp}$, thereby stabilising the crystal. This simple picture is instructive, but otherwise mainly of historical importance, since it does not take the fractional quantum Hall effect (FQHE) state into account, which was discovered several years after publication of this work and changes the situation significantly.

To get a quantitative estimate for the field at which crystallisation for a given electron density occurs, one has to compare the energy of the WC (E_{WC}) with that of the FQHE liquid (E_L) proposed by Laughlin [44]. This was done

by Levesque *et al.* [45]. They calculated E_{L} to a very small error with a Monte Carlo method and compared it with a Hartree-Fock approximation of E_{WC}. It was found that the WC state has a lower energy than the FQHE state for $\nu < 1/9$, where $\nu = \frac{n_{\mathrm{s}}}{\frac{e}{h} \cdot B_{\perp}}$ is the Landau level filling factor (see Sect. 4.1.3). An improvement of this estimate was calculated soon after that, using E_{L} from Ref. [45] but a more accurate variational approach for E_{WC}, which included particle correlations. This revealed the condition $\nu \lesssim 1/7$. This value should be essentially exact, with the caveat that disorder is not taken into account. However, in the meantime experimental evidence of FQHE states at $\nu < 1/7$ has been found, which is not entirely understood [46]. Nevertheless, it is widely assumed that a Wigner crystal is formed at sufficiently low filling factor and between FQHE states.

2.4.2 More Exotic Phases

Katomeris *et al.* and Németh *et al.* performed exact diagonalisation calculations for $N = 3$ and 4 electrons on a two-dimensional 6×6 square lattice with periodic boundary conditions and nearest neighbour hopping [47, 48]. They found that for an intermediate range of r_{s} a phase that is neither fully crystalline nor liquid is formed. Of N particles, $N - 1$ were forming a nearly solid assembly, while the remaining particle was delocalised. The range in which this new phase was formed, was $10 < r_{\mathrm{s}} < 28$ for $N = 4$, and $6 < r_{\mathrm{s}} < 180$ for $N = 3$. For the case of $N = 4$, the influence of disorder was studied by introducing perturbations in the form of a certain randomness of the substrate lattice sites. Weak disorder did not qualitatively change the situation, but in stronger disorder, a phase with localised and delocalised electrons coexisting was no longer observed. The authors proposed that the observed phase coexistence was the mesoscopic trace of the supersolid phase proposed by Andreev and Lifshitz [49], which will be discussed in some more detail in Sect. 6.2.1. Of course, the extremely small number of electrons makes the relevance of these calculation in macroscopic systems debatable. However, the work nevertheless gives some indication that phases other than Wigner crystal and Fermi liquid might exist in clean or low disorder 2DES.

Waintal *et al.* chose a different approach to study intermediate phases [42, 50]: They used FN-QMC but apart from the usual crystalline (localised orbitals) and liquid-like (plane waves) GWF, they also investigated a hybrid phase built from the Bloch states of a triangular lattice, i.e. it is liquid-like in that it is made from plane waves but it has the symmetry of a Wigner crystal. This intermediate phase showed a lower energy than both liquid and crystalline phase for $r_s > 31.5 \pm 0.5$ up to the largest value studied ($r_s = 70$). A physical interpretation of this hybrid phase is not straightforward. While the advantage over a crystalline phase can be understood quite easily in terms of a reduction in kinetic energy due to the delocalised nature, the advantage over a liquid phase is more intricate, but is related to the change in symmetry of the wave function. The work establishes the existence of an intermediate phase, but does not allow very deep insight into the nature of the phase. However, it is clear that the hybrid phase cannot be directly associated with the supersolid phase discussed above, as no discrepancy between number of electrons and lattice sites was observed. This does not mean that, in principle, an incommensurate crystal phase with an even lower energy cannot exist, although the author of Ref. [42] states that he tried to find such a GWF without success.

Spivak *et al.* [51, 52] argue that in a clean (i.e. disorder free) 2DES adjacent to a ground plane, a direct transition from a Wigner crystal to Fermi liquid is forbidden at zero temperature and that an intermediate phase with coexistence of spatially separated liquid and crystal always occurs. This phenomenon arises from the tendency for phase separation originating from the first-order phase transition between Fermi liquid and Wigner crystal as a function of n_s. While in neutral systems a first-order transition favours a global phase separation, this is not possible in charged systems due to the large Coulomb energy associated with a non-uniform distribution of electron density. A 2DES with a ground plane is, in some way, intermediate between those two cases because over distances larger than the separation between 2DES and metallic plane the Coulomb interaction only has dipole character.

The authors argue that in this case, phase separation still occurs, but that the surface energy of minority phase droplets of large enough radius is negative. This property leads to the existence of various intermediate phases. Starting from a Wigner crystal at lowest densities, with increasing n_s the system is

predicted to exhibit both striped and bubble phases, with varying fractions of Fermi liquid and Wigner crystal, eventually turning into pure Fermi liquid phase. All the intermediate phases are expected to be conducting: This is quite clear if the Wigner crystal is the minority phase, where conduction occurs in the liquid phase. It also seems comprehensible that in a phase with large stripes of WC separated by small stripes of FL, conduction can still occur along the direction of those stripes. The case of small FL droplets embedded in a WC is more intricate. However, Ref. [51] argues that, unlike a pure Wigner crystal, such a phase is not pinned by small disorder and can bypass obstacles. In principle, this should allow electrical conductance through sliding of the entire crystal. An interesting observation is that due to a difference in spin entropy between liquid and crystal phase, in a certain temperature range an increase in temperature stabilises the crystal phase relative to the liquid one, which means that the high resistance WC fraction increases on cost of the low resistance FL. This could lead to an increase in resistance with increasing temperature, i.e. a metallic temperature dependence. This effect will be discussed in more detail in Sect. 6.2.1. Refs. [51, 52] discuss

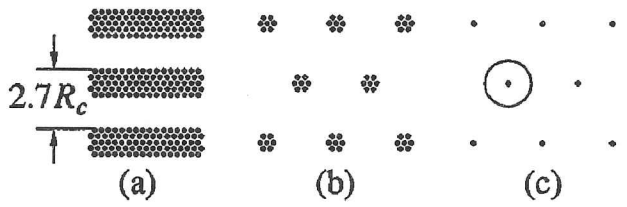

Figure 2.6: Charge density wave patterns: (a) Stripe pattern (R_c is the cyclotron radius). (b) Bubble patterns. (c) Wigner crystal (one cyclotron orbit is shown). [From Ref. [53]]

in particular the MOSFET, where charge neutrality is enforced by a metallic gate, as an example for which their predictions could be relevant, under the reservation that any real device will have a finite amount of disorder. Despite this, their reasoning should be qualitatively correct for the case of a gated AlGaAs heterojunction as well.

Many of their conclusions were later generalised to the case of any Coulomb interacting system, without the condition of a nearby ground plane [54]. In

particular, the requirement for existence of intermediate phases between liquid and crystal was confirmed. In a recent work these results were confirmed further, also including screening effects [55]. However, it was pointed out that the phase separation may only occur in an extremely narrow range around a critical density and at very low temperatures, making an experimental observation highly unlikely.

Nevertheless, there have been some experimental observations, which were interpreted as evidence of a state of crystal/liquid phase coexistence: A linear rather than exponential insulating temperature dependence in ultra high mobility two-dimensional hole gases (2DHG) in the strongly interacting regime up to $r_s = 80$ [56], and an oscillatory behaviour of the magnetoresistance in the insulating phases in the vicinity of the $\nu = 1/3$ filling factor in high mobility 2DHG [57]. While these are doubtless rather interesting experiments, I do not believe they are convincing evidence of a solid/liquid phase coexistence.

Stripe and bubble phases have also been suggested in a quite different context [53]: They were proposed as ground state configuration in 2DES at weak magnetic fields with $N \gg 1$ lower Landau levels completely filled and the upper level partially filled (for a brief discussion of Landau levels (LL) and the quantum Hall effect see Sect. 4.1.2). Hartree-Fock approximations were used to predict these charge density wave states under the condition that electron-electron interactions do not destroy the Landau quantisation, which was shown to be the case for $r_s \lesssim 1$. At high occupation of the highest LL, a charged density wave formed of stripes occurs, which turns into a bubble phase as the occupation is lowered. Further reduction reduces the number of electrons in each bubble until only one electron per "bubble" is left (see Fig. 2.6). This state is indistinguishable from a Wigner crystal. The driving force behind the aggregation of particles in domains is the reduction in exchange energy while the charge density variations (which are not energetically favourable) are not too large (of order 20%).

It should be noted that in form of the fractional quantum Hall effect (FQHE) a strongly correlated electronic phase in two dimensions in presence of strong perpendicular magnetic fields was discovered and has been studied extensively both experimentally and theoretically [44, 58, 59]. While a short description of the integer quantum Hall effect [60, 61] is given in Sect. 4.1.3, a discussion

of the FQHE is beyond the scope of this thesis because experiments presented here were not carried out in the FQHE regime.

2.5 Strongly Interacting Disordered 2DES

Let us now discuss the two-dimensional electron system in the regime of strong interaction but in presence of a finite amount of disorder. This is a theoretically extremely challenging problem, but it has the considerable advantage that it can actually describe real systems. At first sight, it may seem self-evident that disorder and electron-electron interactions always compete with each other, an increase in disorder reducing the effect of interactions between electrons. However, while very strong disorder certainly overrules interaction effects, it turns out that a moderate amount of disorder can actually *enhance* electron-electron interactions. Intuitively, this may be explained by a tendency of the disorder to quench the motion of the particles, thereby effectively increasing the strength of Coulomb energy between charge carriers compared to their kinetic energy.

2.5.1 Crystalline Phases

Chui and Tanatar studied the influence of impurities on the fluid-solid transition in 2DES at $B = 0$ and $T = 0$, using perturbation calculations and Monte Carlo simulations [20]. Their approach, with a disorder potential arising from surface roughness and positively charged impurities at a distance of 10 nm from the 2DES, was aimed at modelling a Si-MOSFET. Despite this, their findings may well be relevant to other systems such as GaAs/AlGaAs heterostructures. They found evidence of a crystal formation at an interaction parameter as low as $r_s \approx 7.5$, compared to $r_s \approx 37$ in the pure case. At higher density, electrons were found to relax around the impurities and "screen" them out. On the other hand, at r_s much larger than 7.5 the system became amorphous, leaving only a certain window of electron density where the crystalline phase exists. The physical interpretation for the stabilisation of a crystalline phase by impurities given by the authors is that the solid can adjust to the impurities more easily. The reduction of the impurity energies in the solid phase makes up for the

higher energy in the solid compared to the fluid. It should be noted that no attempt was made to optimise the disorder to minimise the transition density. This means that in optimal disorder the crystalline phase might persist to even higher electron densities.

Various authors have studied the effect of pinning centres on a Wigner crystal, generally starting with the assumption of a WC phase and investigating how pinning affects the stability and other properties of the phase [62–68].

A very simple model was used by Eguiluz *et al.* [62]: They assumed the existence of a WC and introduced pinning centres at certain lattice sites. This was implemented with a harmonic coupling between electrons, but also a harmonic "pinning" of some randomly chosen electrons to their lattice sites. Their numerical calculations revealed the existence of a sharp low frequency gap Δ_{pin} in the phonon spectrum of the WC and a reduction of the mean square deviation (MSD) of the electrons from their lattice sites. The quenching of the MSD was particularly strong under application of perpendicular magnetic field, but the magnitude of the pinning gap decreased with increasing B-field. Both the existence of the pinning gap and the MSD reduction persisted at finite temperatures. It was concluded that pinning centres considerably aid the stability of a 2D electron crystal at $T \lesssim 1$ K.

A different implementation of disorder was used by Chitra *et al.* [67, 68]. In their model, disorder was represented by a weak random potential with correlation length $r_{\text{f}} \ll \xi$ (ξ the localisation length of the electrons, which is in turn assumed $\ll a_0$, the lattice constant). In heterojunctions, such a disorder potential is expected to be present due to interface roughness. Long range disorder arising from distant dopants is not taken into account in this model. Variational calculations confirmed the existence of a pinning gap in zero [68] and finite [67] magnetic field. Related to the pinning gap (but not identical), a pinning frequency ω_{p} was calculated with an enhanced AC conductivity of the WC expected at resonance, which should be experimentally observable.

The pinning effect of remote charged donors was studied by Chui [64] with variational and numerical methods with good agreement between the two calculations. An explicit expression for the pinning gap was given:

$$m^* \Delta_{\text{pin}}^2 = \frac{0.09 n_\delta a_0^2 e^2}{\epsilon \epsilon_0 \delta_{\text{sp}}^3}, \tag{2.6}$$

with n_δ the doping concentration and δ_{sp} the spacer width. A common attribute of all these pinning studies is the assumption of an essentially classical crystal where individual electrons are so strongly localised that they can be treated as single particles. This is reasonable in the case of ultra low densities, or very high perpendicular fields, where $\xi \ll a_0$.

A completely different approach was chosen by Fukuyama and Lee [69]. They started from the assumption of a sinusoidal charge density wave (CDW) and examined the effect of random impurity centres, focusing on the phase of the CDW. They predicted a vanishing *DC* conductivity, but finite *AC* conductivity with a peak at the pinning mode ω_p. This is in agreement with Refs. [67, 68] (which were actually published more than twenty years later). However, details disagree and in particular, a qualitatively different B-dependence of ω_p was found in Ref. [68].

The temperature driven melting of a two-dimensional crystal is complicated enough in absence of disorder. A large amount of work has been put into studying the details of this transition (see e.g. Refs. [70]), but a detailed discussion of this problem is beyond the scope of this thesis. For the melting temperature, numerically $T_{Melt} \propto 1/r_s$ was calculated for the classical Wigner crystal [71], while for the quantum regime $T_{Melt} \propto 1/r_s^2$ was proposed [51]. Disorder is expected to have a strong impact on the melting temperature, in particular, the pinning gap in the phonon spectrum discussed above, might increase T_{Melt}. I am unaware of any quantitative studies of T_{Melt} in disordered classical or quantum crystals.

Experimentally, a 2D Wigner crystal has been observed on the surface of liquid helium [72]. For semiconductor based 2DES such conclusive evidence is still lacking, but some indications of a crystalline phase have been observed: Through transport experiments in high perpendicular magnetic fields in ultra clean electron- [13, 14] and hole-systems [15] or electron bilayer systems [16]. In a different approach, microwave absorption was used to detect the pinning mode of a Wigner crystal in low disorder and high fields [18, 73]. It is an interesting fact that two crucial discoveries in semiconductor physics were first incorrectly interpreted as evidence of a CDW state, namely the single electron transistor [74] and the fractional quantum Hall effect [58].

2.5.2 Other Phases

As seen previously, there are two regimes of strongly localised 2DES which are, at least theoretically, relatively well understood, namely when either the energy scale of the disorder is much larger than the interaction energy (Fermi glass), or vice versa (Wigner crystal). Qualitatively, one can imagine what happens, when starting from a Wigner crystal, disorder with increasing strength is introduced or the interaction strength is reduced. At first, the electrons will be moved slightly out of their positions and defects such as vacancies and interstitials will be introduced. Such a solid, where electrons are localised due to electron-electron interactions, but the long range order of a crystal is missing, is called a Wigner glass. Moving further in disorder/interaction space, the 2DES will eventually end up as the Fermi glass described in Sect. 2.3.3. However, despite extensive work, no full theory for the intermediate regime is available. Below, a summary of theoretical and some experimental work in this field is given.

Cha and Fertig [75] studied what happens to a two-dimensional crystal when slowly varying disorder with increasing strength is introduced. They proposed a phase transition at a critical disorder strength. Below the critical point, the number of dislocations which are energetically favourable vanishes in a finite size crystal. Above the critical point, the number of dislocations diverges in an infinite size system. This was interpreted as a zero temperature phase transition between crystal and non-crystal.

Thakur and Neilson [76] proposed a "frozen electron solid" in presence of strong electron-electron interaction. In this state, electrons are localised due to exchange-correlation effects, i.e. not simply by disorder. The state is not crystalline but shows a liquid-like short-range order. What distinguishes it from a liquid is that the electrons cannot move. They are frozen in a metastable state, i.e. it is not the ground state of the system. In view of the metallic temperature dependence described in Chapt. 6, it is of particular interest whether the scaling theory described in Sect. 2.3.2, which prohibits a truly metallic ground state in 2D, holds up in the presence of electron-electron interactions. There has been a great deal of theoretical and experimental work in this direction, especially after the observation of an apparent metal-insulator transition in two dimensions [19]. An overview of the relevant work will be given in Chapt. 6

with a special focus on its relevance to the experimental results of this thesis.

2.6 Transport Properties

At low densities in strongly disordered 2DES where electrons are localised in potential traps, transport occurs by hopping between those traps. This means that electrons jump between two trap sites under absorption or emission of a phonon of the energy corresponding to the energy difference between the two sites. At relatively high temperatures, these jumps are between sites close to each other, as there are many phonons available and there is a high probability that a phonon matches the energy difference between the sites. This process is called nearest neighbour hopping (NNH) and leads to a simple activated transport behaviour

$$\rho(T) = \rho_0 \exp(E_0/k_B T), \tag{2.7}$$

with k_B the Boltzmann constant. When the temperature gets lower, the probability increases of the electron hopping to a site further away in space but closer in energy. Therefore, the average hopping distance depends on temperature and becomes longer at lower T. This effect is called variable range hopping (VRH). These two transport mechanisms are schematically shown in Fig. 2.7.

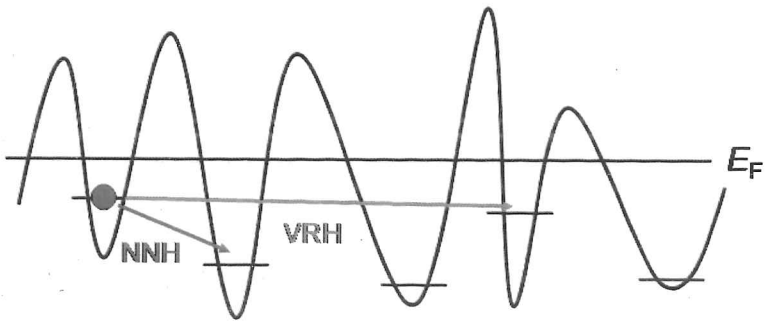

Figure 2.7: Schematic representation of nearest neighbour hopping (red arrow) and variable range hopping (green arrow) trapped in conduction band minima.

Mott first derived a law of transport in the VRH regime under the assumption of a constant density of states at the Fermi level [3]. He predicted a temperature dependence of resistivity of the form

$$\rho(T) = \rho_0 \exp([E_0/k_B T]^{1/3}) \tag{2.8}$$

in two dimensions. The existence of a Coulomb gap in the density of states at the Fermi level (discussed in Sect. 2.3.3), modifies this law, leading to the Coulomb gap or Efros-Shklovskii (ES) hopping law [8]

$$\rho(T) = \rho_0 \exp([E_0/k_B T]^{1/2}). \tag{2.9}$$

Experimentally, both Mott and ES hopping have been observed, mainly in strongly disordered 2DES. For instance, in silicon MOSFETs Mott hopping was reported in Ref. [6] and ES hopping in Ref. [9]. In GaAs/AlGaAs heterojunctions Mott hopping was observed in a δ-doped wafer with a spacer of only two monolayers [7]. In comparable wafers, both Mott and ES hopping were reported [10]: While the non-interacting Mott law was found to be valid at high electron densities, a crossover to the ES law was observed when the electron density was reduced.

Not much is known about transport in a Wigner crystal. It is generally assumed that the WC is pinned by the disorder, which prevents a sliding of the crystal as a whole, unless a large voltage is applied that can depin it. Shklovskii argued that the pinning of the crystal leads to a finite density of charged localised states near the Fermi level, which leads to an ES hopping behaviour of transport [77].

Transport could also occur by hopping of localised point defects such as vacancies or interstitials, which would also lead to an insulating behaviour with nearest neighbour or variable range hopping. However, as discussed in detail in Sect. 6.2.1, in a crystal with strong zero point fluctuations of the electrons, a delocalisation of defects could be possible, with a qualitative change in transport where the resistance might decrease with decreasing temperature.

Mott first derived a law of transport in the VRH regime under the assumption of a constant density of states at the Fermi level [3]. He predicted a temperature dependence of resistivity of the form

$$\rho(T) = \rho_0 \exp([E_0/k_B T]^{1/3}) \tag{2.8}$$

in two dimensions. The existence of a Coulomb gap in the density of states at the Fermi level (discussed in Sect. 2.3.3), modifies this law, leading to the Coulomb gap or Efros-Shklovskii (ES) hopping law [8]

$$\rho(T) = \rho_0 \exp([E_0/k_B T]^{1/2}). \tag{2.9}$$

Experimentally, both Mott and ES hopping have been observed, mainly in strongly disordered 2DES. For instance, in silicon MOSFETs Mott hopping was reported in Ref. [6] and ES hopping in Ref. [9]. In GaAs/AlGaAs heterojunctions Mott hopping was observed in a δ-doped wafer with a spacer of only two monolayers [7]. In comparable wafers, both Mott and ES hopping were reported [10]: While the non-interacting Mott law was found to be valid at high electron densities, a crossover to the ES law was observed when the electron density was reduced.

Not much is known about transport in a Wigner crystal. It is generally assumed that the WC is pinned by the disorder, which prevents a sliding of the crystal as a whole, unless a large voltage is applied that can depin it. Shklovskii argued that the pinning of the crystal leads to a finite density of charged localised states near the Fermi level, which leads to an ES hopping behaviour of transport [77].

Transport could also occur by hopping of localised point defects such as vacancies or interstitials, which would also lead to an insulating behaviour with nearest neighbour or variable range hopping. However, as discussed in detail in Sect. 6.2.1, in a crystal with strong zero point fluctuations of the electrons, a delocalisation of defects could be possible, with a qualitative change in transport where the resistance might decrease with decreasing temperature.

Chapter 3

Devices and Experimental Techniques

3.1 Devices

This section discusses the design and fabrication of the devices that were used in the experiments. The design is simple, but required some optimisation process, chiefly to find the optimal device dimensions. The fabrication itself was done in straight-forward standard optical and e-beam lithography, and does not present any original research work. Therefore, the discussion is kept very short.

A list of devices with relevant geometry and wafer parameters is given in App. A.

3.1.1 Wafers

The GaAs/AlGaAs heterostructures were grown in our group by molecular beam epitaxy (MBE) on top of a substrate made of a GaAs single crystal. Most of the wafers used were δ-doped, i.e. the dopants were restricted to a few atomic monolayers, as opposed to bulk-doping, where the dopants are distributed in a thicker layer of AlGaAs, typically a few tens of nanometres.

The advantage of δ-doping is that it gives a well defined distance between 2DES and dopants, making the spacer width δ_{sp} a good quantity to classify the disorder strength in the 2DES. In all electron systems, Si-dopants were used. The layer sequence for a typical δ-doped wafer (A2678) is shown in Fig. 3.1. The wafers used had spacer widths $\delta_{sp} = 20 - 80$ and mobilities $\mu = 0.6 - 1.8 \times 10^6\,\mathrm{cm}^{-2}/\mathrm{Vs}$ in the dark as cooled down.

Surface/Topgate
50 nm GaAs
200 nm $Al_{0.33}Ga_{0.77}As$
0.556 nm GaAs
Si $2.5 \cdot 10^{12}\,\mathrm{cm}^{-2}$ **(Doping layer)**
0.556 nm GaAs
40 nm $Al_{0.33}Ga_{0.77}As$ **(Spacer)**
1000 nm GaAs
50 nm $Al_{0.33}Ga_{0.77}As$
50 nm GaAs
Substrate: (100) GaAs semi-insulating

Figure 3.1: Layer sequence for a typical δ-doped wafer (A2678), with spacer δ_{sp}=40 nm and total depth of the 2DES d_g=290 nm from the surface.

3.1.2 Geometry

All devices consist of a small Hall bar mesa with one or several gate fingers crossing the mesa between the voltage probes, as schematically shown in Fig. 3.2 a). Since the measurements were done in the low density regime under the gate, transport would always be dominated by the active area under the gate, of dimensions $W \times L$. The dimensions were optimised to allow for the advantage of mesoscopic dimensions while still being large enough to form a two dimensional system. The width was $W = 8\,\mu$m in all cases, while the length varied between $0.5 - 4\,\mu$m.

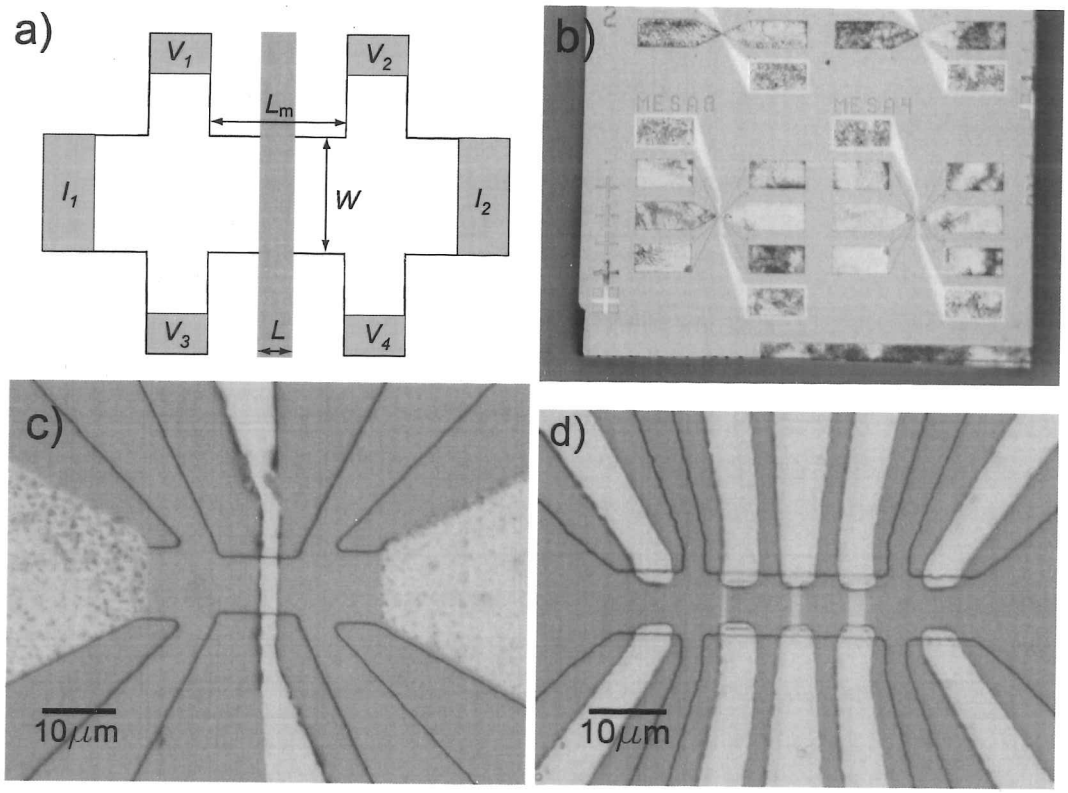

Figure 3.2: a) Schematic of a Hall bar geometry with a gate finger across (golden area). Grey areas labeled $I_{1,2}$ and V_{1-4} indicate Ohmic contacts used for current and voltage probes, respectively. b) Optical microscope image of a chip wit two full devices. c) Optical microscope image of the mesa with an optically defined gate of width $W \approx 3\,\mu$m. d) Optical microscope image of the mesa with three e-beam defined gates of width $W \approx 0.5$, 1 and $2\,\mu$m. The large gates leading away from the mesa were done optically with the leftmost and rightmost pair being unused but kept grounded during experiments.

3.1.3 Fabrication

The first step of the processing is to cleave the wafer into pieces. Usually, a large enough piece is cleaved to make several devices on it. This increases the probability to get at least one working sample. After the cleaving, one has a 2DEG which extends laterally over the whole chip. For our devices a Hall bar mesa was fabricated by optical lithography: A photoresist (Shipley 1813) layer is deposited on the sample surface, baked and then brought into contact with a chrome on glass mask on a mask aligner. The mask contains the pattern of the mesa structure which is projected to the sample by exposure to UV light. The development in MF319 removes the photoresist where it has been exposed. A wet etching procedure with a 1:8:160 H_2SO_4:H_2O_2:H_2O solution etches the sample where it is not protected by the photoresist anymore. Usually, the etching time was adjusted to etch a few tens of nanometres below the GaAs/AlGaAs interface where the 2DES is formed. This defines the Hall bar structure on the 2DES.

In the next step, Ohmic contacts to the 2DEG are produced. Again, photoresist is spun on the sample and exposed with a different mask. This time the mask has to be aligned carefully to match the mesa pattern on the chip. After developing, a AuGeNi alloy is evaporated to the sample surface. After that, the resist is removed. The evaporated AuGeNi peels off where the resist was not already developed. This process in known as "lift-off". Now the sample is annealed at a temperature of 430° C. In this step the AuGeNi melts and diffuses into the GaAs to the 2DEG. Since germanium is a n-dopant in GaAs, the annealing produces a conducting spike which contacts the 2DEG. The composition of AuGeNi is optimised for several factors: Melting temperature of the alloy, good diffusion into the GaAs and a surface that allows bonding. Due to the large depth of the 2DES under the surface, a large amount of AuGeNi (>100 nm) was used and the annealing time was extended from the standard 80 s to 120 s.

In a procedure very similar to the Ohmics processing, a frontgate is produced. Instead of AuGeNi a layer of NiCr ($\sim$ 20 nm) and subsequently a layer of gold ($\sim$ 100 nm) are evaporated, with the NiCr layer being necessary because gold does not stick well on GaAs. Because the topgate is not alloyed, a Schottky barrier is formed between topgate and sample. The minimum width

of gates that could be fabricated with optical lithography was $\sim 1-2\,\mu$m, the fundamental limit being the wavelength of light. For even smaller dimensions, electron-beam (e-beam) lithography was used with the advantage of a much smaller wavelength. The procedure is analogous to the optical gate fabrication, except that a different resist (PMMA) and developer (5:15:1 MIBK:IPA:MEK) were used and the exposure is done by direct "writing" with an electron beam. The exposure was done by David Anderson. The e-beam resist is thinner than the photoresist, which makes the lift-off process after evaporation difficult if the metal layer is too thick. Therefore, the evaporation thickness was limited to ~ 25 nm NiCr and 15 nm Au in this process. Because e-beam lithography is suitable only for small features, the bonding pads of the gates and their leads to the actual gates were done optically in another step, which required very careful alignment of the mask with the e-beam gates. The optical gates were designed to overlap slightly with the mesa, since the e-beam gates are very likely to break at the steep step at the mesa edge because of their thinness.

Finally, the sample is cleaved into small chips with only one or two devices, which are fixed on a chip carrier and connected to its contacts by gold wires. The chip carrier can be plugged into the sample holder of the cryostat probe or directly soldered to its wiring loom.

3.2 Cryogenic Systems

In order to observe quantum effects the devices have to be cooled to low temperatures. A temperature of 4.2 K can be reached by simply dipping the device into a liquid helium dewar.

For lower temperatures, more sophisticated systems have to be used. $T \gtrsim 1$ K can be reached quite easily in ^{4}He-cryostats. By pumping on the surface of liquid helium in a small reservoir (called 1 K pot), the boiling point of the helium and, hence, the temperature in the reservoir can be lowered.

The limiting factor of pumped ^{4}He is that it becomes superfluid at $T = 2.2$ K, which makes pumping very difficult. This problem can be overcome by using ^{3}He, which becomes superfluid only at about 1 mK. Unfortunately, ^{3}He is very expensive and to reduce the amount of ^{3}He needed, a sorbtion pump rather than a rotary pump is used in most cases. This is essentially a cylinder

containing a material with a huge surface area, called the sorb. When the sorb is cooled to 4.2 K, it absorbs most of the ^{3}He gas, reducing the pressure and, hence, boiling point of the ^{3}He liquid. A temperature of $T \approx 300$ mK can be achieved in such systems. When all the ^{3}He has evaporated, the sorb is heated up, releasing the captured helium, which is then liquefied with help of a 1 K pot and collected in the ^{3}He reservoir. These systems are relatively easy to run and have the advantage that the ^{3}He can be kept in a completely closed circuit, which greatly reduces the risk of losing any of the ^{3}He. The disadvantage is, that they do not run continuously and the ^{3}He has to be re-liquefied every $24 - 48$ h. The majority of experiments presented in this thesis were carried out in a ^{3}He-system.

For continuous running and much lower temperatures, a dilution- refrigerator or "fridge" can be used. It uses a ^{3}He/^{4}He mixture, which separates into a ^{4}He-rich and a ^{3}He-rich phase at low temperatures. The cooling arises from evaporation of ^{3}He across the phase boundary from the ^{3}He-rich to the ^{4}He-rich phase in the mixing chamber. The ^{3}He is then pumped out with a big pump (rotary or diffusion) through the still (basically a reservoir with large surface to enhance the evaporation rate) and continuously returned into the mixing chamber after being liquefied by a 1 K pot and pre-cooled by heat exchangers with the still. In our experiments, two different dilution-refrigerators were used. In Fridge I, the device was directly immersed in the mixing chamber, while in Fridge III the device was separated from the mixing chamber through a cold finger which lead the device into the centre of the magnet. Here, the cooling of the device occurs through the wiring which is thermally anchored to the mixing chamber. Only two measurement presented in this thesis were done in Fridge I (Figs. 4.8 and 7.10), while all the other measurements at $T < 300$ mK were done in Fridge III.

3.3 Low-Temperature Measurements

3.3.1 Four-Probe Lock-in Measurements

All measurements were done with lock-in amplifiers. Their working principle is that the measurements are done at a low frequency AC excitation and that

the signal is only measured at this frequency, while noise signals at frequencies other than the reference signal are rejected. This greatly reduces the noise problem, but various other measures to reduce noise have to be taken, nevertheless. The biggest source of noise are all electrical and electronic instruments (including the measurement instruments themselves!) of which there are inevitably countless in any physics laboratory. It is practically impossible to eliminate the noise sources, so the best thing one can do is try to protect the measurement system from it as much as possible. Most effectively, this is done by keeping the cryostat in a screened room (i.e. a Faraday cage). Any noise prone instruments are kept outside this room and electrical connections are led through low-pass filters which keep any high frequency noise out.

The following pages describe the measurement set-ups and noise reduction measures for the two systems that were mainly used for the experiments.

^{3}He-Cryostat (Heliox)

The Heliox is not in a screened room, but with the use of all-analogue lock-ins and an optimum set-up with coaxial cables both in- and outside the cryostat, an excellent noise level could be achieved.

It was found that a constant current set-up yielded best results, which is schematically shown in Fig. 3.3. In such a set-up, a resistor R_L is connected after AC voltage source V_ex. If R_L is much larger than the resistance of the device (e.g. $R_\mathrm{L} = 1\,\mathrm{G}\Omega$), the current will be constant $I_\mathrm{ex} = V_\mathrm{ex}/R_\mathrm{L}$. The device resistance $R = \Delta V/I_\mathrm{ex}$ can then be deduced from the measured voltage drop ΔV between appropriate voltage probes for Hall- or longitudinal resistance. For calibration of the current, the voltage drop was first measured across a known resistor R_C in series with the device and of a resistance similar to the one to be measured. The excitation voltage was then adjusted to give the correct current and subsequently, the voltage probes were removed from the resistor and connected to the device.

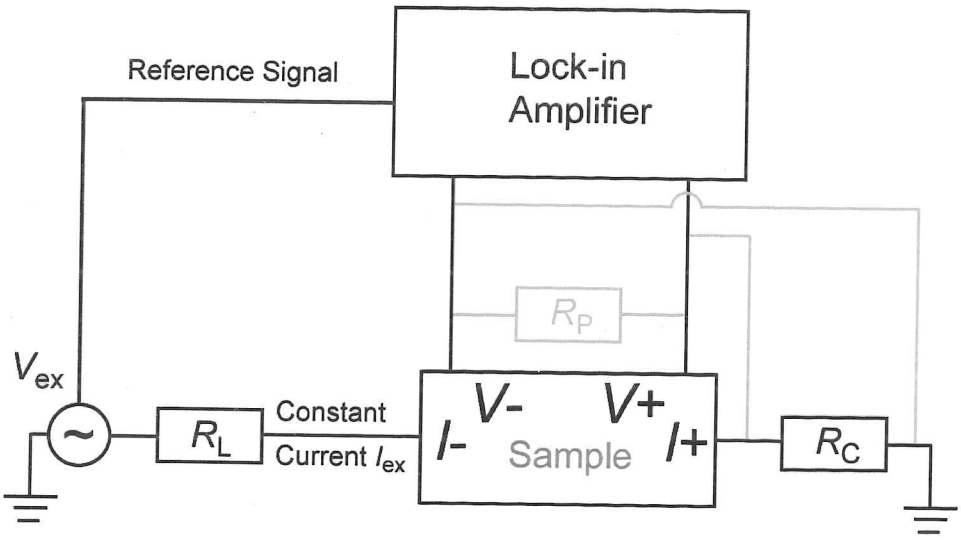

Figure 3.3: Four-probe set-up with constant current. The part in light grey was only used for the high-resistance set-up described in the text.

For high resistance measurements ($\lesssim 1.5\,\mathrm{M\Omega}$) a small current $I_{ex} = 100\,\mathrm{pA}$ was used to avoid Joule heating (see also Sect. 3.3.2) and to make sure that measurements were in the linear response regime. For measurements in the quantum Hall regime, a larger current had to be used to achieve a reasonably measurable voltage, so the current was increased to $I_{ex} = 5\,\mathrm{nA}$ in this case. For all measurements a frequency of $\Omega_{ex} = 7.3\,\mathrm{Hz}$ was used.

Fridge III

Fridge III is in a screened room. Here, an analogue oscillator and digital lock-ins were used, but all instruments were kept outside the screened room and connections were appropriately filtered when entering.

In this system, a constant voltage set-up was found to give the best measurements, as shown schematically in Fig. 3.4. The excitation voltage V'_{ex} is taken across a voltage divider (e.g. $\times 10^{-4}$) to provide a small constant AC-voltage V_{ex}. If the resistance R of the sample is large compared to the rest of the system, R can be deduced as $R = V_{ex}/I_{out}$, where I_{out} is the current flow through the device measured by the lock-in. However, in large magnetic fields, the contact resistance of the Ohmics can become large. Therefore, the voltage

drop ΔV across the device was measured simultaneously with a second lock-in, and the sample resistance was calculated as $R = \Delta V / I_{\text{out}}$, which eliminates the contact resistance. The signals were amplified with a voltage pre-amplifier ($\times 10^3$) and current pre-amplifier ($\times 10^7$), respectively. A capacitor $C_{\text{B}} \approx 40\,\mu\text{F}$ was connected between the fridge and the current pre-amplifier to block a *DC*-offset caused by the current preamp. A small excitation voltage $V_{\text{ex}} = 5\,\mu\text{V}$ at a frequency $\Omega_{\text{ex}} = 84\,\text{Hz}$ was used.

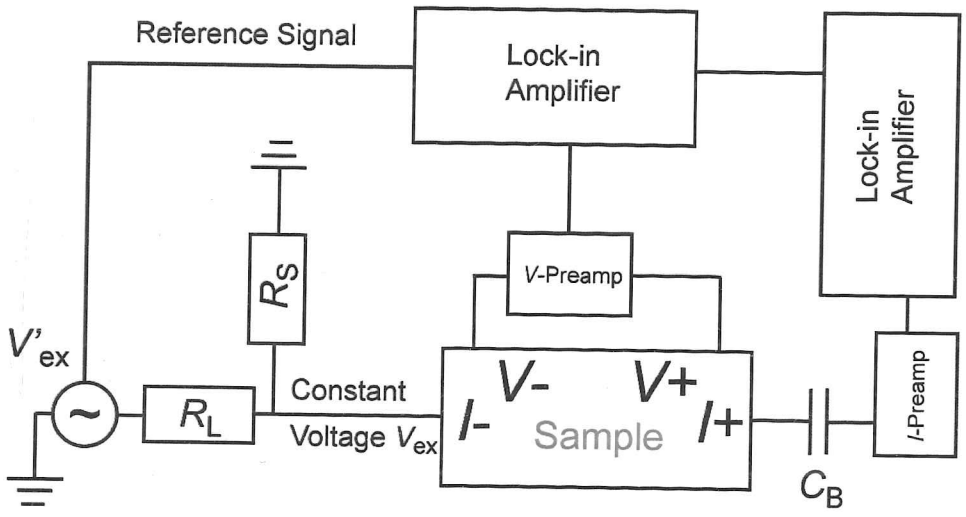

Figure 3.4: Four-probe set-up with constant voltage.

High Resistance Set-Up

It is problematic to measure very large resistances with the described set-ups, since the measured resistance should always be much smaller than the input impedance of the lock-in amplifiers. If this is not the case, a part of the excitation current will pass trough the lock-in, leading to an error in the measurement. Therefore, the measured device resistance was generally limited to $R \lesssim 2\,\text{M}\Omega$. In some cases it was required to measure to higher resistances. In these measurements, a slightly different four-probe constant current set-up was used. A resistor $R_{\text{P}} \approx 2\,\text{M}\Omega$ with known resistance is connected in parallel to the device as shown in Fig. 3.3. This means that the lock-in never measures

a resistance larger than R_P even when the device resistance is much larger. The device resistance can then be determined through the relation $R = \frac{\Delta V/I_{ex} \times R_P}{R_P - \Delta V/I_{ex}}$. In principle, this allows to measure arbitrarily high resistances, however, the larger R gets, the worse the sensitivity gets. Even at relatively small R, the precision is not as good as in a direct measurement. Therefore, this set-up was only used when a very accurate determination of the absolute value of R was not required and the measured range was limited to $R \lesssim 10\,\mathrm{M}\Omega$.

Resistance vs. Resistivity

A short note to clarify the use of the terms resistance and resistivity throughout this thesis. The measurements reveal the absolute resistance R of the device. Under the assumption that the resistance is dominated by the area under the gate, the resistivity ρ can then be deduced as $\rho = R \times W/L$ with W and L the device dimensions as defined in Fig. 3.2 a).

3.3.2 Temperature Control

Cryostat Temperature

In both systems, the cryostat temperatures were measured with RuO_2 thermometers. It is well known that the resistance of these thermometers can drift with time, bringing an error to the calibration. However, this error is expected to be relatively small ($< 20\,\mathrm{mK}$ according to Ref. [78]) and not relevant in our measurements where the change in temperature is much more important than the absolute temperature to a very high precision. Also, RuO_2 thermometers work quite well even at high magnetic fields, which is not the case for more precise thermometers, such as Ge resistors. This advantage and, more importantly, the lack of available Ge thermometers in the used cryostats, are the reasons why RuO_2 thermometers were used.

In Fridge III, the RuO_2 thermometer is at the mixing chamber which is at a significant distance from the device. Therefore, the sample temperature can be higher than the measured temperature in the mixing chamber. In order to ensure that there was no big discrepancy, a commercial Coulomb blockade thermometer (CBT) was placed in the sample space along with the device

in one cooldown. The measured temperature was $T_{\mathrm{CBT}} \cong 70\,\mathrm{mK}$ at a base temperature in the mixing chamber of $T_{\mathrm{MC}} \cong 60\,\mathrm{mK}$, determined with the RuO_2 thermometer. This is a reasonably small deviation and the difference relative to the absolute temperature is expected to become smaller with higher temperatures.

The temperature control was then performed with standard PID feedback controllers. The heat was either applied directly to the mixing chamber (Fridge III), the ^{3}He-pot (Heliox at $T \gtrsim 2\,\mathrm{K}$) or to the sorb (Heliox at $T \lesssim 1.8\,\mathrm{K}$). Heating the sorb reduces its pumping power, which increases the pressure in the ^{3}He-pot and, hence, its temperature.

Electron Temperature

If a 2DES is heated appreciably, e.g. by Joule heating through a current flow, the thermal equilibrium between the electron system and the phonon system can collapse. An effective electron temperature T_{e} is then observed, which could be considerably higher than the lattice temperature T_{L}.

In view of the saturation of the temperature dependence of resistance discussed in Chapt. 6 (e.g. Fig. 6.11), it is important to make sure that the electron temperature actually agrees with the measured cryostat temperature. Otherwise, the saturation of resistance could be explained simply by electron heating and a saturation of T_{e}. It seems unlikely that such a saturation should be so similar for two different cryostats with different cooling power and completely different measurement set-ups. Nevertheless, a discussion of electron heating in our experiments is appropriate.

Electron heating can arise from the intentionally induced current that is unavoidable whilst performing measurements, as well as from unintentional currents induced by noise. As described in Sect. 3.3.1, great care was taken to reduce the noise to a minimum, and very small excitation currents or voltages were used. A quick check for significant heating effects can be done by changing $I_{\mathrm{ex}}/V_{\mathrm{ex}}$ within a certain range around the planned value and check if the measured resistance remains the same. This also ensures that measurements are conducted in the linear response regime.

The electron temperature can be directly measured through the damping of Shubnikov-de Haas-oscillations. The temperature dependence of SdH-

oscillations can be expressed as [21]

$$\frac{\Delta\rho}{\rho_0} = \frac{8\pi^2 k_B T_e/\hbar\omega_c}{\sinh(2\pi^2 k_B T_e/\hbar\omega_c)} \exp(-\frac{\pi}{\omega_c \tau}), \tag{3.1}$$

with τ the quantum scattering time, $\Delta\rho$ the amplitude of the oscillations and ρ_0 the average between minimum and maximum value of one oscillation. Note that τ is the only unknown in the formula. If the electron temperature does not agree with the measured cryostat temperature, a good fit of Eq. (3.1) is not possible. In particular, a saturation of T_e at lowest cryostat temperatures can be easily detected with this method.

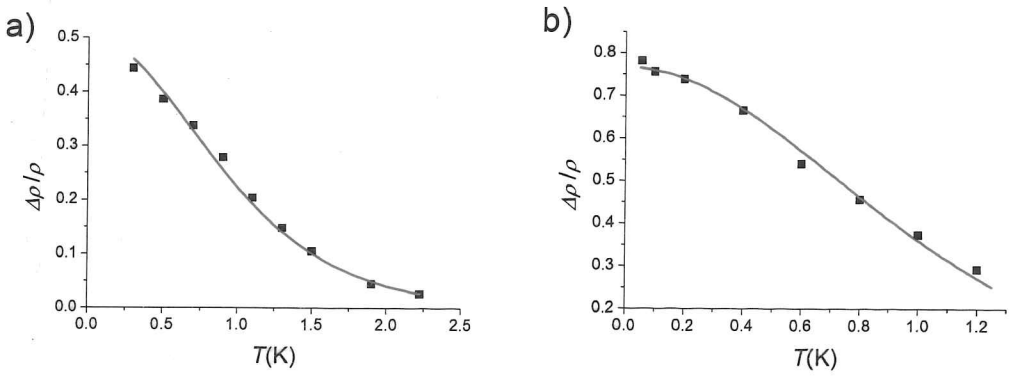

Figure 3.5: Damping of SdH-oscillations with fits of Eq. (3.1). In both Heliox a) and Fridge III b) a good fit is possible and no sign of a saturation of the electron temperature is observed.

Fig. 3.5 shows the damping of SdH-oscillations with fits of Eq. (3.1) for both the Heliox and Fridge III. In neither case any sign of a saturation of electron temperature can be detected. The measurements were done in mesoscopic devices with the gate voltage kept at $V_g = 0$. One could argue that a possible Joule heating would be stronger in a smaller area and at higher resistance. However, while SdH oscillations cannot be measured in the localised regime for obvious reasons, there are other indicators that suggest that a saturation of electron temperature does not occur even in the localised regime and that the

observed saturation of the temperature dependence of resistivity is not caused by such an effect.

Most importantly, as discussed in Chapt. 6, in many cases the resistance did not just saturate, but showed a turnaround with a decreasing resistance towards lowest temperatures (e.g. Fig. 6.2). After a sharp downturn, the temperature dependence seems to flatten at lowest T in Fig. 6.2 as well. However, this impression arises from the $1/T$-scale and a look at Fig. 6.1 c) confirms that the resistance continues to drop down to base temperature. This non-monotonic behaviour of the temperature practically rules out a saturation of electron temperature.

An additional argument against Joule heating is, that it depends strongly on the resistance. Hence, if the saturation of resistance was caused by Joule heating, the saturation temperature should strongly depend on the resistance. For a constant current set-up, the Joule heating power is $P_J = RI_{ex}^2$, i.e. it is proportional to the resistance. By contrast, in a constant voltage set-up, $P_J = V_{ex}^2/R$, i.e. an inverse proportional relation to resistance and opposite trend. Despite this, as discussed in Chapt. 6, no significant change in saturation temperature was often observed over ranges in resistance of an order of magnitude or more.

3.3.3 Slow Cooldown Technique

It was found that for a good stability of the device, a slow cooldown technique was vital. In all successful experiments, devices were cooled down from room temperature to 4 K in at least 12 h, but preferably $\gtrsim$ 24 h.

This could be related to the DX-centres discussed in Sect. 2.2.2. In a very fast cooldown, some of the remaining electrons in the dopant layer may not have time to form DX-centres. They would then form shallow d^0-states, which are much less stable than DX-centres at low temperatures and can move around, leading to switching events and instability of the device.

Additionally, the remaining electrons in the dopant layer could rearrange themselves in order minimise the electrostatic energy. This would lead to a correlated charge distribution compared to the completely random distribution of the donor atoms. Correlations should be strongest at lowest temperatures, but

below the freeze-out temperature of the DX-centres no rearrangement of the charges is possible. Therefore, the crucial temperature for formation of charge correlations is just above the freeze-out temperature, i.e. $T \gtrsim T_{\mathrm{DX}} \approx 130\,\mathrm{K}$. Since the movement of charges gets slower and slower as T_{DX} is approached, it is particularly important to cool down slowly in this temperature range, to give the electrons enough time for redistribution.

Theoretically, charge correlations have been predicted to suppress long-range fluctuations of the 2DES disorder potential [25] and experimentally, an enhanced mobility ascribed to charge correlations in the doping layer has been reported [79]. In our case, a suppression of the long-range disorder could further reduce the effect of charge inhomogeneities at low electron densities, enhancing the effect of the mesoscopic device dimensions.

In order for correlation effects to be strong, a significant number of electrons must remain in the dopant layer. We define the filling factor $\eta = 1 - n_{\mathrm{d}^+}/n_\delta$, with $0 \leq \eta \leq 1$, where n_{d^+} and n_δ are the density of d^+ states and total density of dopants, respectively. A simple electrostatic calculation gives a way to estimate η experimentally. The total charge density of the dopant layer $n_{\mathrm{Q}} = n_{\mathrm{d}^+} - n_{\mathrm{DX}}$, can be calculated as $n_{\mathrm{Q}} = \frac{\epsilon_0 \epsilon}{e d_\delta}(V_{\mathrm{S}} - V_0)$, with d_δ the distance between sample surface and doping layer, V_{S} the Schottky barrier between topgate and GaAs and V_0 the depletion voltage which can be measured experimentally [80]. The filling factor can then be immediately determined as $\eta = 1/2(1 - n_{\mathrm{Q}}/n_\delta)$. Indeed, with $\eta = 0.2 - 0.4$, the filling factors in all of our devices were in a regime were correlation effects are expected to be strong.

The effect of possible charge correlations in the doping layer is further discussed in connection to biased cooldowns in Sect. 9.2.1.

Chapter 4

Measurement of Electron Density in Mesoscopic 2DES

As will become clear in later chapters, an important part of the experiments presented in this thesis is the measurement of the electron density as a function of the applied gate bias. First of all, the electron density provides a measure of the effective Coulomb interactions in the 2DES through the interaction parameter $r_s \propto 1/\sqrt{n_s}$ (see Sect. 2.1.3). But apart from that, many of the interesting transport phenomena could not have been understood without knowing the electron density.

This chapter describes a new technique for measuring the electron density in mesoscopic 2DES based on the reflection of edge states at the gate in the quantum Hall regime. The physics behind it has been known for a long time and it has been used for density estimates in quantum point contacts. However, to my knowledge it had never been systematically applied for electron density measurements in 2DESs.

4.1 Theoretical Background

4.1.1 Tuning the Electron Density

In order to control the electron density in the 2DEG a frontgate is used. By application of a voltage to this gate the electron sheet density n_s can be tuned. A relation between gate voltage and sheet density can be derived in a simple model [80]: The electron gas forms a slab of finite thickness and electron sheet density n_s. A voltage V_g applied between the front gate and the electron gas induces a surface charge σ_g on the front gate surface. The surface charge can be related to the gate voltage through the capacitance C_0. With d_g being the separation between the front gate and the front side boundary of the electron slab, one obtains $\sigma_g = \epsilon\epsilon_0 V_g/d_g$. Charge conservation demands

$$(n_s - n_Q) = \frac{\sigma_g}{e} = \frac{\epsilon\epsilon_0}{d_g e} V_g = C_0 V_g, \tag{4.1}$$

where n_Q is a contribution from the charged donor atoms. This model neglects any quantum corrections that might change the effective electrical depth of the 2DEG [80], but it generally agrees very well with the observed result in structures like the ones used in our experiments.

4.1.2 2DEG in a Magnetic Field

The following derivation follows Ref. [61], where a more detailed description can be found. It is assumed that only one subband (SB) is occupied. A strong magnetic field $B_\perp$ perpendicular to the 2DEG causes the electrons to move in cyclotron orbits. This leads to a formation of discrete energy levels, called Landau levels (LL), with energies

$$E_n = E_0 + (n + \frac{1}{2})\hbar\omega_c \pm g\mu_B B, \qquad n = 0, 1, 2, ..., \tag{4.2}$$

with E_0 the energy of the lowest SB, the Landé factor g, the cyclotron frequency $\omega_c = \frac{eB_\perp}{m^*}$ and the Bohr magneton μ_B. It can be shown that the degeneracy per unit area of the LLs is

$$N_L = \frac{N_0}{L_x L_y} = \frac{eB_\perp}{h}. \tag{4.3}$$

Note that this value is proportional to the magnetic field, but independent of any material constants like effective mass etc. The density of states (DOS) changes from a constant in 2D to a series of delta peaks. In high magnetic fields, the degeneracy of the LLs is high and therefore all the electrons are in the lowest LL. As the B-field decreases, the energetic position of the LL and therefore the Fermi energy decreases. At some point the degeneracy of the LL gets lower than the constant number of electrons and the next higher LL starts being populated and the Fermi energy makes a jump upward. This results in a zigzag behaviour of the Fermi energy as shown in Fig. 4.1 a) and gives rise to dramatic changes of the DOS $D(E_F)$. This has remarkable consequence for many physical properties, particularly for the electric resistance as will be explained in the following two sections.

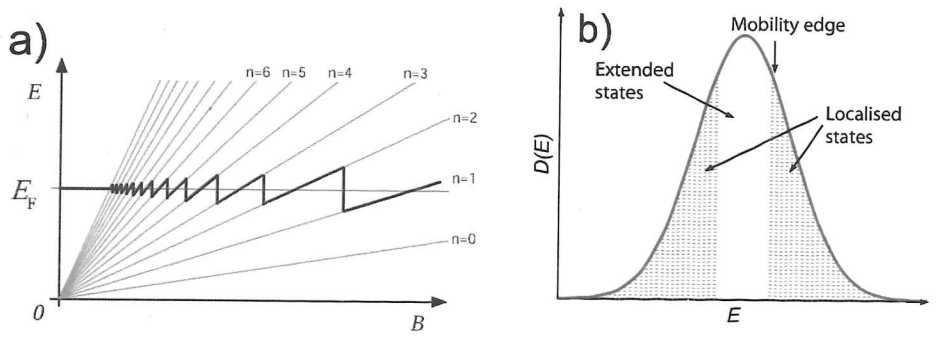

Figure 4.1: a) Fermi energy as a function of magnetic field. [From Ref. [81]] b) Broadened Landau level with localised and extended states.

4.1.3 Quantum Hall Effect

This is a very brief overview of the phenomenon called integer quantum Hall effect (IQHE). Consider a rectangular 2DEG of dimensions L_x and L_y in the x- and y-direction. A current I_x is applied in the x-direction. We define the longitudinal and transverse 2D resistivity coefficients, ρ_{xx} and ρ_{xy}, by $E_x = \rho_{xx} J_x$ and $E_y = \rho_{xy} J_x$, where J_x is a 2D current density defined as $J_x = I_x / L_y$. The classical predictions for these two coefficients are [82]:

$$\rho_{xx} = \frac{m^*}{n_s e^2 \tau}, \qquad \rho_{xy} = -\frac{B_\perp}{n_s e}, \tag{4.4}$$

with τ the scattering time, i.e. ρ_{xx} is independent of $B_\perp$ and ρ_{xy} increases linearly with $B_\perp$. However, the experimental results at low temperatures are very different, as can be seen in Fig. A. The Hall resistivity ρ_{xy} increases in steps at high fields. The values of ρ_{xy} along the horizontal portions are very constant at values related to the fundamental constants h and e by

$$\rho_{xy} = -\frac{h}{ie^2} = -\frac{25812.8\Omega}{i}, \tag{4.5}$$

where i is an integer. The value of these plateaux can be explained with the LLs described in Sect. 4.1.2 [61]. We define the filling factor ν as the number of occupied LLs below the Fermi energy. N_L from Eq. (4.3) being the degeneracy per area of the LLs and n_s the electron sheet density, the filling factor can be expressed as

$$\nu = \frac{n_s}{N_L} = \frac{n_s}{\frac{e}{h}B_\perp}. \tag{4.6}$$

At certain magnetic fields, ν has an integer value and the classical Hall resistivity Eq. (4.4) is

$$\rho_{xy} = \frac{B_\perp}{en_s} = \frac{B_\perp}{e\nu\frac{e}{h}B_\perp} = \frac{1}{\nu}\cdot\frac{h}{e^2}. \tag{4.7}$$

This explains the value of the plateaux but not why there are plateaux at all.

So far the Landau levels have been considered as delta peaks. However, taking electron scattering at impurities into account, the LLs are broadened. In a magnetic field electrons can be localised at impurities if the cyclotron radius is smaller than the distance between the impurities. Numerical simulations show that the extended states are in the center of the LLs and the localised states at the edge [61]. This is schematically shown in Fig. 4.1 b). The edge between localised and extended states is sometimes referred to as the mobility edge. An analysis of the width of the ρ_{xx} peaks in the limit of zero temperature shows that only a few percent of the states of a LL are not localised [83]. Only the extended states can carry a current, whereas all the states contribute to the degeneracy of the LLs. Hence, neither the Hall resistance ρ_{xy} nor the magnetoresistance change, as long as the Fermi energy is in the range of localised states.

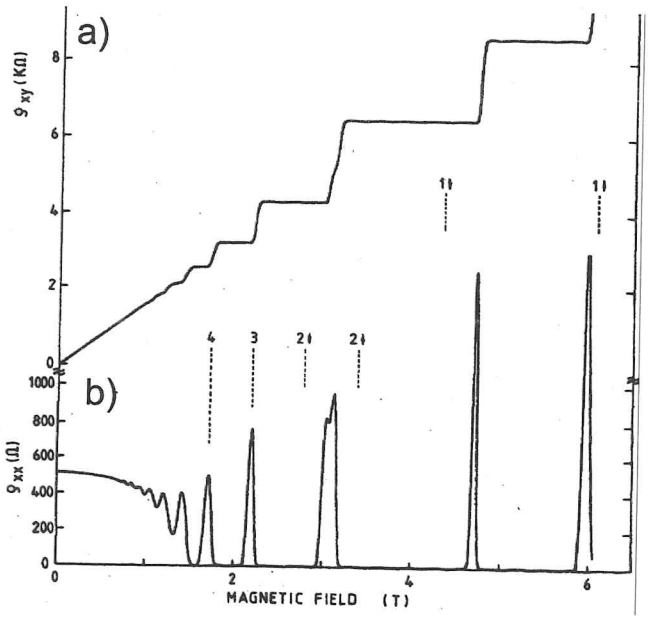

Figure 4.2: a) Quantum Hall plateaux and b) Shubnikov-de Haas oscillations. [From Ref. [61]]

4.1.4 Shubnikov-de Haas Oscillations

Not only the Hall resistance but also the longitudinal resistance of a 2DEG behaves very differently from classical predictions: Classically the longitudinal resistance ρ_{xx} is independent of a magnetic field (Eq. (4.4)), but in Fig. A it shows an oscillatory behaviour, the so called Shubnikov-de Haas (SdH) oscillations. The resistance disappears in the range where the Hall resistance is constant, but shows distinct peaks when the Hall resistance jumps from one plateau to another. This can again be explained with LLs. As long as the Fermi energy lies between two LLs, the lower of these two LLs is completely filled and there are no free states where electrons could be scattered into. A scattering process would have to excite the electron to the next higher LL, which is obviously not possible for elastic scattering. Therefore any scattering is suppressed and the resistance disappears. Only when the Fermi energy coincides with the energy of a LL, there are empty states in the LL and scattering is possible. Without any broadening of the LL the peaks in ρ_{xx} would be delta shaped, but if the LLs are broadened the SdH peaks get broadened

as well. When the spin splitting of the LL, which is $\Delta E = g\mu_B B$ according to Eq. (4.2), is larger than the broadened width of the extended states of the LLs (see Fig. 4.1 b)), the spin splitting can be observed in the magnetoresistance as two separate peaks. But in low magnetic fields, where the spin splitting of the LL is small, the two LLs merge and behave like one LL with double degeneracy. Here, only even filling factors are observed. In this regime the SdH oscillations are periodic in $1/B_\perp$.

4.1.5 Edge State Picture

In this section a brief introduction to the edge state picture of the quantum Hall effect is given. In Eq. (4.2) the energy eigenvalues for electrons in a 2DEG applied to a perpendicular magnetic field were given. This result is true in the case where the potential in the plane of the 2DEG vanishes. However, near the edges of the sample there will be a non-vanishing potential. This causes an increase of the energy eigenvalues and an upward bend of the Landau levels. In a naive one-electron picture, this would lead to a simple crossing of the LLs with the Fermi level, as shown in Fig. 4.3 b) and a stepwise decrease of the electron density near the sample edge (Fig. 4.3 c)). Since for transport, the states near the Fermi level are important, this results in narrow current carrying states along the edges, called edge states, shown in Fig. 4.3 a). Chklovskii *et al.* showed that in reality, the behaviour is not that simple [84]. They argued that the electron density at an etched or gated edge of a 2DEG in a GaAs/AlGaAs heterostructure is dominated by the electrostatics of the distribution of charges in donor layer, surface and gate. The smooth decrease of electron density at the edges can only be weakly modified by a magnetic field as shown in Fig. 4.3 f). The self-consistent electrostatic potential increases stepwise, and strips of compressible and incompressible liquid are formed (Fig. 4.3 e)). This leads to a quite different picture of the edge states, with extended compressible strips that can carry a current, separated by narrow incompressible strips (Fig. 4.3 d)). For the density measurements discussed in this chapter, the exact structure of the edge states should not matter as long as they remain one-dimensional and, hence, the Landauer-Büttiker formalism can be applied (discussed in the following paragraphs). However, it may be relevant to the experimental results

presented in Chapt. 8.

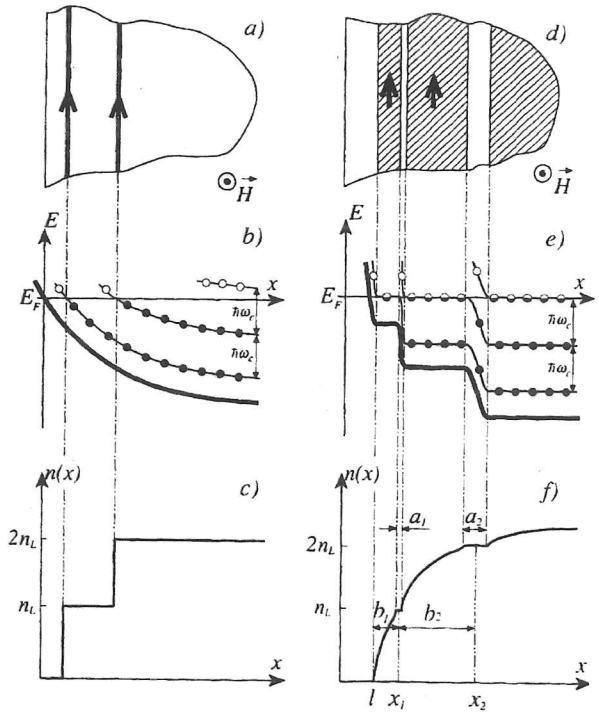

Figure 4.3: a)-c) One-electron picture of edge states with a smooth effective potential and stepped electron distribution. d)-f) Self-consistent electrostatic picture with a stepped effective potential and smooth electron distribution. [From Ref. [84]]

The current fed into the edge states belonging to one Landau quantum number is given by

$$I = ev_{\mathrm{nk}}D(E)\Delta\mu = \frac{e}{h}\Delta\mu, \tag{4.8}$$

where the longitudinal velocity v_{nk} and the density of states $D(E)$ cancel out because of the one-dimensional nature of the edge states. In analogy to the classical skipping orbits at the two edges, the longitudinal velocities are in opposite directions at the two edges.

Transport in one-dimensional channels was treated by Büttiker [85]. He treated not only many channels but also the influence of many contacts. The basis of his formula is the conservation of current. He treats different contacts on an equal footing, i.e. current contacts and potential probes are equivalent.

The law of current conservation is applied to all the contacts simultaneously. The resulting formula for the current in the contact i is

$$I_{\mathrm{i}} = \frac{e}{h}\left((N - r_{\mathrm{ii}})\mu_{\mathrm{i}} - \sum_{\mathrm{j}} t_{\mathrm{ij}}\mu_{\mathrm{j}}\right), \tag{4.9}$$

with N the number of channels, r_{ii} the sum of the reflection coefficients from contact i to contact i, μ_i the electrochemical potential in contact i, and t_{ij} the sum of the transmission coefficients from contact j to contact i. For the quantum Hall effect one assumes that the transmission coefficients at the edges for the different edge channels are unity while the backscattering (i.e. scattering from one edge to the other) is suppressed. Under these assumptions, the Hall

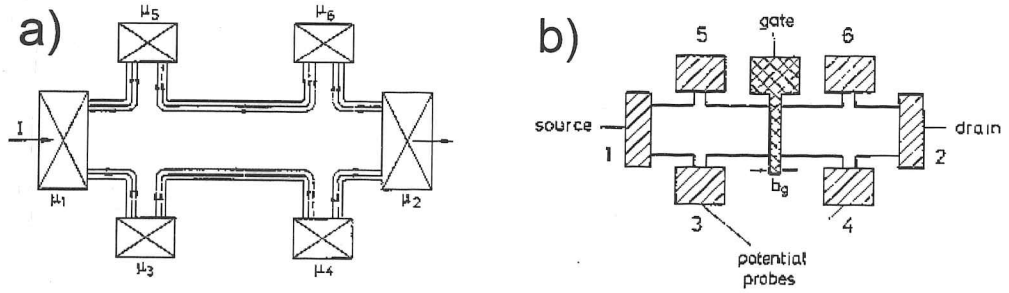

Figure 4.4: a) Hall bar geometry in a magnetic field applied perpendicular to the plane with two Landau levels occupied. b) Hall bar geometry with a gate finger across it. [From Ref. [86]]

resistance for the geometry shown in Fig. 4.4 a) with two edge states can be calculated:

$$R_{35} = \frac{\mu_3 - \mu_5}{eI} = \frac{h}{2e^2}, \tag{4.10}$$

since $I = \frac{2e}{h}(\mu_1 - \mu_5)$ and $I_3 = 0 = \frac{2e}{h}(\mu_3 - \mu_1)$.
The edge state model of the quantum Hall effect provides a powerful tool for the calculation of the resistance in a Hall bar with a gate finger across as shown in Fig. 4.4 b). As shown in Sect. 4.1.1 the carrier density under the gate can be changed. Therefore, in a magnetic field, the filling factor in this region can be changed as well and the Hall bar sample will contain regions of different filling

factors. As described above, the filling factor can be related to the number of occupied edge states. Hence, the number of edge states under the gate can be decreased. The edge states which exist in the adjacent undisturbed regions of the 2DEG, but are missing in the gate region, are reflected at the gate.

Within the edge state picture it is possible to calculate the resistance between the potential contacts 3 and 4 in Fig. 4.4 b):

$$R_{34} = \frac{\mu_3 - \mu_4}{eI} = \frac{h}{e^2}\left(\frac{1}{\nu} - \frac{1}{\nu_0}\right), \tag{4.11}$$

where ν and ν_0 are the filling factors under the gate and in the rest of the Hall bar, respectively. In measurements on gated Hall bars in a magnetic field corresponding to an integer filling factor in the ungated region, plateaux in the resistance as a function of gate voltage have been observed at the predicted values [87, 88].

4.2 Measuring the Electron Density

4.2.1 Conventional Method

As seen in the previous section, the electron sheet density of a 2DEG can be calculated from the $1/B_\perp$-periodic SdH-oscillations of the resistivity namely

$$n_{\mathrm{SdH}} = \frac{2e}{h\Delta(\frac{1}{B_\perp})}, \tag{4.12}$$

where $\Delta(\frac{1}{B_\perp})$ is the period of the SdH-oscillations in the regime where the spin splitting is not resolved. At low magnetic fields the Hall resistivity increases linearly with $B_\perp$:

$$\rho_{\mathrm{xy}}(B_\perp) = \frac{B_\perp}{n_{\mathrm{H}}e}. \tag{4.13}$$

This relation gives us an easy way of determining the electron sheet density from the slope of ρ_{xy} in this linear range. The densities n_{H} and n_{SdH} are equal if only one energy subband of the 2DEG is occupied.

4.2.2 New Technique for Small Active Areas

These conventional density measurements cannot be used if the active region of the device is very small. An alternative technique based on the edge state picture described in Sect. 4.1.5 comes to our aid if the sample is similar to the one shown in Fig. 4.4 b). To measure the density under the gate, a perpendicular magnetic field is set to a value that corresponds to an integer filling factor in the ungated region. These values of magnetic field can be determined by standard Shubnikov-de Haas measurements when the gate voltage is set to zero. Then the resistance is measured as a function of the gate voltage V_{g}, which leads to plateaux at the values of $R_{34} = \frac{h}{e^2}(1/\nu - 1/\nu_0)$ (Eq. (4.11)), provided the contacts are close to ideal with no reflection and perfect transmission. V_g at the center of these plateaux then corresponds to an electron density $n_{\mathrm{s}} = eB_{\perp}\nu/h$, while the width of the plateau represents the maximum uncertainty.

4.3 Experimental Results

In Sect. 4.1, the theoretical background for an alternative electron density measurement technique based on the reflection of edge states was given. In the following, this technique is used to measure the gate voltage dependence of the electron density of a for mesoscopic 2DES as described in Sect. 3.1. In these devices conventional Shubnikov-de Haas measurements cannot be done.

4.3.1 Measurements at $V_{\mathrm{g}} = 0$

In a first step the electron density in the ungated region of the device is measured in a conventional Shubnikov-de Haas measurement. This is done by measuring the transverse and longitudinal resistance as a function of the magnetic field at zero gate voltage. Such a measurement is shown in Fig. 4.5. A beating of the SdH oscillation can be seen, which is explained by a difference in electron density underneath and away from the gate, i.e. a slight depletion under the gate even at V_{g}=0.

Now the positions of several minima in the Shubnikov-de Haas oscillations

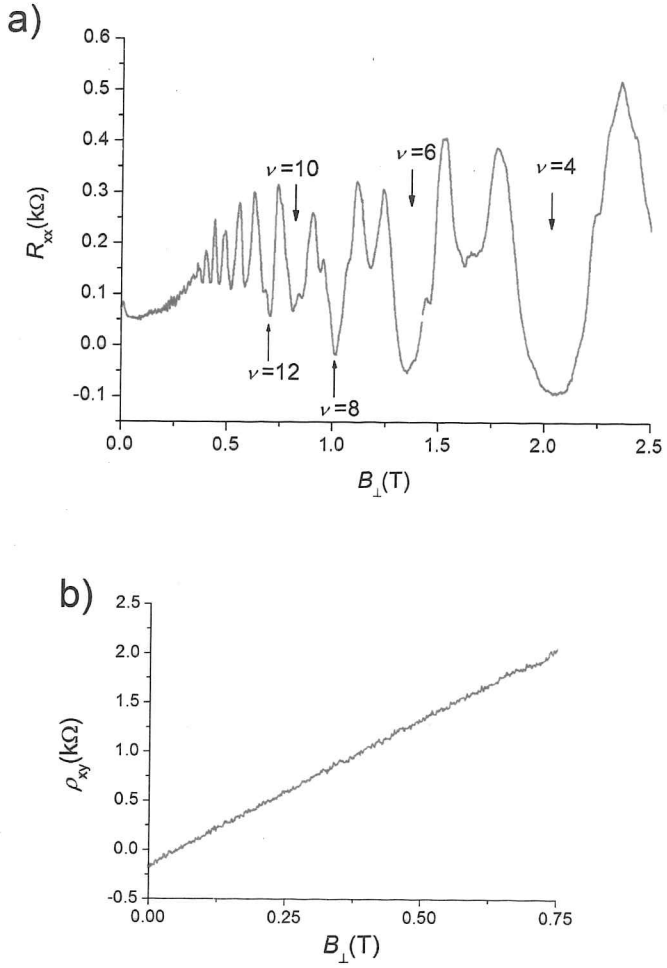

Figure 4.5: (Device A78f T=300 mK) a) Longitudinal magnetoresistance with Shubnikov-de Haas oscillations. A beating of the oscillation can be seen, which comes from superposition of SdH under the gate, where the density is reduced even at $V_g = 0$. The minima at low ν show a negative resistance. This is a measurement artefact, which can explained by one of the contacts used for the voltage probes getting a very high resistance in higher magnetic fields. This does not affect the SdH periodicity and does, hence, not have any impact on the density measurement. b) Hall resistance of the same sample.

are determined. The positions of the minima in R_{xx} determines the magnetic fields of the integer filling factors used in the second stage of the experiment which will be described below. An alternative method to determine integer filling factors is by doing a Fourier analysis of the SdH oscillations, which extracts their periodicity in $1/B_\perp$. Via the relation $n_{\mathrm{SdH}} = \frac{2e}{h\Delta(\frac{1}{B_\perp})}$ (Eq. (4.12)), the electron density can be measured, leading to the B-fields for integer filling factors according to Eq. (4.6). In fact, this method proved more reliable and was used in most cases. In some devices, particularly when the electron density was low or the zero gate voltage depletion was strong, SdH oscillations where difficult to measure. In these cases, the electron density could be determined by a measurement of the Hall resistance at low fields, where it is not quantised, using Eq. (4.4). This method is less precise, since it depends on the actual measured value of the resistance, while the analysis of SdH oscillations is unaffected by a possible error of the resistance. Also, if several subbands are occupied, the Hall analysis gives the sum of the densities of all subbands, whereas the SdH analysis measures each subband separately. However, the second point is unimportant in our case, since only one subband is expected to be occupied in all devices used in this thesis. For the device shown in Fig. 4.5 (A78f), a direct comparison between Hall- and SdH-density can be made. It reveals $n_{\mathrm{SdH}} = 2.075 \times 10^{11}\,\mathrm{cm}^{-2}$ and $n_{\mathrm{Hall}} = 2.11 \times 10^{11}\,\mathrm{cm}^{-2}$ giving difference of $< 2\%$.

4.3.2 Gate Voltage Dependence of the Electron Density

After determining the B-field values at filling factors ν_0=4, 6, 8, 10 and 12 in the ungated region of the Hall bar, the measurements for the density under the gate could be done. The longitudinal resistance of the Hall bar was measured as a function of gate voltage at each of the magnetic fields corresponding to the filling factor in the ungated region given above. A summary of the results is shown in Fig. 4.6 a), while b) and c) show details of measurements at two magnetic fields.

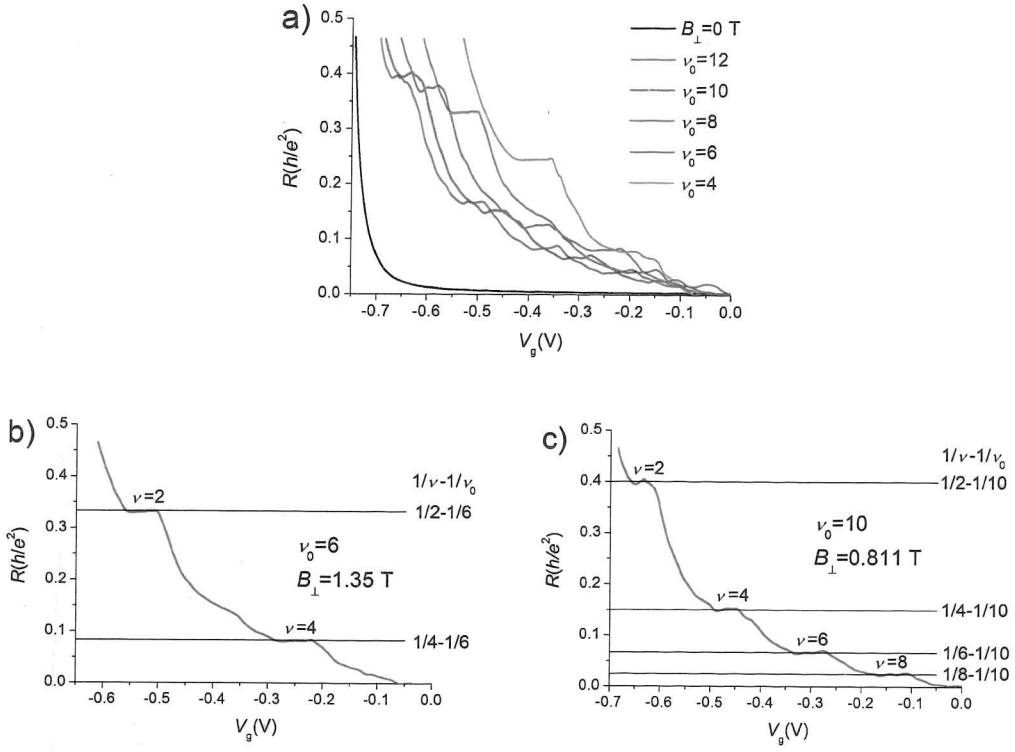

Figure 4.6: (Device A78f; T=300 mK) a) Longitudinal resistance as a function of gate voltage at magnetic fields corresponding to integer filling factors $\nu_0 = 4, 6, 8, 10$ and 12 in the ungated region of the device. b), c) Examples of the plateaux used to find the position of integer filling factors under the gate.

Clear plateaux are visible at even filling factors and the agreement of the resistance at the plateaux with the expected values $R = 1/\nu_0 - 1/\nu$ with $\nu_0 < \nu$ when plotted in units of h/e^2 is excellent. In some cases, a series resistance had to be subtracted to get a good agreement, but in the sample shown, this was not necessary. The V_g at the centre of these plateaux corresponds to an electron density of $n_s = eB_\perp \nu/h$.

The results of these measurements are shown in Fig. 4.7. The electron density shows an almost perfectly linear dependence on the gate voltage. The slope is approximately $C = 23.5 \times 10^{10}\,\mathrm{cm}^{-2}\mathrm{V}^{-1}$ which agrees very well with

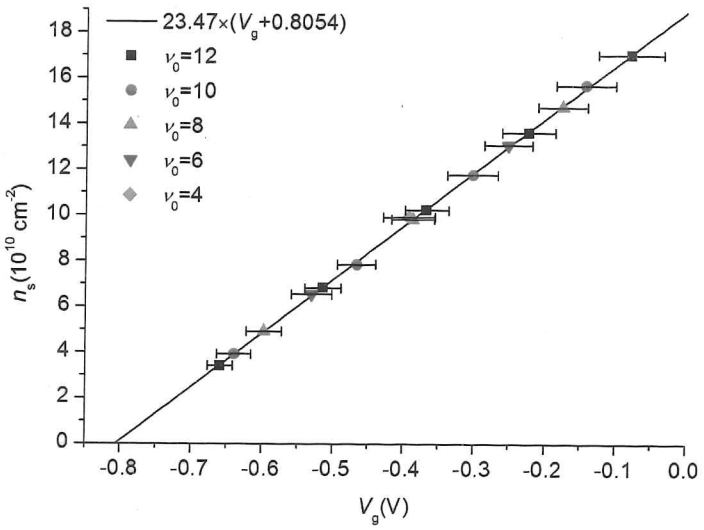

Figure 4.7: Gate voltage dependence of the electron density determined from the plateaux positions in the measurement shown in Fig. 4.6.

the theoretically predicted value of $C_0 = \frac{\epsilon\epsilon_0}{d_{ge}} = 24.6 \times 10^{10}\,\mathrm{cm}^{-2}\mathrm{V}^{-1}$ (Eq. (4.1)).

Including Odd Filling Factors

In the data shown so far only even filling factors were taken into account in the analysis. This is because at the temperature of 300 mK, where a large part of the data presented in this thesis was taken, odd filling factors could not usually be resolved.

However, at very low temperatures in a dilution refrigerator, odd filling factors can be resolved, providing additional density points and improving the precision and reliability of the density measurement method described in this chapter. Fig. 4.8 shows a density measurement done in a dilution refrigerator, where the sample was immersed in the mixing chamber at a temperature of 30 mK. The sample was illuminated with a LED prior to the measurement. Therefore, the electron density was particularly high, leading to an increase of the magnetic field where a given filling factor occurred. This lead to an excellent resolution of odd filling factors under the gate, even when the filling

factor in the ungated part of the device was high. Odd filling factors were also observed in other devices without illumination at dilution refrigerator temperatures, although not usually as clearly. Fig. 4.8 a) shows a gate sweep at $B_\perp$=1.28 T, which corresponds to $\nu_0 = 10$. No correction due to series resistance was done in this measurement. Very clear plateaux are visible at ν=2, 4, and 6, but also at the odd filling factors ν=3 and 5.

In Fig. 4.8 b) the measured densities are plotted as a function of gate voltage. The obtained slope is $C = 64.75 \times 10^{10}\,\mathrm{cm}^{-2}\mathrm{V}^{-1}$ comparing to the theoretical value of $C_0 = 79 \times 10^{10}\,\mathrm{cm}^{-2}\mathrm{V}^{-1}$. The deviation of $\sim 20\%$ is still reasonably low. In the plot, a distinction between data points achieved from even and odd filling factors is made. As expected, no systematic difference between even and odd filling factors can be observed.

Experimental Error

As discussed above, the error bars given in Figs. 4.7 and 4.8 b) are determined by the width of the plateaux in the density measurement. Using these error bars an estimate for the error in the final density function determined by the linear fit to the data points can be made. This is done simply by tilting the fit as far as possible away from the best fit without leaving the boundaries given by the error bars. This provides extreme values for the slope C and the depletion voltage V_0. Such an estimate is shown in Fig. 4.9 (red line). Together with the best fit, it provides a density $n_\mathrm{s} = 23.5^{+2.9}_{-2.2} \times (V_\mathrm{g} - 0.8054^{+0.031}_{-0.035}) \times 10^{10}\,\mathrm{cm}^{-2}$. However, a simple look at the quality of the linear fit suggests that these boundaries hugely overestimate the error. If the actual errors of the density points were as large as the error bars suggest, a scattering around the linear fit of the same order would be expected, at least if the error was random. A more realistic, if slightly vague, error estimate can be done by simply trying out, how far the best fit might be bent without deviating unreasonably far from the data points. This is shown in the blue lines in Fig. 4.9 and provides the reduced errors $n_\mathrm{s} = 23.5 \pm 0.53 \times (V_\mathrm{g} - 0.8054 \pm 0.0079) \times 10^{10}\,\mathrm{cm}^{-2}$.

A systematic error in the analysis, e.g. an asymmetry of the plateaux with respect to the precise position of the integer filling factor cannot be completely ruled out. Such an error would lie within the boundaries given in the first error estimate, but not necessarily in the second, smaller estimate. However, such

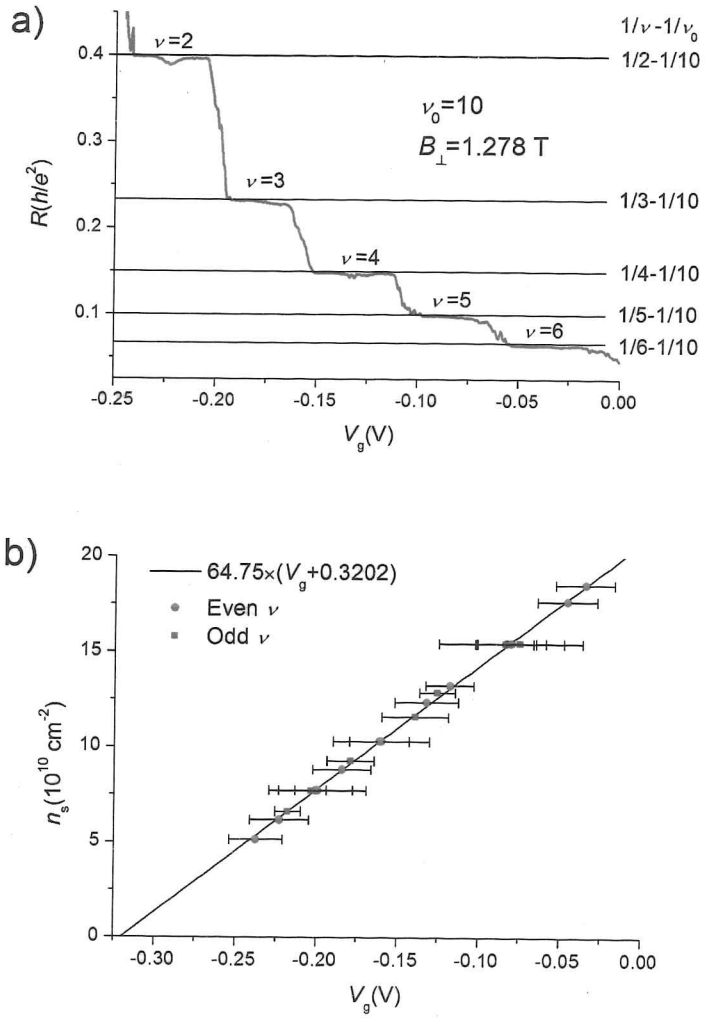

Figure 4.8: a) Longitudinal resistance as a function of gate voltage at magnetic fields corresponding to integer filling factor ν_0=10 ($B_\perp$ = 1.28T) in the ungated region of the device, at T = 30 mK. Plateaux at both even and odd filling factors can be clearly observed. b) Densities obtained from ν_0=14, 12, 10, 8, 6, and 4, distinguishing between even and odd filling factors ν under the gate. No systematic deviation between even and odd is observed. (Device A77b).

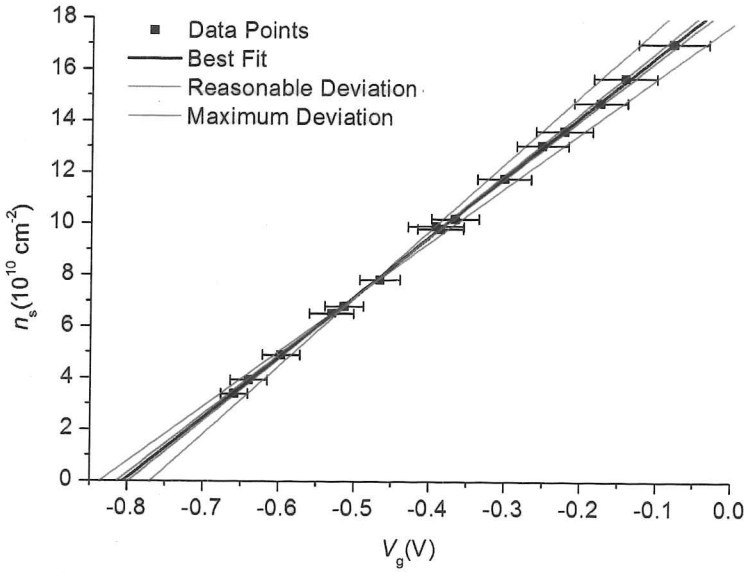

Figure 4.9: The same data as in Fig. 4.7, but apart from the best linear fit (black line), the maximum deviation from the best fit that still fits within the error bars (red lines), and a maximum deviation based on eye judgement (blue lines) are given.

a systematic error would be unlikely to be independent of magnetic field and electron density or even/odd filling factor. Hence, if the error was large, a deviation from linearity would be expected. As discussed above, this is not the case even when both even and odd filling factors are included.

Another error comes from the measured density n_{SdH} in the ungated part of the device. If $n'_{\mathrm{SdH}} = C \times n_{\mathrm{SdH}}$ then $n'_{\mathrm{s}} = C \times n_{\mathrm{s}}$, where n' and n are the measured and actual electron density, respectively. This error does not lead to a non-linearity of the measured density and is, hence, harder to detect. However, the error coming from the Fourier analysis of the SdH-oscillations is generally expected to be rather small. Also, since no offset in the depletion voltage V_0 is caused, extrapolation of the measured densities to the low density regime does not increase the relative error, making it less serious for our purpose.

Chapter 5

Magnetoresistance of Hopping Transport

This chapter discusses magnetoresistance (MR) measurements in the hopping regime of 2DES. It presents the first detailed study of this kind in mesoscopic high mobility 2DES.

In Sect. 5.2, the average hopping distance r_{hop} is analysed as a function of electron density. Surprisingly, it is found that $r_{\mathrm{hop}} \approx r_{\mathrm{ee}} = 1/\sqrt{n_{\mathrm{s}}}$, the average electron-electron separation. This is strong evidence that electron-electron interactions play an important role in transport. A quantitative analysis in terms of transport mediated by defects in an interaction induced electron solid is given.

Sect. 5.3 treats the hopping prefactor R_{B} as defined in Eqs. (5.1) and (5.3). It is found that this prefactor decreases exponentially with increasing n_{s} at low densities, but saturates at higher densities and forms plateaux at the universal values h/e^2 and $h/2e^2$. The universality occurs in resistance rather than resistivity and is independent of gate length and, within a window, spacer width. The result is interpreted as additional evidence of a strongly correlated electron phase, where hopping is assisted by electron-electron rather than electron-phonon interactions.

Sect. 5.4 presents other aspects of the MR, in particular the low and high field limits. The results are discussed in consideration of the findings in

Sects. 5.2 and 5.3 and some further support to the conclusions of these sections is given.

5.1 Theoretical Background

Hopping transport, where electrons tunnel between states near in space and energy, is determined by the wave function overlap and the availability of an energy transfer mechanism, which allows for electrons to absorb or emit the energy difference of the states between which it tunnels. While the second term has most impact on the T-dependence of transport (Chapt. 6), it is the first term that dominates the magnetoresistance.

A magnetic field $B_\perp$ perpendicular to the plane of the 2DES increases the confinement of the electrons by effectively producing a harmonic potential of the form $V(r) = \hbar^2 r^2/8m^* l_B^4$ with $l_B = \sqrt{\hbar/eB_\perp}$ the magnetic length. In a weak $B_\perp$ such that $l_B \gg \xi$, the hydrogenic wave function of a localised electron $\psi(r) \propto \exp(-r/\xi)$ (ξ the localisation length) changes to $\psi(r) \propto \exp(-r/\xi - r^3\xi/24l_B^4)$ which reduces the wave function overlap and, hence, the tunnelling probability. This leads to a magnetoresistance of the form [89, 90]

$$\rho(T, B_\perp) = \rho_B(T) \exp(\alpha B_\perp^2), \tag{5.1}$$

with

$$\alpha = Ce^2 r_{hop}^3 \xi/12\hbar^2. \tag{5.2}$$

Here, r_{hop} is the average distance between trap sites and the model dependent constant $C \approx 1 - 1.5$ depends on the number of bonds in the random resistor network, i.e. the number of available states an electron can hop to with non-negligible probability. For the MR prefactor one finds

$$\rho_B = \rho_0 \exp(E_t/k_B T)^p \exp(2r_{hop}/\xi), \tag{5.3}$$

with E_t the energy mismatch between electronic states and $p = 1$ for nearest neighbour hopping (NNH) and $p = 1/3$ or $p = 1/2$ for variable range hopping (VRH) without or with a Coulomb gap, respectively (see Sect. 2.6).

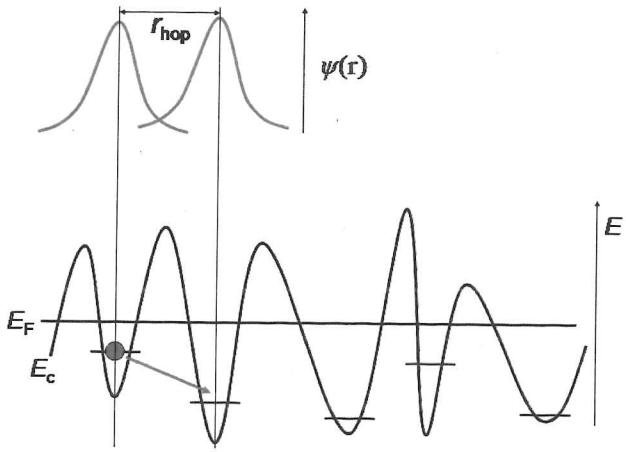

Figure 5.1: Schematic of hopping between localised electron states in a random disorder potential.

In a strong magnetic field such that $l_B \ll \xi$, the electron wave function becomes a Gaussian $\psi(r) \propto \exp(-r^2/4l_B^2)$. In this case, the magnetoresistance is [90]

$$\rho(T, B_\perp) = \rho'_B(T) \exp(\beta B_\perp), \tag{5.4}$$

with

$$\beta = C' e r_{hop}^2/\hbar. \tag{5.5}$$

5.2 Density Dependent Hopping Distance

5.2.1 Overview

Expression (5.1) has been confirmed experimentally for hopping transport in the impurity band in the inversion layer of sodium-doped Si-MOSFET [91] as well as in layers of Si donors in GaAs [17]. Here, it is shown that an exponential $B_\perp^2$-dependence also occurs in the strongly localised regime of mesoscopic modulation-doped GaAs/AlGaAs heterostructures, which are much less disordered.

Fig. 5.2 shows the MR in low perpendicular field for devices from four different modulation-doped heterojunctions including δ-doped wafers with δ_{sp}=20,

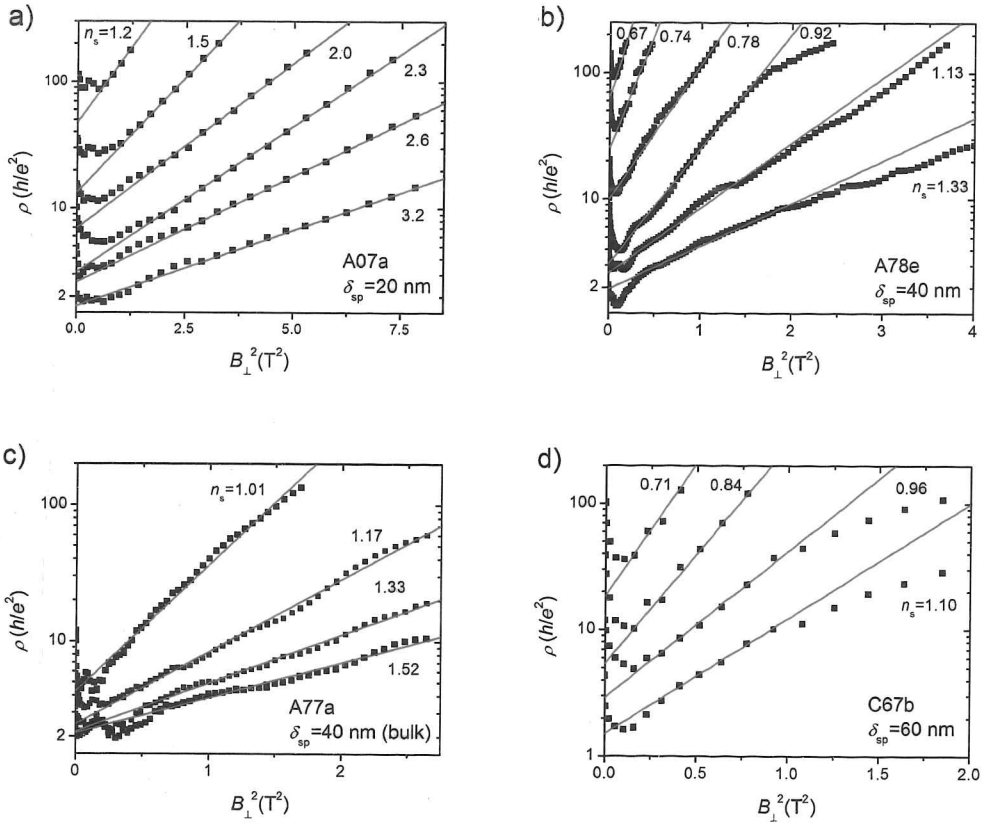

Figure 5.2: Resistivity ρ in logarithmic scale versus $B_\perp^2$ (perpendicular) for four devices from different wafers with δ_{sp} varying from 20 nm to 60 nm, including both δ- and bulk-doped heterostructures. All measurements were taken at $T = 300\,\mathrm{mK}$. The densities for each data set are given in units of $10^{10}\,\mathrm{cm}^{-2}$. A clear exponential $B_\perp^2$-dependence is observed over up to more than one order of magnitude in resistivity. The slopes of the linear fits reveal the coefficient α in the exponential, the y-intercept gives the MR prefactor ρ_B [92].

40 and 60 nm and one bulk-doped wafer with δ_{sp}=40 nm. Device dimensions are $L \times W \cong 2-3\,\mu m \times 8\,\mu m$. Measurements are restricted to electron densities where the minimum resistivity is $\gtrsim 2h/e^2$, in order to ensure that electrons are localised. In this regime, all devices show a MR according to Eq. (5.1) with an exponential $B_\perp^2$-dependence of ρ over up to more than one order of magnitude in resistance. This strongly suggests that transport, indeed occurs by hopping and an analysis of the data in the framework described in Sect. 5.1 is adequate. Alternative transport mechanisms will be discussed in Sect. 5.5.

5.2.2 Analysis

This section focuses on the analysis of the coefficient α in the exponential, which is determined by the slope of the linear fits to the resistivity in logarithmic scale vs. $B_\perp^2$ as shown in Fig. 5.2. A first striking observation is that the slope α depends strongly on electron density and *decreases* with *increasing* n_s for all devices. According to Eq. (5.2), α contains two parameters that may not be constant, namely r_{hop} and ξ. The localisation length ξ is proportional to α, hence, if the n_s-dependence of α was caused by a change in ξ, the localisation length would have to decrease with increasing electron density. Such a behaviour is completely unexpected: In a non-interacting scenario, in the regime of very low densities, where localisation is completely determined by trapping of individual electrons by local minima in the background disorder potential, one would expect a ξ independent of electron density. With increasing density, stronger screening of the disorder potential can lead to an increase in ξ (e.g. Ref. [93]), but it is certainly not expected to decrease as the observed behaviour of α would suggest.

The other possible explanation is a decrease in the average hopping distance r_{hop} with increasing n_s. However, again, a single-particle picture fails to explain why this should happen. In the low density limit, the hopping distance should be independent of the electron density. With increasing n_s, some of the trap sites might get screened, or occupied and, hence, unavailable. This would lead to a larger hopping distance with increasing electron density, again leading to the opposite trend than experimentally observed.

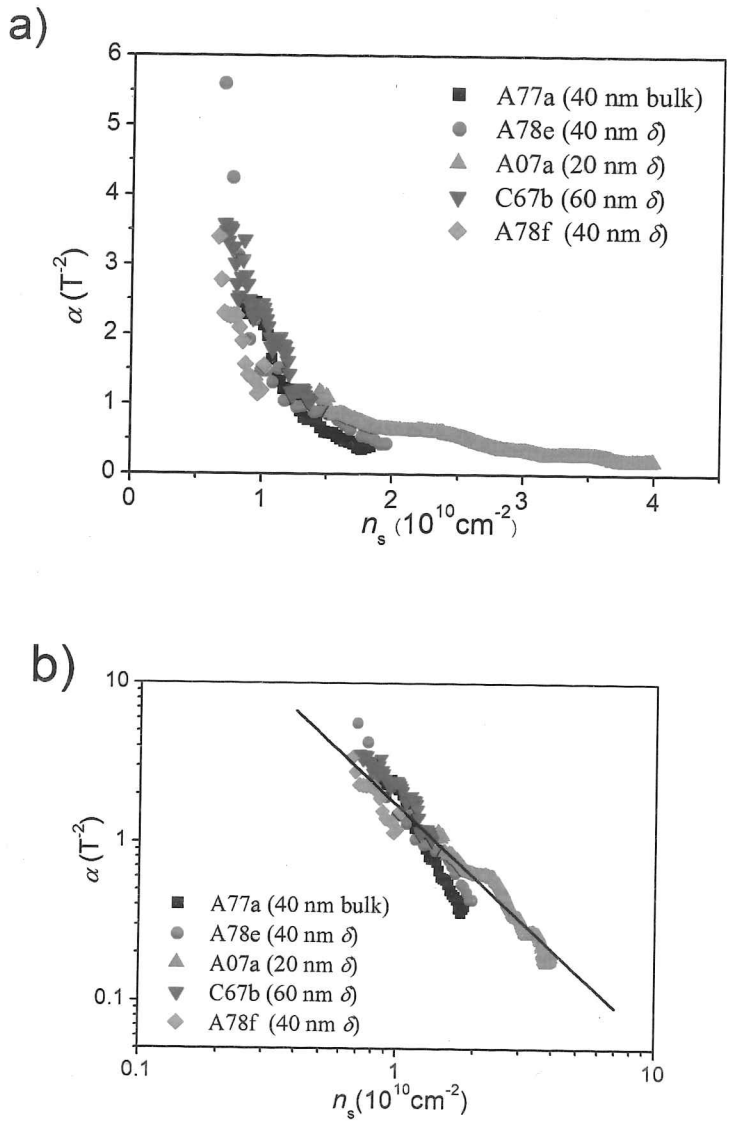

Figure 5.3: a) Coefficient α as a function of electron density for five different devices with spacer width varying from 20 nm to 60 nm, all data taken at T=300 mK. α collapses onto one universal curve, determined by density only, independent of disorder strength. b) The same data as a), but on a log-log scale. The slope of the solid line is -3/2, implying $\alpha \propto n_s^{-3/2}$ or, assuming a constant ξ, $r_{\mathrm{hop}} \propto r_{\mathrm{ee}}$.

An understanding of the n_s-dependence of α requires a more quantitative analysis. In Fig. 5.3 a), α is shown as a function of electron density for five devices made from four different wafers ($\delta_{sp} = 20 - 60\,\text{nm}$). Remarkably, α from different samples are strongly correlated with the magnitude apparently only determined by n_s and following an universal function, independent of disorder. At stronger disorder (e.g. A07a), localisation occurs at lower n_s, resulting in a lower α, while at lower disorder (e.g. C67b) localisation occurs at higher n_s, yielding a larger magnitude of α.

As discussed above, a single-particle picture of transport and localisation fails to explain the qualitative density dependence of α for individual devices. The strong correlation of α from sample to sample gives further evidence of this finding. It makes a purely disorder associated origin of r_{hop} clearly unlikely. For example, taking $r_{hop} \approx \delta_{sp}$ (the shortest disorder length-scale expected in the 2DES, see Sect. 2.2.3) would lead to distinct sets of α for wafers with different δ_{sp}. On the other hand, the wide range of doping concentrations, compensations of the dopants, and the use of both bulk- and δ-doped wafers excludes a possible distinct length-scale within the doping layer as the origin of r_{hop}. However, in the context of strong electron-electron correlations, another relevant length-scale is $r_{ee} \cong 1/\sqrt{n_s}$. It is the nearest neighbour separation of the electrons assuming they are arranged on a square lattice. For simplicity, r_{ee} is referred to as mean electron-electron separation and its physical implications are discussed below.

In case of tunnelling events over a mean electron-electron separation, i.e. $r_{hop} \approx r_{ee}$, Eq. (5.2) describes both absolute magnitude and the n_s-dependence of α quantitatively. Using $r_{hop} \approx 1/\sqrt{n_s}$, Eq. (5.2) leads to $\alpha \propto n_s^{-3/2}$, which is observed experimentally (solid line in Fig. 5.3 b)). Allowing for sample-to-sample variation, it was found that $\alpha = (1.7 \pm 0.5) \times 10^{21}/n_s^{3/2}\ \text{T}^{-2}$ from which, using Eq. (5.2), one obtains $\xi = 9.0 \pm 2.6\,\text{nm}$. This value is close to the effective Bohr radius a_B^* in GaAs ($\approx$10.5 nm). Here, a value of $C = 1$ was assumed, which cannot be rigorously justified. However, the theoretical predictions all lie within a deviation of 50% from $C = 1$, and using any other value would not qualitatively alter the picture.

In a summary of the analysis so far, we have seen that α is only determined by the electron density and not disorder. This behaviour can be quantitatively

described over nearly one order of magnitude in n_s and two orders of magnitude in α by assuming hopping transport with a constant localisation length $\xi \approx a_B^*$ and a density dependent hopping length $r_{hop} \approx r_{ee}$.

5.2.3 Discussion

In the following, the physical scenarios that could lead to an electron separation-dependent hopping transport are discussed. It is evident that any explanation of the finding that $r_{hop} \approx r_{ee}$, must take significant electron-electron interactions into account. A natural explanation is that of a self-localised electron solid as discussed in Sect. 2.5. This may be anything from a strongly disordered electron glass to a disorder stabilised, pinned Wigner crystal with high regularity. For a strongly disordered ES, there is no well defined nearest-neighbour separation, but electrons will try to avoid each other and generally would not be much closer than r_{ee}. This condition also restricts the hopping path and, as Fig. 5.4 a) shows schematically, it seems reasonable that the closest available sites an electron can hop to, will be $O[r_{ee}]$ away.

For the case of a pinned Wigner crystal a more quantitative discussion is possible. Here, transport would occur by hopping of point defects such as interstitials or vacancies. The WC is arranged in a hexagonal lattice with lattice constant $a_0 = 1.07/\sqrt{n_s}$. The hopping distance of a vacancy is $r_{hop}^v = a_0$, while that of a interstitial is slightly shorter, $r_{hop}^i = 0.87 \times a_0 = 0.93/\sqrt{n_s}$. Both values lie well within the error margin of the measured r_{hop}. This means that transport mediated by defects in a WC could explain the observed n_s-dependence of r_{hop} very well.

Formation of a Wigner crystal in presence of optimal disorder has, indeed, been suggested at $r_s \approx 7.5$ (see Sect. 2.5.1 and [20]), which is not very far from the range of $r_s \approx 2.7 - 6.5$ in which the unusual hopping behaviour was observed experimentally. The results described here do not allow for a definite conclusion about the degree of order between the localised electrons. However, the results obtained from the temperature dependence in the same regime suggest, that a rather strong ordering might be present. This is presented in Chapt. 6, where a more detailed discussion of the motion of defects in an electron solid is also given.

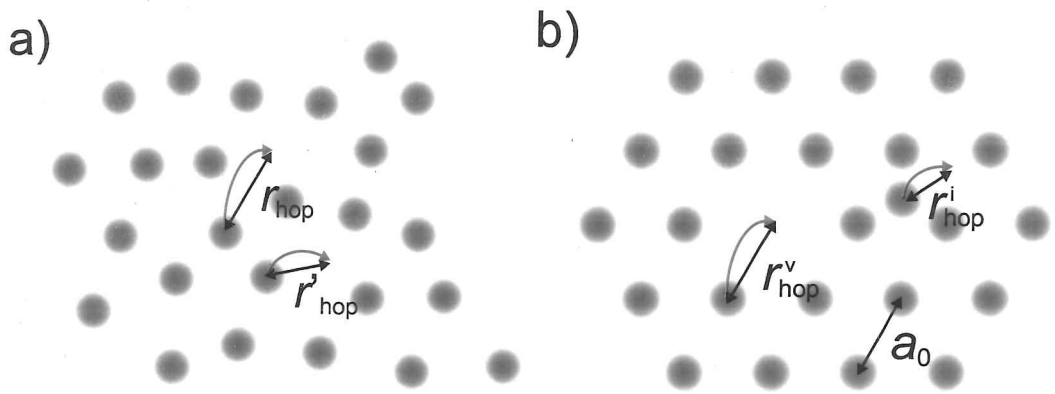

Figure 5.4: a) Schematic illustration of hopping in a Wigner glass. Two possible hopping events over the distances r_{hop} and r'_{hop} are indicated. b) Hopping of defects in a Wigner crystal over the distance $r^{\mathrm{i}}_{\mathrm{hop}}$ (interstitial) and $r^{\mathrm{v}}_{\mathrm{hop}}$ (vacancy). The lattice constant of the hexagonal crystal is indicated as a_0.

The interpretation above assumes a constant or weakly changing localisation length $\xi \approx a_{\mathrm{B}}^{*}$ and a wave function of the form $\psi(r) \propto \exp(-r/\xi)$. The success of the analysis, in particular, the clear exponential $B_{\perp}^{2}$-dependence of ρ and the sample-to-sample consistency justify these assumptions. The intricate interplay of confinement arising from the magnetic potential, disorder potential and electron-electron interactions is expected to determine $\psi(r)$. However, how this could lead to an universal localisation length $\xi \approx a_{\mathrm{B}}^{*}$ is presently not understood.

5.3 Universality and Quantisation of Hopping Prefactor

The hopping prefactor ρ_{B} as defined in Eq. (5.1) reveals independent information about r_{hop} and ξ which allows for a verification of the results discussed in Sect. 5.2.

If those findings were true, i.e. $r_{\mathrm{hop}} \approx 1/\sqrt{n_{\mathrm{s}}}$ and $\xi \approx a_{\mathrm{B}}^*$, the electron density dependence of the prefactor should be $\rho_{\mathrm{B}}(n_{\mathrm{s}}) \propto \exp(2/\sqrt{n_{\mathrm{s}}}a_{\mathrm{B}}^*)$, according to Eq. (5.3). Fig. 5.5 a) shows ρ_{B} as a function of r_{ee} for various devices with spacer width $\delta_{\mathrm{sp}} = 20 - 60\,\mathrm{nm}$. As the solid lines confirm, in the low density/ high resistivity regime, ρ_{B} follows the expected behaviour in a satisfactory manner despite some scatter of the data points. This is a good check of consistency with the results discussed above. However, at lower n_{s}, ρ_{B} deviates from the exponential behaviour and saturates to a weaker r_{ee}-dependence. The saturation value is found to be $\rho_{\mathrm{B}} \sim 1 - 2h/e^2$ for all devices.

A striking observation becomes clear in Fig. 5.5 b), where the same data as in a) is plotted in terms of absolute resistance $R = \rho \times L/W$: The saturation value turns out to be the universal value of $R_{\mathrm{B}} \approx h/2e^2$ for all devices.

In order to verify this surprising result, a set of devices from the same wafer and mesa width W, but varying gate length L was measured. This leads to a different ratio between ρ_{B} and R_{B} for each device. Fig. 5.6 shows a direct comparison of the obtained hopping prefactors in terms of resistance (a)) and resistivity (b)). While R_{B} exhibits a practically coinciding saturation, ρ_B varies strongly in its absolute saturation value. This results confirms that the saturation value is, indeed, universal in resistance rather than resistivity.

In Fig. 5.7, R_B is again plotted for four devices, all from different wafers. The gate voltage where the first deviation from the exponential behaviour occurs has been subtracted in the x-axis in order to get a better representation of the data. Here, another observation becomes clear: Apart from the saturation at $R_{\mathrm{B}} \approx h/2e^2$ another plateau is formed at lower electron density at $R_{\mathrm{B}} \approx h/e^2$. In other words, R_{B} is quantised in units of the quantum of resistance $h/2e^2$. In some cases, further features were observed at higher resistances. However, they were not clear enough to be assigned to a certain quantisation value. On the other hand, in the regime of higher n_{s}, where lower resistance plateaux might be expected, strong localisation and hopping transport break down, making an analysis of the hopping prefactor impossible.

According to Eq. (5.3), R_{B} should depend on temperature exponentially. However, as Fig. 5.8 shows, R_{B} is virtually temperature independent between 300 mK and 1.2 K. This is most likely related to the saturation in the temperature dependence of resistance at low T discussed in Chapt. 6. There, it is shown

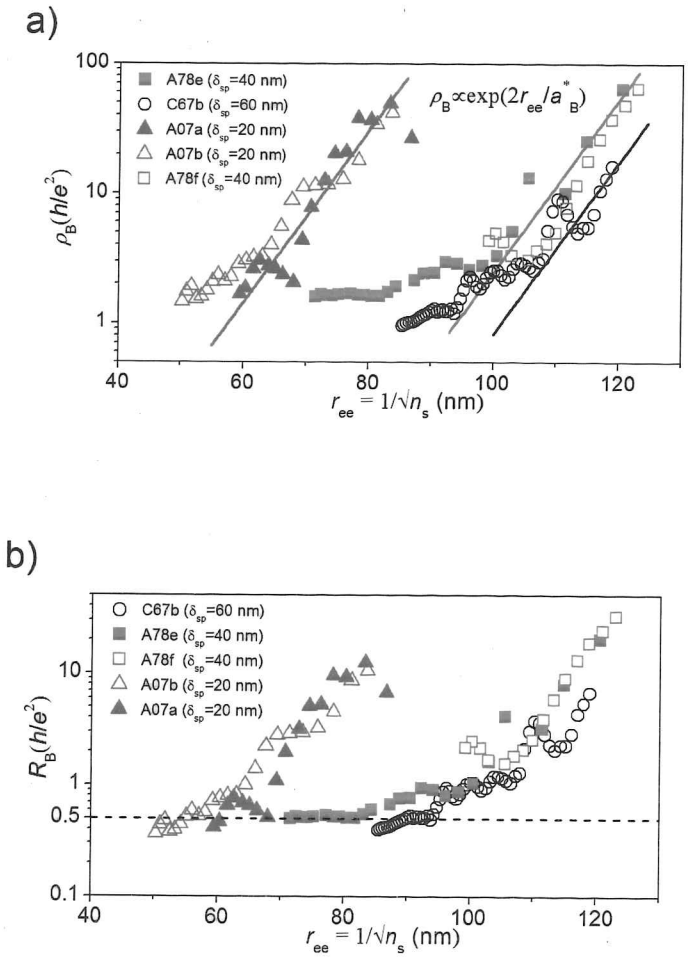

Figure 5.5: a) Hopping MR prefactor ρ_B in terms of resistivity as a function of r_{ee}. At large r_{ee} (low electron density), the expected behaviour $\rho_B \propto \exp(2r_{ee}/a_B^*)$ is confirmed satisfactorily (solid lines), while at smaller r_{ee} a saturation at $\rho_B \sim 1 - 2h/e^2$ occurs. b) Same data as a), but in terms of absolute resistance. It becomes clear that the saturation occurs at $R_B \approx h/2e^2$ (dashed line).

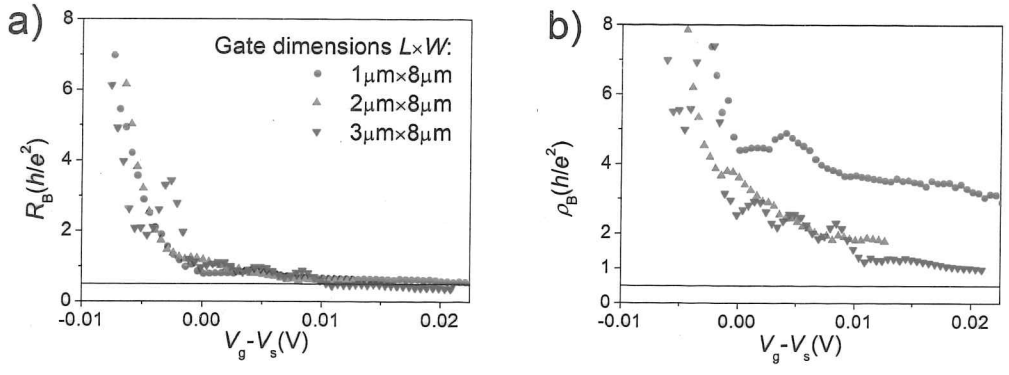

Figure 5.6: Direct comparison of hopping MR prefactor for various device dimensions in terms of resistance a) and resistivity b). The saturation value is independent of the gate length when expressed in resistance, while it varies strongly when shown in resistivity. For better representation, the gate voltage V_s where deviation from exponential behaviour first occurs for each device, has been subtracted from the absolute value of gate voltage V_g. The legend in a) applies to both panels. Devices are C67a and C67b.

that the (saturated) low-temperature behaviour may be explained as thermally assisted tunnelling between nearest neighbour states with the average energy difference between states $E_t \ll k_B T$. This means that $\exp(E_t/k_B T)^p \approx 1$ and, hence, Eq. (5.3) becomes

$$\rho_B \approx \rho_0 \exp(2r_{hop}/\xi), \tag{5.6}$$

which explains the temperature independence of ρ_B. In this situation, ρ_B is equal to the hopping prefactor ρ_t in exponential temperature dependence $\rho(T) = \rho_t \exp(E_t/k_B T)^p$, which has been investigated for the case where $E_t \gg k_B T$. Experimentally, an universal value of $\rho_t \cong h/e^2$ was observed in macroscopic 2DES in silicon [9] or at $\rho_t \cong h/e^2$ and $\rho_t \cong h/2e^2$ in AlGaAs heterostructures with very small spacer $\delta_{sp} = 0.6\,\mathrm{nm}$ [10].

If the tunnelling is assisted by electron-phonon scattering, a prefactor $\rho_t \gg h/e^2$ is expected [95]. However, it had long been suggested that hopping as-

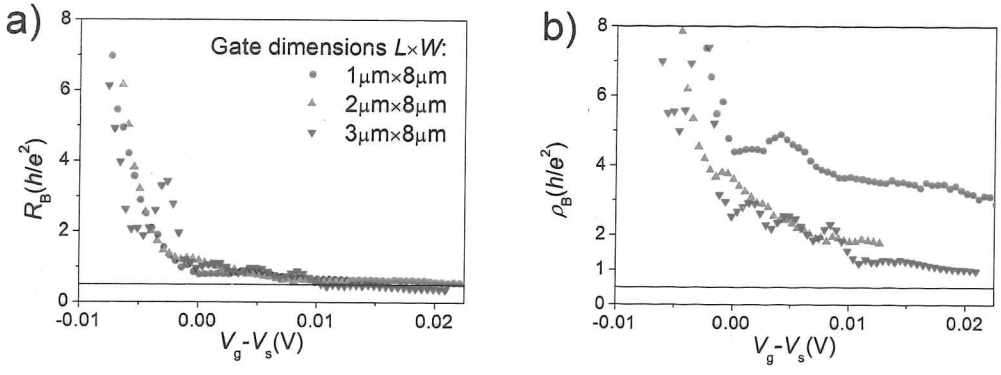

Figure 5.6: Direct comparison of hopping MR prefactor for various device dimensions in terms of resistance a) and resistivity b). The saturation value is independent of the gate length when expressed in resistance, while it varies strongly when shown in resistivity. For better representation, the gate voltage V_s where deviation from exponential behaviour first occurs for each device, has been subtracted from the absolute value of gate voltage V_g. The legend in a) applies to both panels. Devices are C67a and C67b.

that the (saturated) low-temperature behaviour may be explained as thermally assisted tunnelling between nearest neighbour states with the average energy difference between states $E_t \ll k_B T$. This means that $\exp(E_t/k_B T)^p \approx 1$ and, hence, Eq. (5.3) becomes

$$\rho_B \approx \rho_0 \exp(2r_{hop}/\xi), \tag{5.6}$$

which explains the temperature independence of ρ_B. In this situation, ρ_B is equal to the hopping prefactor ρ_t in exponential temperature dependence $\rho(T) = \rho_t \exp(E_t/k_B T)^p$, which has been investigated for the case where $E_t \gg k_B T$. Experimentally, an universal value of $\rho_t \cong h/e^2$ was observed in macroscopic 2DES in silicon [9] or at $\rho_t \cong h/e^2$ and $\rho_t \cong h/2e^2$ in AlGaAs heterostructures with very small spacer $\delta_{sp} = 0.6\,\mathrm{nm}$ [10].

If the tunnelling is assisted by electron-phonon scattering, a prefactor $\rho_t \gg h/e^2$ is expected [95]. However, it had long been suggested that hopping as-

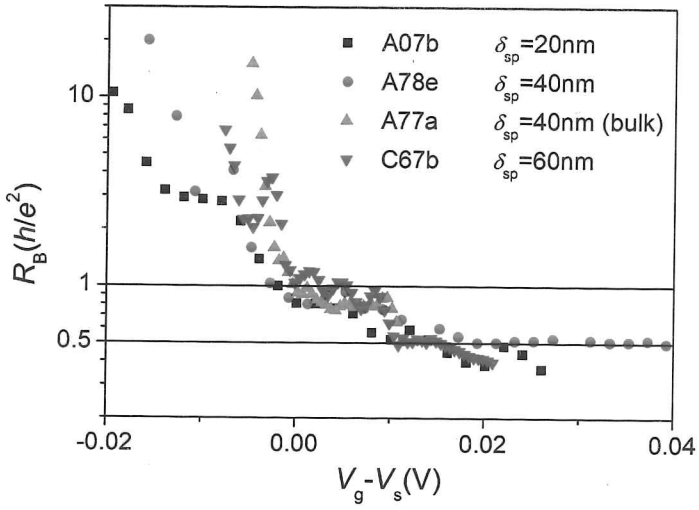

Figure 5.7: R_B for devices from four different wafers showing a quantisation with plateaux at the values $R_B \approx h/2e^2$ and h/e^2. For better representation, the gate voltage V_s, where deviation from exponential behaviour first occurs for each device, has been subtracted from the absolute value of gate voltage V_g.

sisted by electron-electron scattering may lead to a prefactor $\sim h/e^2$ [95]. A theoretical justification was not given in Ref. [95], but the reasoning must be that the coupling in electron-electron scattering is much stronger than in electron-phonon scattering, since phonons are essentially vibrations on uncharged atoms.

Recent theoretical work has, indeed, predicted a prefactor $\rho_t \cong h/e^2$ in hopping transport assisted by excitations of strongly overlapping localised electron states [96]. Calculations for scattering between electrons (or charged defects) and lattice vibrations in an electron solid were not done, but a similar result would not be unexpected [96]. However, a quantisation at h/e^2 and $h/2e^2$ is not predicted in this theory. Nevertheless, the experimental results described in this section provide further evidence of a strongly interacting electronic phase or possibly even a electron solid.

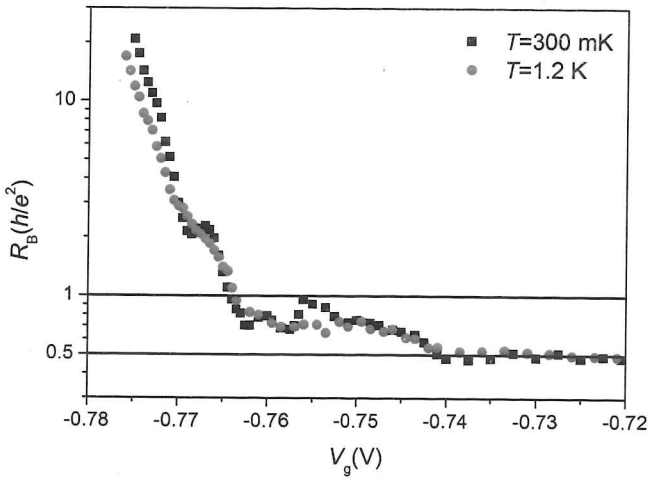

Figure 5.8: Magnetoresistance prefactor R_B at the temperatures $T = 300\,\mathrm{mK}$ and $T = 1.2\,\mathrm{K}$ for device A78e. R_B is virtually temperature independent within this temperature range [94].

Despite all this, the question remains, why the saturation is universal in resistance rather than resistivity. The apparent insensitivity to the length of the gate may be explained by a correlated hopping, leading to a length-independence if the device is smaller than the correlation length, which may be true in mesoscopic devices. Even in this case one would expect a dependence on the width of the device. A systematic investigation of the dependence of ρ_B or R_B on mesa width was not done, but it seems an unlikely coincidence that it is the choice of a width of $8\,\mu\mathrm{m}$ that leads to the observed saturation value. The independence on device width could possibly be explained by formation of some kind of quasi one-dimensional stripe as dominating transport path, be it caused by disorder or a fundamental interaction effect [51–53]. However, this would by no means explain the observation fully, in fact, it would be difficult to account for many other observations described in this thesis in such a picture.

5.4 Other Aspects of Magnetoresistance

5.4.1 Low Field Negative Magnetoresistance

The devices under investigation generally showed a clear negative magnetoresistance at lowest fields (see Sect. 5.4.3 for exceptions). This is shown for a set of four devices in Fig. 5.9, where a linear rather than quadratic $B_\perp$-scale was chosen in order to highlight the low-field part of the data. Tripathi and Kennett (TK) have discussed negative MR in insulators, which has been studied in literature in two contexts [97]. One possible origin of negative MR is the suppression of destructive interference between different trajectories between starting and final point of a hopping event. This has been predicted to lead to a linear negative MR $[\rho(B_\perp)-\rho(0)] \propto |B_\perp|$ or quadratic MR $[\rho(B_\perp)-\rho(0)] \propto B_\perp^2$ depending on the strength of the field [97]. The other mechanism, which would be relevant in the droplet picture proposed by TK (see discussion in Sect. 5.5), arises from an increase of the wave function overlap between adjacent electron droplets. This model also predicts a quadratic negative MR $[\rho(B_\perp)-\rho(0)] \propto B_\perp^2$. However, the magnetoresistance observed here, does not seem to follow any of these predictions. As Fig. 5.10 shows, in device C67b, a rather clear $B_\perp^2$-dependence of the conductivity $\sigma = 1/\rho$ is observed, i.e. a negative magnetoresistance of the form $[\rho(B_\perp) - \rho(0)] \propto B_\perp^{-2}$. The author is unaware of any theoretical work that predicts such a behaviour.

Another aspect of the negative MR is the position $B_{\min}$ in magnetic field of the resistance minimum. In all cases a slight increase in the position of this minimum with increasing electron density is observed (Fig. 5.9). This could be explained simply by the observed decrease in α, which would mean that a higher magnetic field is required for the exponential increase in resistance to become dominant over the negative MR. However, we note that in all devices the minimum occurs at approximately $B_{\min} \approx hn_s/e$ (indicated by arrows in Fig. 5.9), which corresponds to a Landau level filling factor $\nu = hn_s/B_\perp e \approx 1$. Best agreement occurs at lowest densities, while larger deviations are generally observed at higher n_s. In view of the finding that both α and ρ_B are determined by r_{ee}, this observation has a interesting physical interpretation. Namely, it means that there is one magnetic flux quantum ϕ_0 within an area of r_{ee}^2. This

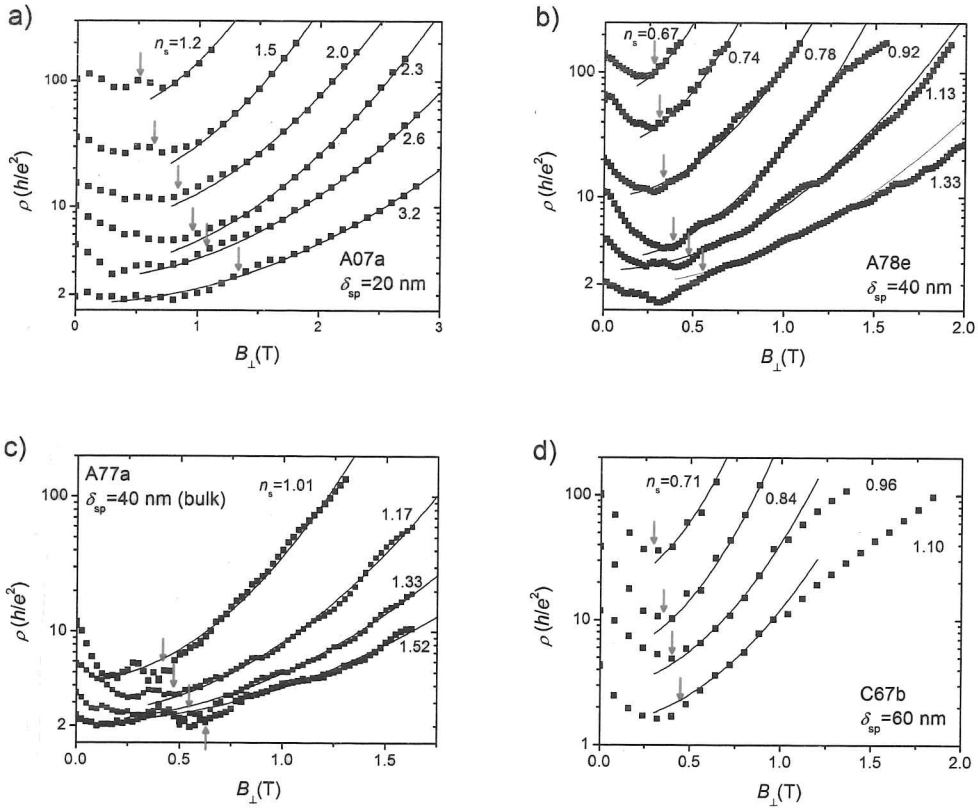

Figure 5.9: The same data as Fig. 5.2, but on a linear $B_\perp$-scale which highlights the low-field parts of the data. A strong negative MR is observed in all devices with the magnetic field at which the minimum in resistivity occurs increasing with increasing n_s. Arrows indicate $B_\perp = hn_s/e \Leftrightarrow \nu = 1$ [92].

suggests that the negative MR may be related to the destruction of interference in a loop of area r_{ee}^2. Indeed, this is the expected area of the smallest loop of a defect undergoing a random walk in an electron solid. This observation supports the picture of transport mediated by defects in an ES.

In conclusion of this section, an interesting low field MR has been observed, but a good understanding of the behaviour would require further experimental and theoretical investigations which are beyond the scope of this thesis.

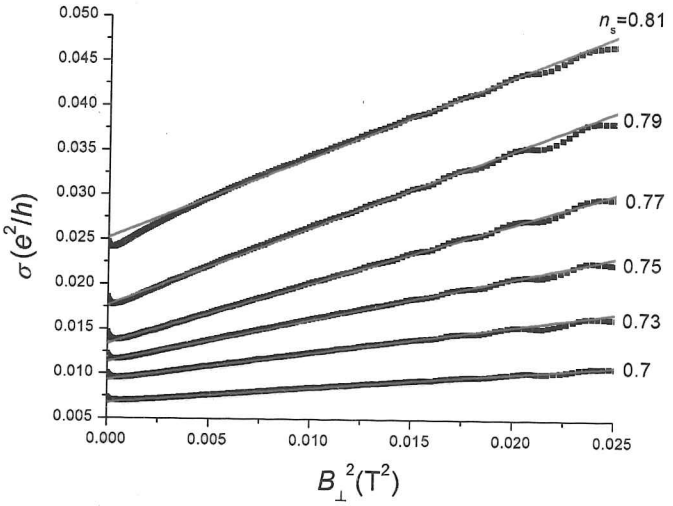

Figure 5.10: Low field magnetocondivity $\sigma = 1/\rho$ of device C67b on a $B_\perp^2$-scale. The solid lines are linear fits, demonstrating a clear quadratic $B_\perp$-dependence of G and, hence, a negative magnetoresistivity of the form $[\rho(B_\perp) - \rho(0)] \propto B_\perp^{-2}$.

5.4.2 High Field Magnetoresistance

As discussed in Sect. 5.1, at high magnetic fields the exponential $B_\perp^2$-dependence of ρ should turn into a exponential $B_\perp$-dependence. In this regime, relations (5.4) and (5.5) provide another way of estimating the average hopping distance r_{hop}. This estimate is independent of the zero field localisation length, because it is done in the regime where the localisation is dominated by the magnetic confinement.

Indeed, an exponential $B_\perp$-dependence at high fields was observed in many devices. One example is shown in Fig. 5.11 a). The onset of $B_\perp$-dependence occurs at $B_\perp \approx 2.5\,\mathrm{T}$, a value that is roughly independent of electron density. The high field behaviour of magnetoresistance is expected for $l_\mathrm{B} \ll \xi$. This means that the observed transition field, which corresponds to $l_\mathrm{B} \approx 1.5 \times a_\mathrm{B}^*$, is lower than the expected value for a localisation length $\xi \cong a_\mathrm{B}^*$. This would suggest that the zero field localisation length is in fact larger than a_B^*, contradicting the conclusion of Sect. 5.2. However, the deviation is not so

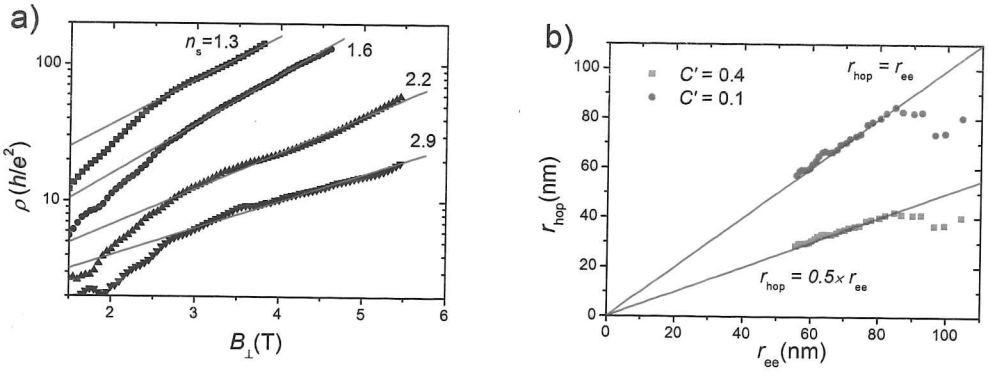

Figure 5.11: a) High field magnetoresistance, showing a exponential $B_\perp$-dependence above a critical value. The solid lines are linear fits to the data and their slopes correspond to β. Electron densities are indicated in units of $10^{10}\,\mathrm{cm}^{-2}$. b) Values of r_{hop} as a function of r_{ee} as extracted from β using Eq. (5.5). While using the theoretically predicted $C' \approx 0.4$, leads to the relation $r_{\mathrm{hop}} \cong 0.5 \times r_{\mathrm{ee}}$, the best agreement $r_{\mathrm{hop}} \cong r_{\mathrm{ee}}$ is found for $C' \approx 0.1$. The proportionality between r_{hop} and r_{ee} is nicely confirmed. (Device A77a)

strong that a definite statement could be made. The weak n_s-dependence gives some confirmation of an approximately constant localisation length, since a strong change in ξ should lead to a change in the threshold where the magnetic length becomes dominant over the localisation length.

As Fig. 5.11 a) shows, the coefficient β, which corresponds to the slope of the linear fits, follows qualitatively the behaviour that is expected from the analysis of α, i.e. β decreases with increasing density as expected if $r_{\mathrm{hop}} \cong r_{\mathrm{ee}}$. A more quantitative analysis is shown in Fig. 5.11 b), where r_{hop} has been calculated using relation (5.5) and plotted as a function of r_{ee}. The choice of C' gives some uncertainty for r_{hop}. Following Ref. [90] one would expect $C' \approx 0.4 \times C = 0.4$. As Fig. 5.11 b) shows, using this value leads to a $r_{\mathrm{hop}} \cong 0.5 \times r_{\mathrm{ee}}$. For a good agreement, $r_{\mathrm{hop}} \cong r_{\mathrm{ee}}$, one has to use $C' = 0.1$. These deviations lie within the uncertainty of C'. While for a good quantitative confirmation (or rejection) of the equality $r_{\mathrm{hop}} \cong r_{\mathrm{ee}}$, a better estimate of C' would be desirable, the results

in Fig. 5.11 b) nevertheless nicely confirm that r_{hop} is proportional to r_{ee}, a finding that is independent of the value C' or any other unknown variables.

One has to add at this point, that device A77a was the only one that showed such a clear linear r_{ee}-dependence of r_{hop}. Most other devices did show a rough agreement with $r_{\mathrm{hop}} \cong r_{\mathrm{ee}}$ in trend and absolute magnitude, but r_{hop} deduced from β often showed strong oscillations. These oscillations may be related to the strong resistance oscillations occurring at high magnetic fields in mesoscopic devices, as discussed in Chapt. 7. Indeed, device A77a showed unusually weak oscillations. In view of this limited reproducibility, one should not overrate the results presented in this section.

5.4.3 Very Strong or Weak Disorder Devices

In strongly disordered macroscopic 2D systems hopping magnetoresistance of the form of Eq. (5.1) was first observed in the impurity band formed at the inversion layer of sodium-doped MOSFETs [91]. Later, the same was achieved in hopping transport within δ-doping layers in GaAs [17]. In this case, a good agreement with the theoretical prediction for the coefficient α (Eq. (5.2)) was found, assuming the localisation length to be $\xi \cong a_{\mathrm{B}}^*$ and $r_{\mathrm{hop}} \approx 1/\sqrt{N_\delta}$, with N_δ the dopant concentration. This is in contrast to the results for high mobility mesoscopic devices discussed in Sect. 5.2, where α was found to be independent of disorder and only determined by n_{s}.

In case of very weak disorder, i.e. $\delta_{\mathrm{sp}} = 80\,\mathrm{nm}$ (Device T46a), the low field magnetoresistance appears to be qualitatively different from the more disordered devices discussed in the previous sections of this chapter. An exponential $B_\perp^2$-dependence of resistance appears only at very low fields and is not very clear (Fig. 5.12). When trying to fit Eq.(5.1) to the data nevertheless, no clear trend in the slope (i.e. α) is observed. Also, a negative magnetoresistance at smallest B is absent in most cases. This result shows that finding the right amount of disorder is crucial in experiments performed for this thesis. In the suggested picture of transport through hopping of defects in a disorder stabilised electron solid, one could explain the different behaviour of MR by the absence of the electron solid because the disorder is too weak to stabilise the solid phase. Alternatively, it could be that the phase still exists, but that the

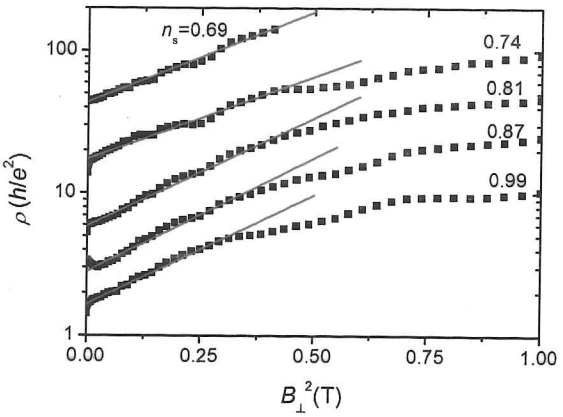

Figure 5.12: Low field magnetoresistance in a low disorder device with spacer width δ_{sp}=80 nm (Device T46a). An exponential $B_\perp^2$-dependence appears only at very low fields, if at all. The slope α does not show the clear decreasing trend with increasing electron density as it does in the more disordered cases. Electron densities in the legend are in units of $10^{10}\,\mathrm{cm}^{-2}$ [94].

upper limit in magnetic field of the exponential $B_\perp^2$-dependence is very low. This could be due to a larger localisation length or a different wave function from the one used to derive Eq. (5.1). More generally, the different behaviour of the low disorder case may be explained by a different appearance of the same physical scenario, or by a different transport or localisation mechanism altogether.

5.5 Alternative Interpretations

5.5.1 Direct Tunnelling

In view of the mesoscopic dimensions of the devices, one may ask if transport could actually occur by direct tunnelling between the conducting Fermi seas on either side of the gate. However, apart from the fact that it is not obvious how this could explain the observations described in this chapter (or the other

chapters of this thesis), there are several reasons that make direct tunnelling a very unlikely transport mechanism through the gate.

First of all, the author is unaware of observation of direct tunnelling in comparable systems with tunnelling lengths in the order of microns as it would have to be the case in the devices with gate lengths of up to $L \approx 4\,\mu$m. The tunnelling probability becomes extremely small over such distances, as it decreases exponentially with tunnelling length. Additionally, from the density measurements, we know that the area under the gate is by no means completely depleted, but that hundreds to thousands of electrons remain in the gated area even in the smallest devices at lowest densities. It seems obvious that it is more likely for electrons to jump in and out of the localised area rather than going across it in a single tunnelling event.

The observed exponential increase with a perpendicular magnetic field is strong evidence that wave function overlap plays a critical role in transport. This is not expected in direct tunnelling. It would, of course, be expected in tunnelling via a few impurities states. However, in this case, resonance peaks should occur as a function of gate voltage, when the energy of the impurity state is aligned with the Fermi energy in the leads [98]. No sign of such resonant tunnelling has been observed in any device.

5.5.2 Hopping between Electron Droplets

As briefly mentioned in Sect. 5.4.1, TK have suggested an alternative mechanism to explain the magnetoresistance described in Sect. 5.2 [97]. They considered formation of electron droplets at minima in the disorder potential in the non-linear screening regime of δ-doped GaAs/AlGaAs 2DES. They provide detailed calculations of droplet radius, inter-droplet distance and droplet localisation length for a range of electron densities similar to those where experiments presented here were carried out. It is argued that the number of electrons in a droplet (≈ 6), depends only weakly on the average electron density and that extra electrons are accommodated by increasing the density of droplets. This means that the separation between droplet centres decreases with increasing n_s.

The calculation of the suppression of the tunnelling probability between droplets caused by shrinking of the localisation length in a perpendicular magnetic field leads to a magnetoresistance of the form of Eq. (5.1) with

$$\alpha_{\mathrm{TK}} = A/n_{\mathrm{s}}^{3/2}, \tag{5.7}$$

where A is only weakly dependent on n_{s}. This is in qualitative agreement with the observed n_{s}-dependence of α. A depends on the doping concentration as $n_\delta^{3/4}$, which means that device C67b should exhibit α approximately 0.4 times smaller than other devices at the same electron density. Such a deviation is not observed experimentally, but it might be within the experimental error margin. It would be interesting to know a dependence of A on spacer width, however, these values cannot be extracted easily from the work of TK.

A numerical estimate of A for the case of $\delta_{\mathrm{sp}} = 50\,\mathrm{nm}$ is given by TK. They find a deviation of more than 1.5 orders of magnitude from the observed value at $n_{\mathrm{s}} = 10^{10}\,\mathrm{cm}^{-2}$. The error gets slightly smaller at higher densities, but stays above one order of magnitude. The authors state that including effects of partial ionisation of the dopants make the agreement even worse. This means that the error should be even larger, since devices used here are generally highly compensated, as discussed in Sect. 3.3.3. In view of this large quantitative discrepancy between theory and experiment, the author doubts that the picture suggested by TK is the correct description of the experimental results. Nevertheless, it should not be completely dismissed, as a better estimate of some of the quantities involved may (or may not) lead to a better agreement.

The transport picture introduced by TK has also been extended to explain magnetic field induced resistance oscillations and the T-dependence of resistance [99]. This will be discussed in the concerning chapters (6 and 7).

Chapter 6

Temperature Dependence of Resistivity

This chapter discusses the temperature dependence of resistivity in the strongly localised regime of mesoscopic 2DES. An unexpected behaviour is reported where at higher temperatures the resistivity increases exponentially with $1/T$ as expected, but flattens or even reverses as the temperature is lowered further. This indicates a temperature driven insulator-to-metal transition, with an insulating phase at high and a metallic phase at low T. The phenomenon persists even when the resistivity of the system greatly exceeds the quantum of resistivity h/e^2. This is an unprecedented observation in 2D, which is fundamentally different from any previously reported putative metal-insulator transitions.

In the following, the terms "metallic" will be used for a positive temperature coefficient of resistivity $d\rho/dT > 0$ and "saturated" for the weak, but non-metallic T-dependence, as opposed to "insulating" for an exponential behaviour. It should be noted that the denotations "metallic", or "insulating" as used in this chapter cannot be identified with a metallic or insulating ground state, respectively: An insulating ground state is defined through a diverging resistance as T approaches absolute zero, while the resistance of a metallic ground state remains finite at $T = 0$, but need not show a metallic behaviour as defined above.

6.1 Comparison of Macroscopic and Mesoscopic Devices

Figs. 6.1 a)-c) show typical temperature traces for one macroscopic device and two mesoscopic ones with approximately the same resistivity at lowest temperature. All the devices had the same spacer width δ_{sp}=40 nm. The macroscopic device shows the expected exponential behaviour down to the lowest temperatures. By contrast, the mesoscopic devices show an exponential behaviour only at high T, followed by a range where the resistivity increases only slowly or even decreases as the temperature is lowered.

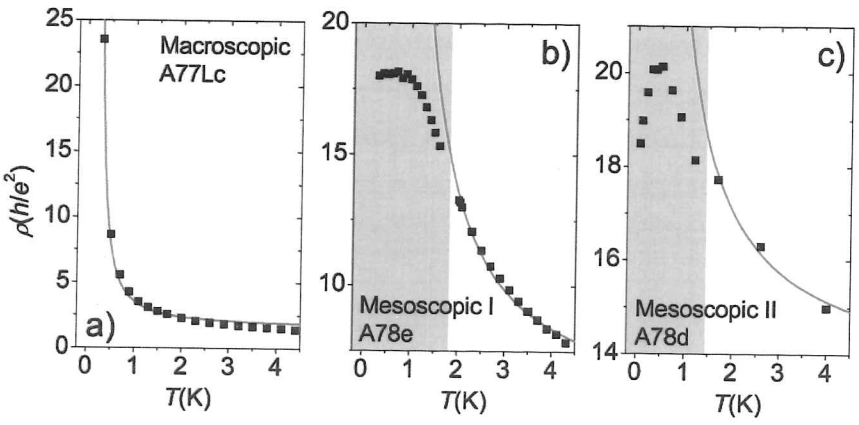

Figure 6.1: Comparison of temperature dependence of resistivity for two mesoscopic devices (W = 8 μm, L = 2, 0.5 μm for device I and II, respectively) with a macroscopic device (100 μm × 900 μm) from wafers with the same spacer width (40 nm) in the same regime of resistivity at lowest temperatures. While a clear saturation or downturn of the resistivity at lowest T occurs in the mesoscopic devices, the macroscopic device shows an exponential increase to the lowest temperature. The solid lines are fits of the form $\rho = \rho_0 \exp[E_0/k_B T]$, the shaded areas mark a deviation from this insulating behaviour [92].

For best representation, the comparison in Fig. 6.1 is done between mesoscopic and macroscopic devices from different wafers, although with the same spacer width. However, a direct comparison between a macroscopic and a mesoscopic device from the same wafer showed qualitatively the same result. Also, because the localisation transition in mesoscopic devices occurs at much lower densities, the mesoscopic devices shown have much lower densities at the same resistivity. But again, a comparison at the same density with both devices in the localised regime (this is only possible over a very limited density range) confirmed the qualitatively different behaviour between macroscopic and mesoscopic 2DES.

6.2 Metallic and Saturated Behaviour

Let us start the discussion with the most striking behaviour of the temperature dependence, namely the case where the strongly insulating state at higher temperature turns into the opposite and becomes metallic. Figs. 6.2 and 6.3 show device A78d which exhibited a particularly strong metallic behaviour. In Fig. 6.2 the resistivity is shown as a function of inverse temperature $1/T$ at four different densities. At all densities, the systems shows an insulator-like activated transport at higher temperature, but a metallic behaviour appears below a crossover temperature T_θ, indicating a temperature-driven insulator-to-metal transition. This behaviour is observed over approximately three orders of magnitude of resistivity and up to $\rho \approx 800 \times h/e^2$. The reduction in resistivity between the temperature where ρ is maximum and base temperature is usually about 10 % with extreme values of 5 % and 20 %. As Fig. 6.3 shows, a non-monotonic T-dependence with a decrease in resistance at lowest T persists continuously over the entire accessible n_s-range in the localised regime.

This was not the case in all measured devices. In most cases, metallic behaviour occurred only at certain electron densities. The extent of metallicity varied from device to device but also between different cooldowns of the same device. However, more that 50 % of the mesoscopic devices with spacer width $20\,\text{nm} \leq \delta_{sp} \leq 60\,\text{nm}$ showed metallic behaviour at certain ranges of n_s. Please note that *all* these mesoscopic devices did show a low-T saturation where metallicity was absent. Examples of devices with $\delta_{sp} = 20 - 60\,\text{nm}$

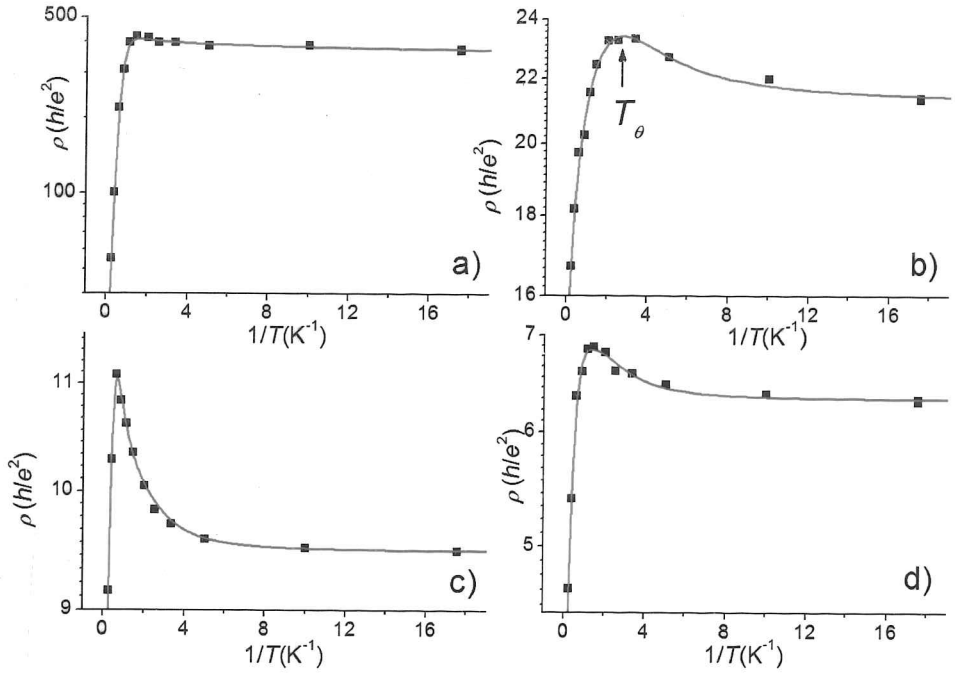

Figure 6.2: Resistivity as a function of inverse temperature at B=0 for device A78d at four different densities, which are indicated by arrows in Fig. 6.3. At all densities the strongly insulating (activated) temperature dependence at higher densities is followed by a decrease in resistance below a crossover temperature T_θ (indicated by arrow in b)). The solid lines are fits of Eq. (6.3) to the data.

showing metallic behaviour at low or zero magnetic field are given in Fig. 6.4. Characteristics are very similar to the data shown in Fig. 6.2, with all devices showing a strongly insulating regime it higher T before turning to metallic behaviour below a crossover temperature $T_\theta \approx 0.7 - 1.5\,\mathrm{K}$.

Fig. 6.5 shows an overview of the occurrence of metallic and saturated behaviour as a function of electron density for four different devices from three different wafers with spacer widths $\delta_{\mathrm{sp}} = 20-60\,\mathrm{nm}$. In order to distinguish be-

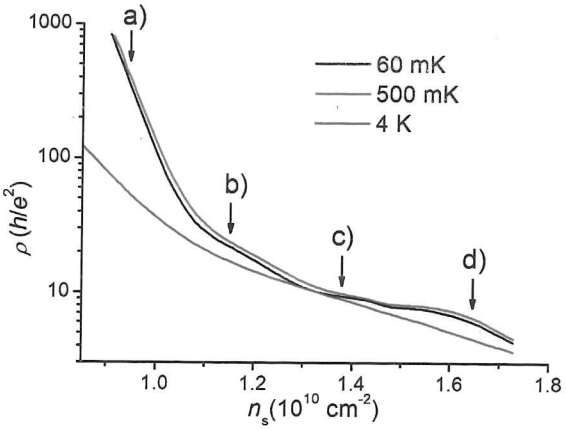

Figure 6.3: Resistivity as a function of electron density for device A78d at three different temperatures (B=0). The resistivity at $T = 500\,\mathrm{mK}$ is higher than at both $T = 4\,\mathrm{K}$ and $T = 60\,\mathrm{mK}$, implying a non-monotonic temperature dependence of resistance at all densities. The resistivity ranges from less than $10 \times h/e^2$ to almost $1000 \times h/e^2$, i.e. over approximately two orders of magnitude. The arrows indicate the positions in density of the respective panels in Fig. 6.2.

tween metallic and saturated low temperature behaviour, the slope $\frac{d\rho(T)/dT}{\rho(T)}$ was determined by linearly fitting the resistivity locally around $T \approx 400 - 500\,\mathrm{mK}$. A positive value (colour coded yellow to red) indicates a metallic behaviour, while a negative coefficient (blue) can be attributed to a saturated behaviour. The choice of $T \approx 400 - 500\,\mathrm{mK}$ as reference temperature is somewhat arbitrary, being the lowest temperature to give a reliable result in the ^{3}He system with a base temperature of $T_{\mathrm{Base}} \approx 300\,\mathrm{mK}$. However, it gives a good quantity to distinguish between metallic and saturated behaviour: Whenever metallicity was observed, $\frac{d\rho(T)/dT}{\rho(T)}$ was negative in this temperature range, since $T_\theta \gtrsim 500\,\mathrm{mK}$ in all cases and a turnaround from a metallic back to insulating behaviour at very lowest temperature never occurred. The quantity is mainly meant to discern the metallic and saturated behaviour rather the quantifying the "degree of metallicity".

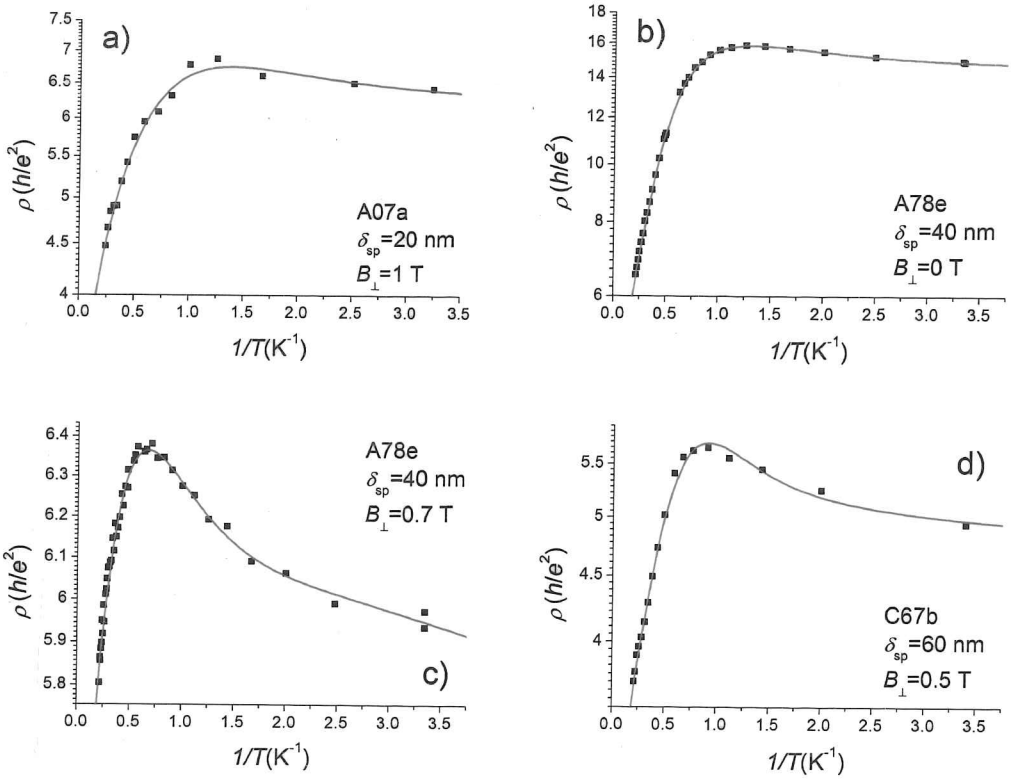

Figure 6.4: Metallic behaviour of three devices with $\delta_{sp} = 20 - 60$ nm, all at low or zero magnetic field. Characteristics are very similar in all cases, with a strongly insulating behaviour at high temperature and metallic behaviour below a crossover temperature $T_\theta \approx 0.7 - 1.5$ K. The solid lines are fits of (6.3) to the data. The extracted values of the temperature exponent γ are a) 1.66 b) 2.62 c) 1.83 d) 2.68, confirming the result that $\gamma \sim 2$ [92].

A good example of saturated behaviour with a very clear transition from activated to weakly temperature dependent regime is shown in Fig. 6.6. The transition temperature T^* cannot be defined as unambiguously as in the case of metallic behaviour, where T_θ is easily determined by the temperature of maximum resistivity. T^* can only be slightly vaguely defined as a temperature between fully activated and clearly saturated regime, which is usually a range

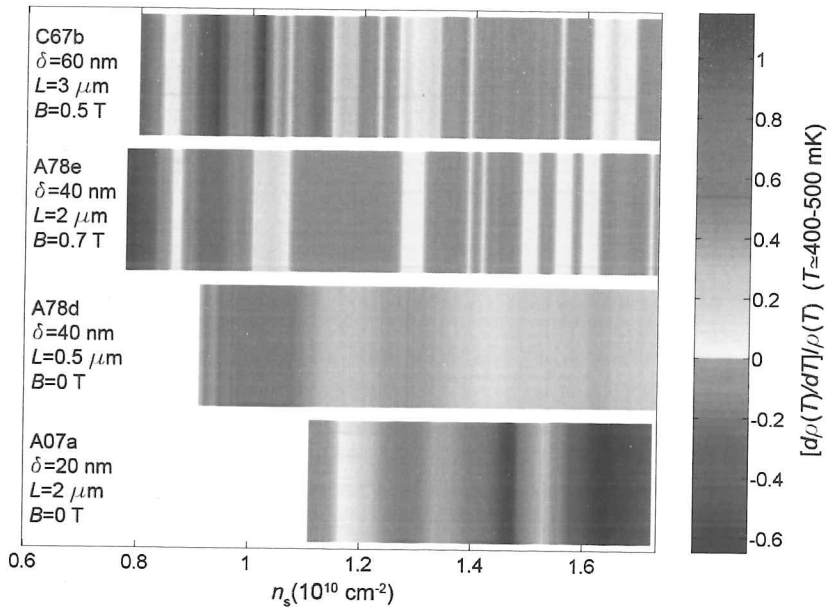

Figure 6.5: Comparison of "metallicity" (defined as $\frac{d\rho(T)/dT}{\rho(T)}$ at $T \approx 400-500\,\mathrm{mK}$) for four different devices from three different wafers with spacer widths $\delta_{\mathrm{sp}} = 20 - 60\,\mathrm{nm}$. A metallic state shows positive values while a negative value can be assigned to a saturated behaviour. The mesa width is $W = 8\,\mu\mathrm{m}$ for all devices, while the gate length L is indicated in the graph [92].

of a few hundred mK. However, one can say that T^*, like T_θ, always lies within the range $500\,\mathrm{mK} \lesssim T^* \lesssim 2\,\mathrm{K}$. In fact, T^* and T_θ seem strongly related. As Fig. 6.5 shows, transitions between metallic and saturated regime often occurred as a function of electron density. This changeover does not seem to happen through a shift of T_θ to a temperature below T_{Base} of the cryostat. Rather than that, at the transition density, the crossover temperature just seems to continuously change from T_θ to T^*.

While a strong perpendicular magnetic field seemed to slightly shift T^* towards lower temperatures (see Sect. 6.3), a clear trend of T^* with changing spacer width or device dimension could not be established from the available data.

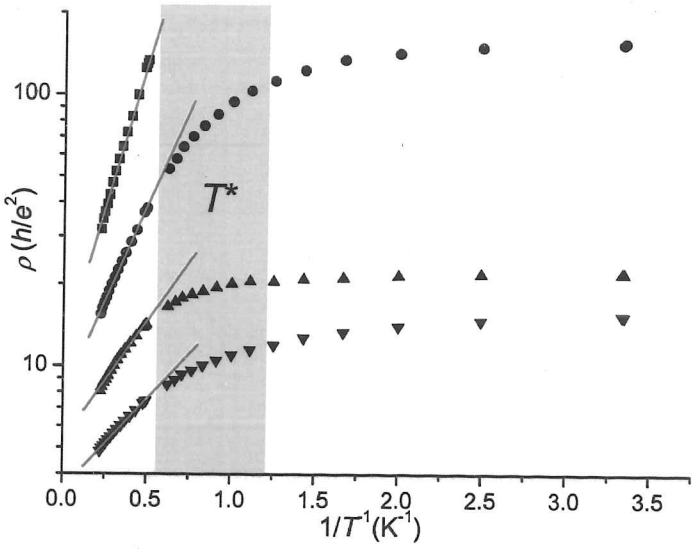

Figure 6.6: Activated (high T) and saturated (low T) behaviour for device A78e at B=0 T (n_s=0.61, 0.71, 0.83 and 0.95×10^{10} cm^{-2}, starting with highest resistivity). The solid lines are fits of the form $\rho(T) = \rho_b \exp(E_b/k_B T)$. The shaded area corresponds to the transition between the two regimes, i.e. the range of T^* [94].

6.2.1 Discussion

"Conventional" Metal-Insulator Transition

At this point, a brief discussion of the apparent metal-insulator transition (MIT) first reported by Kravchenko *et al.* [100] is appropriate (it is in the following referred to as "conventional" MIT). The observation, reported in Si-MOSFET's as well as GaAs/AlGaAs based 2D electron and hole gases, provoked a large amount of work of both experimental and theoretical nature [19]. Briefly summarised, the experimental observation was that in the interacting regime of 2DES, a crossover from an insulating temperature dependence at low densities to a metallic T-dependence at high densities occurred at a critical density (see Fig. 6.7). The transition occurred at a resistivity in the order of the quantum of resistance h/e^2 and the metallic behaviour persisted to the lowest accessible temperatures. The claims of this observation to be the signature of a metallic ground state in 2D have always been controversial. Recently,

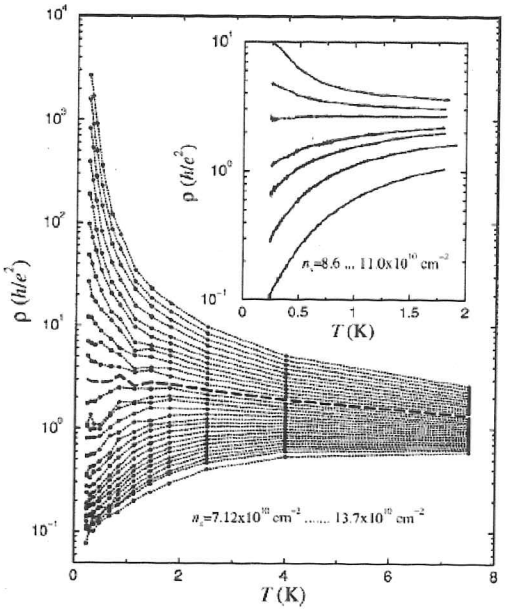

Figure 6.7: Apparent metal-insulator transition in a Si-MOSFET. [From Ref. [19]]

a change in the sign of $d\rho/dT$ was observed at ultra low temperatures in the putative metallic state [101], which strongly supports the notion that it is not a sign of a true metallic ground state.

The metallic behaviour reported in this thesis cannot be explained as a variation of the conventional MIT, as it is crucially different in several aspects: (1) The conventional MIT at zero magnetic field shows the metallic phase at higher electron densities but always crosses over to an insulating phase below a critical density, i.e. it is a density-driven metal-to-insulator transition. This is qualitatively different from the behaviour observed here, where in some cases a continuous metallic phase was seen down to the lowest electron densities, but in other cases a repeated transition between metallic and insulating (but saturated) behaviour occurred.
(2) Even though rather strong non-monotonic T-dependence (i.e. insulating at high T and metallic at low T) has been reported in context of the conventional MIT [102], this is not a common feature, and in most cases, the T-dependence was found to be either insulating or metallic over the whole temperature range

(see Fig. 6.7). By contrast, in the case presented here, the strongly insulating (activated) behaviour at higher temperatures is an intrinsic property of the observation and the insulator-to-metal transition appears to be temperature-driven. A temperature-driven transition from activated to metallic behaviour in two-dimensions in 2D has not been previously reported to my knowledge. (3) The conventional MIT occurs at a resistivity scale set by $\rho \sim h/e^2$ and the metallic phase is never observed above a resistivity of a few times h/e^2. This is in complete contrast to the metallic behaviour reported here, which was only observed at $\rho > h/e^2$ and persisted to resistivities as high as $\rho \approx 800 \times h/e^2$.

Many possible theoretical explanations have been proposed for the conventional MIT, such as renormalisation group calculations predicting a quantum critical point separating a metallic from an insulating phase in disordered interacting 2DES [103], a percolation transition in a network of quantum point contacts [104], or a temperature dependent screening of the scattering by impurities [105]. These theories are, of course, not aimed at explaining the observations described in this thesis, and in most cases cannot be applied these results, the main reason being that the theories do not apply to the strongly localised regime ($\rho \gg h/e^2$). Work done in relation to the conventional MIT that nevertheless may be of relevance to this thesis will be discussed later.

Quantum Diffusion of Defects in an Electron Solid

In Chapt. 5 it was shown that results of magnetoresistance measurements can be interpreted as evidence of an electron solid in which transport occurs by movement of charged defects such as vacancies or interstitials. Here, it is shown that this picture may provide a consistent explanation for the unusual temperature dependence of resistivity described above. The mechanism that may lead to a metallic temperature dependence is that of a delocalisation of defects in a quantum solid (QS).

The quantum behaviour of defects in a solid was first discussed by Andreev and Lifshitz (AL) for the case of atomic crystals [49]. They pointed out that quantum mechanics requires the existence of zero-point vibrations of the lattice, i.e. vibrations that remain at zero temperature and, therefore, do not violate the periodicity of the crystal. If these zero-point vibrations are large compared to the lattice constant a_0, quantum mechanical effects become

important, i.e. it is a quantum solid. A numerical measure of the relative magnitude of zero-point vibrations is given by the parameter

$$\Lambda = h/a_0\sqrt{m\epsilon}, \tag{6.1}$$

where m is the mass of an atom and ϵ the characteristic interaction energy between the atoms. This parameter is small for most crystals, but there are exceptions such as solid helium with $\Lambda > 1$.

Classically, defects such as vacancies, interstitials or impurities are localised. However, due to the finiteness of Λ and the degeneracy of the energies of defects under translation by a lattice constant, which lead to the possibility of quantum tunnelling, a delocalisation of the defects is possible. The finite time t a defect spends at a certain lattice site leads to a finite bandwidth W of the defect energy, which can be quantified as $W \sim \hbar/t$ according to the Heisenberg uncertainty principle. The bandwidth becomes important when the perfect periodicity of the crystal is disturbed by an external disorder potential: If the misalignment E_m between energies of adjacent defects is larger than the bandwidth, a coherent tunnelling between those states (i.e. tunnelling not involving absorption or emission of a phonon) is not possible anymore and delocalisation of the defects is suppressed. This is schematically shown in Fig. 6.8 a). Fig. 6.8 b) shows the situation where $W > E_\mathrm{m}$ and a delocalisation of defects is possible.

With increasing bandwidth, $W/2$ can, in principle, become larger than the defect energy E_d itself. This means that the band minimum ϵ_d becomes negative. One could imagine that this would lead to a melting of the crystal. However, AL conjectured that only a reorganisation of the crystal's ground state might occur. This new ground state must contain defects, but has to be perfectly periodic. Hence, AL proposed an incommensurate crystal where the number of crystal lattice sites is unequal to the number of atoms, or in other words, the defects are completely delocalised and form so called "defectons". According to AL this crystal possesses the property of quantum fluidity even at zero temperature, i.e. it can flow around obstacles and would not be pinned by a small amount of disorder. It is, therefore, sometimes referred to as supersolid.

AL also qualitatively discussed the temperature dependence of the movement of defects in a quantum solid. At very low temperature the defectons can

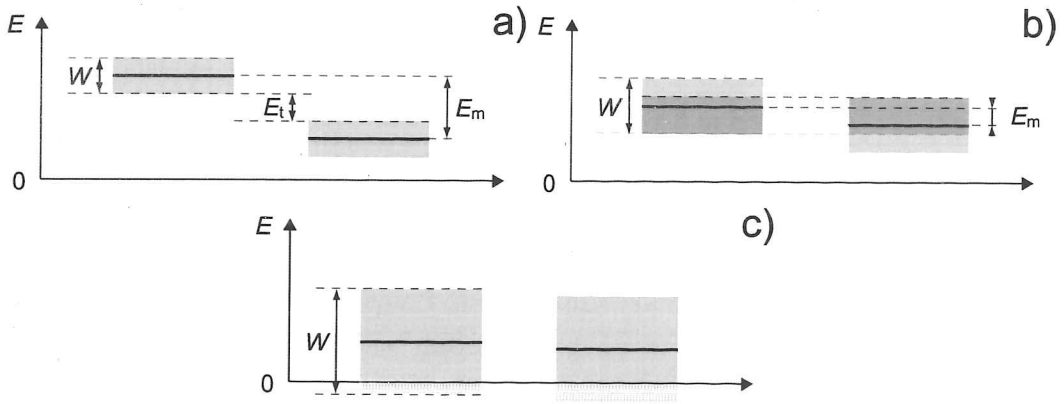

Figure 6.8: Schematic of defect energies and bandwidths in a quantum solid: a) The misalignment E_m between adjacent defect states is larger than the bandwidth W of the defect energies. Coherent tunnelling suppressed. b) The misalignment E_m between adjacent defect states is smaller than the bandwidth W of the defect energies. Coherent tunnelling is possible. c) The band minimum ϵ_d is negative and the crystal must either melt or become incommensurate.

move practically freely, only occasionally undergoing collisions with phonons, which reduce the mobility. For this regime, they predicted a temperature dependence of the diffusion coefficient $D \propto T^{-9}$. With increasing temperature, the defecton-phonon collision frequency increases and there comes a point when, during the time a defect spends on a fixed site, it is able to reach equilibrium with the lattice. Under such conditions, one must talk about a localised defect undergoing a random walk with a step equal to the lattice period a_0, a process which is practically temperature independent. With the temperature increasing even further, the probability of a defect being thermally excited across the energy barrier become larger, and eventually, this will be the dominant transport mechanism, leading to a classical activated transport.

A more quantitative theory for quantum diffusion of defects in quantum crystals such as solid helium was done by Pushkarov [106]. He predicted a temperature dependence of the diffusion coefficient D of the form

$$D = (D_0^{-1} + C_1 T^{\gamma})^{-1} + C_2 \exp(-E_0/k_B T). \tag{6.2}$$

Here, the second term comes from the classical activated diffusion. The first term consists of a temperature independent D_0 arising from impurity scattering and a power law temperature dependent part. The coefficient of the power law is predicted as $\gamma = 9$ in the case of strong defecton-phonon scattering, but $\gamma = 2$ if defecton-defecton collisions are the dominant scattering mechanism.

As discussed in Sect. 2.4.2, some theoretical work has been done on the possibility of delocalised defects in two-dimensional electron systems [47, 48]. A transport mechanism was not touched on in this work, not to speak of its temperature dependence. However, given that defects in an electron solid are charged quasi-particles which can carry a current, one can conclude that the atomic diffusion in Eq. (6.2) is analogous to the inverse resistance in an electronic QS. Hence, Eq. (6.2) can be rewritten as

$$\rho(T)^{-1} = (\rho_0 + \alpha T^{\gamma})^{-1} + \beta \exp(-E_0/k_{\mathrm{B}}T). \tag{6.3}$$

Indeed, this equation can be fitted very well to the data with metallic behaviour, as shown in Figs. 6.2 and 6.4. Fig. 6.4 shows fits to the data from three different devices (from different wafers, $\delta_{\mathrm{sp}} = 20 - 60\,\mathrm{nm}$) at the electron density where metallicity was strongest for each device. Fig. 6.2 shows four different densities of device A78d, which showed metallicity over the whole measured density range. The quality of the fits is excellent over the entire temperature range for all instances.

In Fig. 6.9, some of the parameters extracted from the fits for device A78d at various electron densities are shown. Panel a) shows the residual resistivity ρ_0 extrapolated to zero temperature. The value is finite, but $\rho_0 \gg h/e^2$. This is very unusual, since a finite ρ_0 is only expected for a metal, but for conventional metals $\rho_0 \lesssim h/e^2$ is generally observed. For an insulator ρ_0 is infinite.

The exponent γ of the power law temperature dependence is shown in Fig. 6.9 b). Over a wide range of densities $\gamma \sim 2$, a result confirmed by the fits for other devices shown in Fig. 6.4 with the extracted values of γ given in the figure caption. According to Ref. [106], this suggests inter-quasiparticle scattering as dominant relaxation mechanism. For the case of diffusion of impurities in solid He, $\gamma = 9$ was confirmed experimentally [106]. It is not entirely surprising that in an electronic solid, defecton-defecton scattering is stronger, since in this case the quasiparticles are charged. Also, in a Wigner

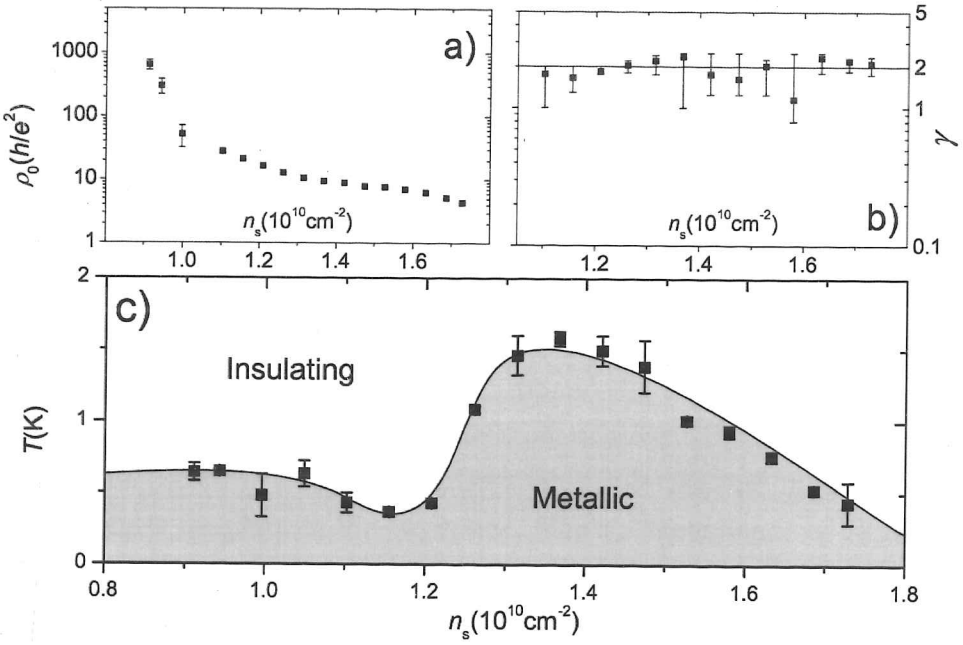

Figure 6.9: Physical quantities extracted from data fits to Eq. (6.3) for device A78d as shown in Fig. 6.2: a) ρ_0 represents the resistivity extrapolated to $T = 0$. While for an insulating state, ρ_0 is infinite, for a metal a finite $\rho_0 \lesssim h/e^2$ is usually observed. Here, surprisingly, $\rho_0 \gg h/e^2$ but finite for all n_s. b) The temperature exponent is found to be $\gamma \sim 2$ over a wide density range. c) Temperature T_θ at which the resistivity is maximal. It shows a non-monotonic density-dependence with a maximum value $T_\theta \approx 1.5\,\mathrm{K}$ at an intermediate density. T_θ marks the transition temperature between the insulating an the metallic phase, and, hence, defines a phase diagram in $T - n_s$ space.

crystal the pinning gap at low frequencies in the phonon spectrum (discussed in Sect. 2.5.1) may strongly suppress phonon scattering at lowest temperatures. The quantitative estimate for the pinning gap given by Eq. (2.6) reveals an energy scale >100 K for typical experimental parameters. This would suggest that the phonons in the electron solid are, indeed, frozen out. However, the value seems rather high and it is unclear if the calculations done for a classical Wigner crystal are valid for a quantum solid.

The strong deviations from $\gamma \sim 2$ at lowest electron densities may be explained by a stronger disorder scattering, which could mask the T^2-dependence. One should also keep in mind that at the very lowest electron densities, only a few hundred electrons are left in the active area of the device. The number of defects must naturally be even smaller than the number of electrons. This could lead to statistical deviations from the value expected for a very large number of particles.

The n_s-dependence of T_θ, the temperature where the resistance is maximum, is shown in Fig. 6.9 c). It shows a non-monotonic behaviour $T \approx 0.7 - 1.5\,\mathrm{K}$ with a maximum at intermediate electron density. Phenomenologically, T_θ indicates the crossover temperature between insulating and metallic state and defines a phase diagram in $T - n_s$ space. The n_s-dependence of T_θ is not well understood at present. As seen in Fig. 6.5, density driven transitions between metallic and saturated behaviour were often observed, which may be attributed to the interplay between electron density and disorder topology as discussed below. Similarly, the relative contributions of the activated and the T^2 part of conduction could vary with density due to disorder effects and the observed n_s-dependence of T_θ may be coincidental.

The activation energy for device A78d was found to be $E_0 \approx 1 - 6\,\mathrm{K}$ with a trend of decreasing E_0 with increasing n_s but rather strong scattering (not shown), which can be attributed to the lack of sufficient high temperature data points in this measurement. A more detailed discussion of the activation energies is given in Sect. 6.4.1.

We have now seen that quantum diffusion of defects can adequately describe the metallic behaviour, and also the transition to activated transport at higher temperatures. But how does the appearance of saturated T-dependence fit into this picture?

As discussed above, in a system with finite disorder a delocalisation of defects can only occur if the misalignment between defect energies is smaller than the defect bandwidth (Fig. 6.8 b)). In the opposite case (Fig. 6.8 a)), defects remain localised and transport can either occur by activation across the energy barrier E_b, or by incoherent tunnelling, where the energy difference E_t between the band edges is overcome by emission or absorption of a phonon. This is

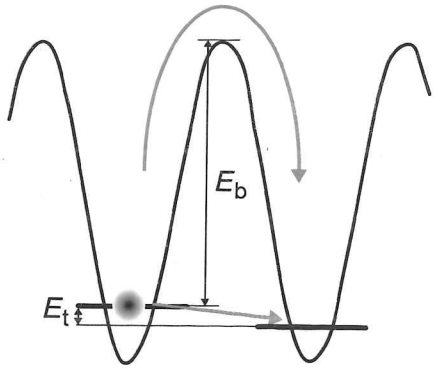

Figure 6.10: Schematic of two component transport with activation across the energy barrier (blue) and phonon assisted tunnelling (green).

shown schematically in Fig. 6.10 where the bandwidth has been neglected. In this situation, one can expect a two component form of resistivity

$$\rho(T)^{-1} = \rho_b^{-1} \exp(-E_b/k_B T) + \rho_t^{-1} \exp(-E_t/k_B T). \tag{6.4}$$

In our situation the difference between energy levels E_t is expected to be very small and, hence, $E_b \gg E_t$. If $\rho_b \ll \rho_t$, which is also a realistic assumption, the first term will dominate at high temperatures and the second one at low temperatures. Indeed, Eq. (6.4) can be fitted very well to the data of saturated behaviour as Fig. 6.11 shows for two devices at a few electron densities. These fits were done for several devices at various densities and several magnetic fields, and they all showed a similar agreement (not shown). The energy difference in the tunnelling process was usually very small (E_t/k_B <10 mK) and in almost all cases $E_t \ll k_B T_{Base}$. This explains the practically temperature independent behaviour of ρ at low T, but also the apparent absence of variable-range hopping (VRH) as suggested by result of hopping magnetoresistance (Chapt. 5). One would still expect a transition to VRH at $T \ll E_t/k_B$, however, such low temperatures are not experimentally accessible.

The duality between saturated and metallic behaviour can now be understood as follows: At any given electron density, the background disorder will most likely suppress the delocalisation of defects in certain areas. As n_s is changed, the electron lattice changes relative to the disorder and metallic regions can become non-metallic or vice versa. If a significant part of the device

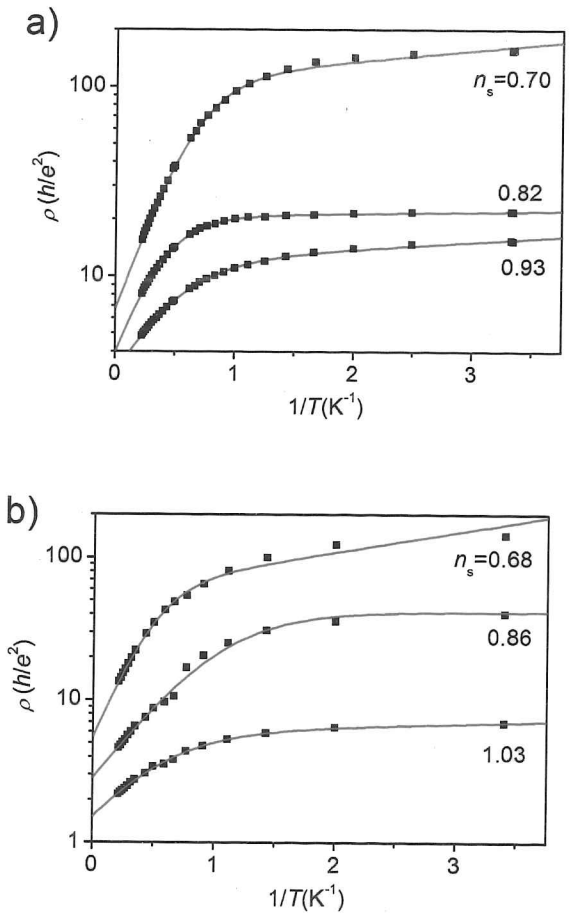

Figure 6.11: Fits of Eq. (6.4) to data with saturated behaviour at $B = 0$, showing a very good agreement. Similar agreement was observed in all cases were fits were done. Devices: a) A78e, b) C67b. Electron densities are indicated in units of $10^{10}\,\mathrm{cm}^{-2}$ [92].

is metallic and, in particular, a connection from source to drain exists, metallic temperature dependence is observed. On the other hand, if the device is mostly non-metallic, a saturated behaviour will persist. With this in mind, it is not surprising that the shortest device showed a continuous metallic behaviour, as it is most likely that a metallic path is formed across the device in this case. However, one cannot exclude this correlation to be a coincidence and more

devices of various sizes would have to be measured to draw any conclusions in this direction.

Finally, one has to consider if the formation of such a quantum solid in the systems used here is realistic at all. As discussed in Sect. 2.5, the theoretical treatment of 2DES in the strongly interacting regime in presence of disorder is extremely difficult. However, it is generally agreed that disorder can enhance interaction effects. In particular, the formation of a Wigner crystal at r_s as low as 7.5 has been predicted in presence of disorder [20] as compared to $r_s \approx 37$ in the pure case [12]. A variation of the disorder parameters may well lead to a further reduction of r_s where Wigner crystallisation is possible. Therefore, an electron solid formation in the density region where experiments were carried out for this thesis ($r_s \approx 4-6$) does not seem too far fetched.

On the other hand, it can easily be shown that the magnitude of zero-point fluctuations relative to the lattice constant expressed by the parameter Λ as defined in Eq. (6.1) is $\Lambda \approx 2\sqrt{\pi/r_s}$ for a WC, using the effective mass m^* in GaAs and the Coulomb energy between electrons separated by $r_{ee} \approx 1/\sqrt{n_s}$ for ϵ. For $r_s \approx 4-6$, $\Lambda \approx 1.4-1.8$, while for $r_s > 37$, where a WC might be formed in a very clean system, $\Lambda \lesssim 0.6$. This could explain why a quantum diffusion is more likely to be observed in the approach used here than in other attempts of WC investigation where a minimisation of disorder and maximisation of r_s is generally pursued. Another factor is the size: Even if metallic regions were formed, it is much less likely that they percolate from source to drain in a macroscopic device than in a mesoscopic one.

The origin of the defects could be manifold. In a situation where the defect band minimum is negative (schematic in Fig. 6.8 c), the zero-point defects are an intrinsic property of the 2DES ground state. However, even if this condition is not fulfilled, defects may be created thermally, through disorder, or when the gate is swept and electrons have to rearrange as the density changes. These defects could, nevertheless, delocalise if the bandwidth is large enough (situation as in Fig. 6.8 b). In fact, recent experiments in solid ^{4}He show that the signatures of a possible supersolid phase in these systems are strongly enhanced when the helium is cooled extremely fast, which leads to a strongly disordered, glassy solid [107, 108]. This may be another reason why such a

phase is more likely to be observed in the systems used here, but not in ultra clean 2DES.

An exciting question is whether defects, be they created spontaneously or by an external influence, really remain delocalised at arbitrarily low temperatures. This would mean that, if our interpretation was correct, a truly metallic phase in 2D exists, in contradiction to the scaling theory of localisation [4]. The finite disorder could eventually lead to an Anderson localisation of all defects [109], but it is by no means obvious that this has to be the case [110].

Tunnelling Between Disorder Induced Electron Puddles

As discussed in the context of magnetoresistance in Sect. 5.5, Tripathi and Kennett (TK, Refs. [97, 99]) have developed a theory based on electron puddle formation to explain several aspects of the results presented in this thesis. In their picture, transport occurs by tunnelling of electrons between those puddles, which are formed due to disorder in the non-linear screening regime at low electron densities. If these puddles are small enough, and the tunnelling probability is small, Coulomb blockade effects should become important. The primary impetus for putting this effect forward comes from the resistance oscillations described in Chapt. 7, which have been associated with Coulomb blockade oscillations by TK. This will be discussed in detail in the respective chapter.

TK have discussed the temperature dependence of resistance in the regime where Coulomb blockade effects are important. They predicted a resistance of the form

$$R(T)^{-1} = G_0/\cosh^2(E_0/2k_BT) + G_{\mathrm{cot}}(1 + cT + aT^2). \qquad (6.5)$$

Here, the exponential term comes from the energy difference E_0 between the Fermi energy in the leads and the lowest available energy state in the dot, determined by the level spacing and charging energy. E_0 oscillates as a function of gate voltage between zero at resonance and some maximum value. G_0 depends on the symmetry of the tunnelling barriers and has a maximum value of e^2/h. The second term is a phenomenological expression arising from resonant cotunnelling (a and c are non-negative parameters), i.e. an event where one

electron tunnels out of the puddle but is simultaneously replaced by another electron tunnelling in. This process is of second order in the small tunnelling probability. It is expected to be small and important only at very low temperatures. In the case of transport through a string of puddles, the situation conjectured for mesoscopic systems by TK, the total cotunnelling probability is the product of the probability for each individual puddle, and is even smaller.

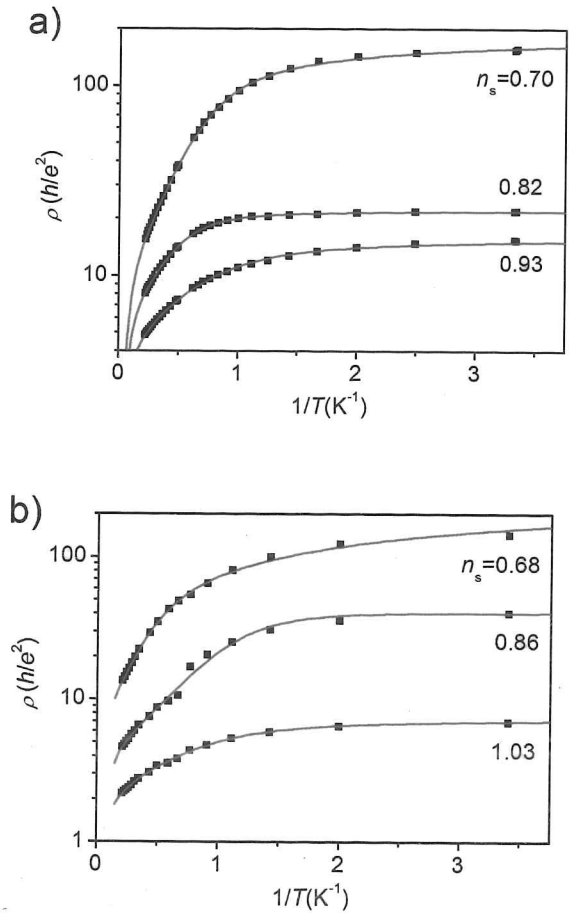

Figure 6.12: Fits of Eq. (6.5) to data with saturated behaviour at $B = 0$, showing equally good agreement as Eq. (6.4) presented in Fig. 6.11. Similar agreement was observed in all cases were fits were done. Devices: a) A78e, b) C67b. Electron densities are indicated in units of 10^{10} cm^{-2} in the legends [92].

Fig. 6.12 shows the same data as Fig. 6.11, but this time fits were done with Eq. (6.5), showing equally good results. Similar agreement was observed in all cases were fits were done (not shown). The successful fitting of two rather different expressions suggests that the good agreement might be fortuitous in either case. The condition $G_0 \lesssim e^2/h$ is fulfilled in all cases and $G_{\mathrm{cot}} \ll G_0$ generally, even though in some cases $G_{\mathrm{cot}} \approx G_0$. TK do not give any numerical value for the weight of the cotunnelling conduction compared to the thermally assisted tunnelling other than stating that the cotunnelling term is expected to be important only at very low temperatures. It seems therefore somewhat surprising that the cotunnelling term should become significant at temperatures as high as 1 K in experiments carried out for this thesis.

However, the main problem in TK's theory is that in cannot explain the metallic low-temperature behaviour. Eq. (6.5) cannot lead to a positive temperature coefficient of resistance $dR/dT > 0$. In the Coulomb blockade regime an insulating behaviour with diverging resistance as $T \to 0$ always occurs. A decreasing resistance with decreasing temperature is only possible in the regime of resonant tunnelling, due to the diminishing thermal broadening of the resonance [111]. However, this could only lead to metallic behaviour in a narrow region around resonance. Therefore, it cannot possibly explain the occurrence of a metallic phase over a large range of gate voltage/electron density as observed in device A78d (Fig. 6.3). These considerations exclude a resonance effect in one or several quantum dots as origin of the metallic temperature dependence.

Other Possible Scenarios

One possible explanation for a metallic temperature dependence has been proposed by Spivak *et al.* [51, 52] on the basis of the Pomeranchuk effect for a state of coexistence between Fermi liquid and Wigner crystal as discussed in Sect. 2.4.2. The spin entropy of the WC is larger than the entropy of the liquid. Therefore, the fraction of WC grows with increasing temperature. Since the resistivity of the WC is much larger than that of the liquid, the resistance of the system must increase with increasing temperature. If the temperature gets higher than the melting temperature of the WC, the process is reversed and with a further increase in temperature, the resistance should decrease again.

This qualitatively agrees with the experimental observation. The effect should be suppressed by a magnetic field strong enough to polarise the spins, as observed experimentally (see. Sect. 6.3). However, there are several points that speak against this scenario. First of all, due to the existence of the liquid phase, the overall resistivity would be expected to be rather low, in the order of h/e^2 and certainly not several hundred times h/e^2. Also, hopping transport and the observation that $r_{\mathrm{hop}} \approx r_{\mathrm{ee}}$, is not expected in this picture. Finally, the proposed phase coexistence should only occur in a very narrow range of n_{s} around the critical density [55] and can, hence, not explain the experimental observation of continuous or re-entrant metallicity over a large range of n_{s}.

Some attempts have been made to investigate if Coulomb interactions between electrons could, at least to some amount, overcome the localisation arising from disorder. For reviews see Refs. [40] and [19]. Two cases may be particularly relevant to the work described in this chapter and will be discussed in some more detail in the next two paragraphs.

Shepelyansky suggested that a pair of interacting (repulsive or attractive) particles can propagate coherently on a distance much larger than the one-particle localisation length in a random potential [112]. Details of transport or its temperature dependence are not given in those works. However, one could imagine that a pair or more complex many-body state is formed only below a certain critical temperature, much like in the case of Cooper-pairs in a superconductor. This could possibly lead to a sudden delocalisation and increase in conduction below this temperature as experimentally observed, with the critical temperature the experimentally observed T_θ. At present, this is only a conjecture and more theoretical work would be required to clarify if such a mechanism could, indeed, lead to the observed temperature dependence of resistance.

Basko *et al.* have recently studied the question if electron-electron interactions could lead to hopping conductance in absence of any phonon-electron interactions and if so, whether such a transport mechanism could lead to a finite conductivity at T=0 [109]. They concluded that many body effects could lead to a "metallic" phase where conduction is finite even in the absence of electron-phonon interactions. However, such a phase only exists above a critical temperature T_{c}, below which the conductivity is strictly zero without

electron-phonon interactions. This is, of course, exactly the opposite temperature dependence of conductivity than observed in the experiments, especially since even for the "metallic" phase, a decrease of conductance with decreasing temperature is predicted. Nevertheless, the work is of interest to the observed results as it considers a different transport mechanism from the standard hopping transport in the localised regime. Similar to the scenario described in the last paragraph, it may be the case that at high enough temperatures ($T > T_\theta$), strong phonon effects start dominating over the many-body hopping. This could lead to a single-particle transport at high temperature, crossing over to a - possibly metallic - many-body transport at low T.

More generally, for many of the phases discussed in Sects. 2.5 and 2.4, possible transport mechanisms have not been studied and a behaviour as reported in this chapter can neither be predicted nor ruled out.

6.3 Perpendicular Magnetic Field

6.3.1 Overview

Application of a magnetic field perpendicular to the plane of the 2DES has a dramatic effect on the metallic behaviour: At large enough $B_\perp$, the metallicity is completely suppressed. While low fields $B_\perp \lesssim 1\,\mathrm{T}$ have relatively little effect or in some cases even strengthen the metallicity, a clear metallic behaviour was never observed at $B_\perp \gtrsim 1.5\,\mathrm{T}$. Enough low field data is not available for a definite statement, but it should be noted that suppression of metallic behaviour seems to start in approximately the same range of $B_\perp$ where the low field negative magnetoresistance turns into exponential positive MR (see Sect. 5.4.1).

The suppression of metallicity can best be demonstrated with device A78d where the whole localised regime with resistivity $\rho \approx 3 - 800 \times h/e^2$ (corresponding to $n_\mathrm{s} = 0.9 - 1.7 \times 10^{10}\,\mathrm{cm}^{-2}$) showed strong metallic behaviour at $B_\perp = 0$. When a field $B_\perp = 1.5\,\mathrm{T}$ was applied, the same range of resistivity ($n_\mathrm{s} = 1.3 - 2.6 \times 10^{10}\,\mathrm{cm}^{-2}$) showed no metallic behaviour, whatsoever, but a strong saturation still occurred at lowest temperatures. An example of this is shown in Fig. 6.13. For the electron density $n_\mathrm{s} \cong 1.63 \times 10^{10}\,\mathrm{cm}^{-2}$, the

temperature dependence of resistivity is compared between $B_\perp = 0$ (inset) and $B_\perp = 1.5\,\mathrm{T}$ (red). Because of the exponential rise of ρ with $B_\perp^2$, the resistivity at $B_\perp = 1.5\,\mathrm{T}$ is much larger than at zero field. Therefore, one could argue that the qualitatively different behaviour simply arises from comparing two different regimes of resistivity/localisation. However, this argument can easily be refuted by comparing two measurements with approximately the same resistivity at T_{Base}. This is also shown Fig. 6.13, comparing two sets of data with $\rho(T_{\mathrm{Base}}) \approx 200 \times h/e^2$ at $B_\perp = 0$ (blue) and $B_\perp = 1.5\,\mathrm{T}$ (red). Naturally, in this comparison, the electron density at $B_\perp = 1.5\,\mathrm{T}$ is higher ($n_{\mathrm{s}} \cong 1.63 \times 10^{10}\,\mathrm{cm}^{-2}$) than at zero field ($n_{\mathrm{s}} \cong 0.98 \times 10^{10}\,\mathrm{cm}^{-2}$).

The development under magnetic field is rather difficult to analyse quantitatively or even qualitatively. First of all, it is difficult to quantify the "strength" of saturation. One way of quantification would be through the fitting of Eq. (6.4). One could use the low temperature activation energy E_{t} as a measure i.e. assign the smallest E_{t} to strongest saturation. However, the error in E_{t} is large because the temperature range of saturated behaviour is relatively small and even more so the resistivity range, which is natural as the resistivity changes weakly. Therefore, the best quantitative statement one can make about E_{t} is that it is generally a few tens of mK, with the distribution within this range appearing more or less random. Another way of quantifying the behaviour of saturation would be through the temperature T^* where the transition between activated and saturated behaviour occurs. However, as mentioned above (Sect. 6.2), this does not give a well defined temperature, but a temperature range. Because of this limitation, only a qualitative discussion seems reasonably possible. Fig. 6.14 shows the temperature dependence of two devices at $B_\perp$=0, 1.5, and 3 T where n_{s} has been chosen so that $\rho(T_{\mathrm{Base}}) \approx 200 \times h/e^2$ at all fields. It seems quite clear that the saturation transition loses its sharpness with increasing magnetic field and the total change in resistivity between $T_{\mathrm{Base}} \cong 300\,\mathrm{mK}$ and $T_{\mathrm{Max}} \cong 4.6\,\mathrm{K}$ gets larger at higher fields. Nevertheless, a sub-exponential dependence of ρ on $1/T$ remains at lowest T. In fact, as Fig. 6.15 shows, the qualitative behaviour of activated behaviour at high temperature and saturation at low T persists to fields as high as 8 T.

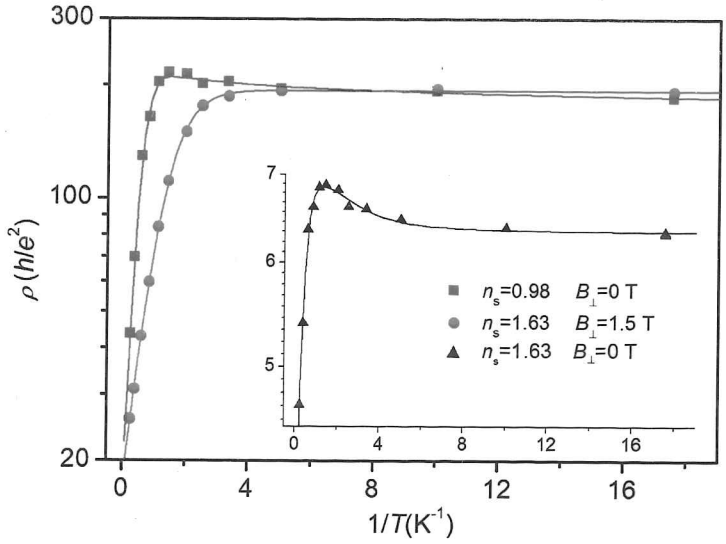

Figure 6.13: Comparison of temperature dependence at zero and finite perpendicular magnetic field $B_\perp$ for device A78d: The red data is at $n_s \cong 1.63 \times 10^{10}\,\mathrm{cm}^{-2}$ and $B_\perp = 1.5\,\mathrm{T}$. The inset shows the same n_s at zero field. The blue data is also at $B_\perp = 0$, but, here, a density has been chosen where $\rho(T_{\mathrm{Base}})$ is approximately the same as for the red data. The zero field data shows strong metallicity in both cases, while metallicity is completely suppressed at finite magnetic field but a clear saturation remains. The solid lines are fits of Eq. (6.3) for metallic and Eq. (6.4) for saturated behaviour, respectively.

6.3.2 Discussion

The suppression of the metallic behaviour can be readily explained in the picture of quantum diffusion in an electron solid. First of all, the perpendicular magnetic field reduces the wave function overlap between different states resulting in a suppression of the tunnelling probability. Since the bandwidth of the defect energy is inverse proportional to the tunnelling time, the bandwidth is expected to be reduced by a strong $B_\perp$. Hence, application of a strong per-

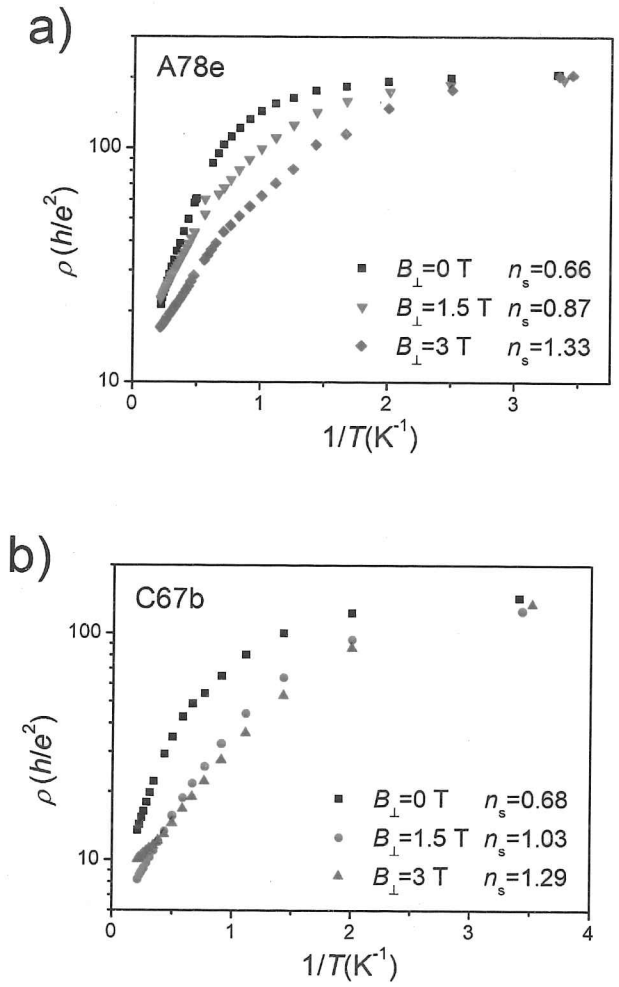

Figure 6.14: Comparison of data with $\rho(T_{\text{Base}}) \approx 200 \times h/e^2$ at $B_\perp$=0, 1.5 and 3 T for two different devices. The saturation appears to get weaker with increasing field, but a clear sub-exponential dependence of ρ on $1/T$ remains. Densities in the legend are given in units of $10^{10}\,\text{cm}^{-2}$ [92].

pendicular magnetic field can easily drive the system from a situation with an overlap of defect energies (schematic Figs. 6.8 b) and c)) to one where the bandwidth is too small to overcome the disorder induced difference in adjacent defect energies (Fig. 6.8a)). This would lead to the observed transition from metallic transport to weakly temperature dependent non-coherent tunnelling

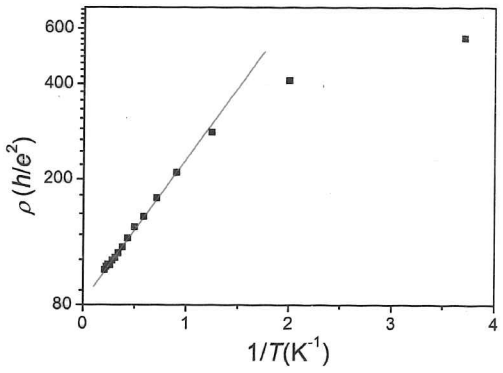

Figure 6.15: Activated and saturated behaviour for device A78d at $B_\perp$=8 T.

transport.

More generally, a perpendicular magnetic field is well known to confine charged particles within a length scale $l_B = \sqrt{\hbar/eB_\perp}$ (the magnetic length). For $B_\perp$=1.5 T, $l_B \approx 20$ nm, which means $l_B \lesssim r_{ee}$ for $B_\perp > 1.5$ T and it is not surprising that a delocalisation over a distance $> l_B$ cannot occur. The magnetic confinement cannot only explain the suppression of defect delocalisation in the framework of quantum diffusion, but of any kind of low temperature delocalisation mechanism.

6.4 Activation Energies

The discussion of the temperature dependence so far has been focused on the low temperature range. This section looks at the high temperature part where a strongly insulating T-dependence was always observed.

A behaviour

$$\rho(T) = \rho_0 \exp([E_0/k_B T]^p) \tag{6.6}$$

with p=1, 1/2, or 1/3 is a reasonable assumption, as this is the expected behaviour for transport in the strongly localised regime of 2DES (see Sect. 2.6). From this relation one can extract information about the activation energies involved. However, one should first check if the temperature dependence really is exponential. For this purpose, the resistivity as a function of $1/T$ is

compared with a linear and a logarithmic ρ-axis in Fig. 6.16. The linear fit on the logarithmic scale clearly confirms the exponential dependence on $1/T$. On the linear scale, a linear fit in not possible. Other possible relations such as a power law dependence or linear or exponential T dependence (rather than $1/T$) where also investigated but did not lead to a satisfactory result.

An absolutely unequivocal confirmation of the exponential dependence on $1/T$ is hindered by the fact that, due to the saturation at low T, the temperature and resistivity range in which the strongly insulating behaviour is observed, is limited. For definite confirmation of an exponential law, one would ideally be able to fit over several orders of magnitude in resistivity, which is not possible in our case. For the same reason, it is difficult to definitely determine the exact exponential behaviour, i.e. the coefficient p in Eq. (6.6). Determining p=1, 1/2, or 1/3, would distinguish between nearest-neighbour, Efros-Shklovskii, and Mott hopping. While the nearest-neighbour hopping (NNH) expression seems to agree best, the Efros-Shklovskii or Mott hopping relation fits are only marginally worse.

From available results, one can conclude that a simple activated behaviour, hinting at NNH, is the most likely mechanism, but VRH cannot be entirely ruled out in this regime. With increasing electron density (decreasing resistivity), the resistivity range often became so small that even a distinction between exponential or sub-exponential dependence on $1/T$ became difficult. However, no signs of a qualitative change in the high-T range was observed and an exponential behaviour was assumed to persist.

Activation energies were determined by fitting the expression (6.6) with $p = 1$ to the high temperature part of the data, as shown in Figs. 6.6 and 6.16 b). This approach was preferred over fitting more complicated expressions because it is the most general one and does not assume any specific model. Eqs. (6.4) and (6.5) both have an activated high T behaviour and fits of those expressions revealed similar activation energies.

Unfortunately, the generality of the expression has a drawback, namely that it does not retrieve much information about the origin of the activation energy. For example, in the picture of transport through defects in an electron solid, E_0 could be identified with the height of the energy barrier between defect states as well as the difference between defect energies. This is shown schematically

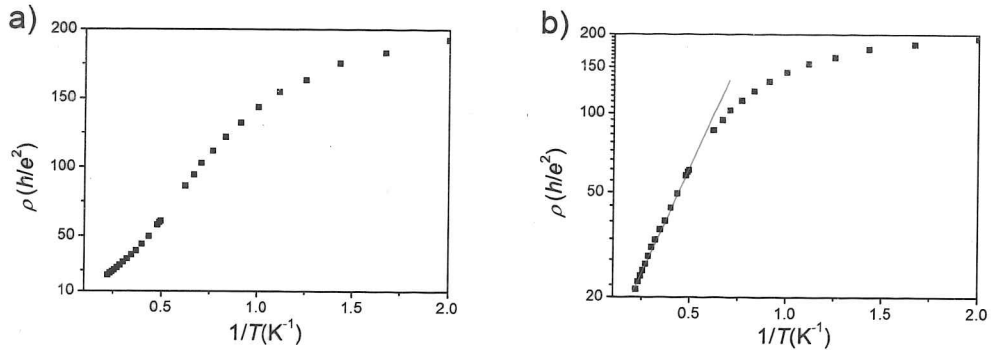

Figure 6.16: Comparison of temperature dependence of resistivity between linear a) and logarithmic b) y-axis. The x-axis is $1/T$ in both cases. An exponential dependence of ρ on $1/T$ is confirmed by the linear fit (solid line) in b). Device A78e, $B = 0$ [94].

in Fig. 6.10. For both transport mechanisms, a simple activated behaviour is expected, with E_0 identifiable with E_b or E_t, respectively. Additionally, the thermal creation of defects could play a role, where creation of charge carriers could again lead to an activated behaviour of resistivity, but here with the activation energy $E_0 = E_\mathrm{d}$, the energy required to create a defect. The situation where electrons are localised at disorder traps as single electron or electron puddles, is essentially the same, except that the defect creation process is absent. E_0 could be the height of the energy barrier between impurity states (essentially, activation to the mobility edge), as well as the average energy separation between nearest neighbour trap sites. Again, in both cases, a simple activated transport law is expected as long as the temperature is high enough to avoid VRH.

Figs. 6.17 a) and b) show the dependence of the activation energies E_0 on both electron density and perpendicular magnetic field for two devices with δ_sp=40 and 60 nm, respectively. Two clear trends can be spotted immediately: Firstly, E_0 decreases with increasing n_s, mostly monotonically. Secondly, while E_0 decreases at most densities for a low $B_\perp \lesssim 1\,\mathrm{T}$, it increases significantly as a stronger $B_\perp$ is applied.

A discussion of the n_s- and $B_\perp$-dependence of the activation energies is difficult because, as shown above, there are many different mechanism that might show an activated behaviour. On one hand, each of these mechanisms might show a different reaction when the electron densities or the magnetic field are changed. On the other hand, completely different scenarios could lead to a similar behaviour. In the following sections, an attempt is made to discuss which of the physical scenarios could lead to the experimentally observed behaviour when n_s and $B_\perp$ are varied.

6.4.1 Electron Density Dependence of E_0

Single-Particle Localised 2DES

In single-particle disorder localised 2DES, the qualitative behaviour E_0 can be explained if it is the activation energy required for the electron to escape the trap site, i.e. $E_0 = E_b$. At higher electron density, trap sites with smaller binding energy will be filled and, hence, the energy required to excite them will be smaller. If the density of states is a constant function of energy, one would expect E_0 to decrease linearly with n_s. The n_s-dependence of E_0 in Fig. 6.17 appears to be stronger than linear, hinting at a decreasing density of states with decreasing energy, which is, indeed, expected in the band tail. A decreasing density of states would also lead to an increase of E_t with decreasing n_s, since this means, by definition, that the energy separation between neighbouring states gets larger. Hence, the qualitative behaviour of E_0 can be well explained in a single-particle localisation picture, however, as discussed in other places, there are several other experimental results that are not compatible with this model.

Electron Puddles

In the case of hopping between puddles as put forward by TK, one would expect E_0 to oscillate between zero and a few Kelvin due to Coulomb blockade, with the effect becoming more pronounced with increasing magnetic field [99]. This is clearly not observed, a fact that will be discussed further in Chapt. 7.

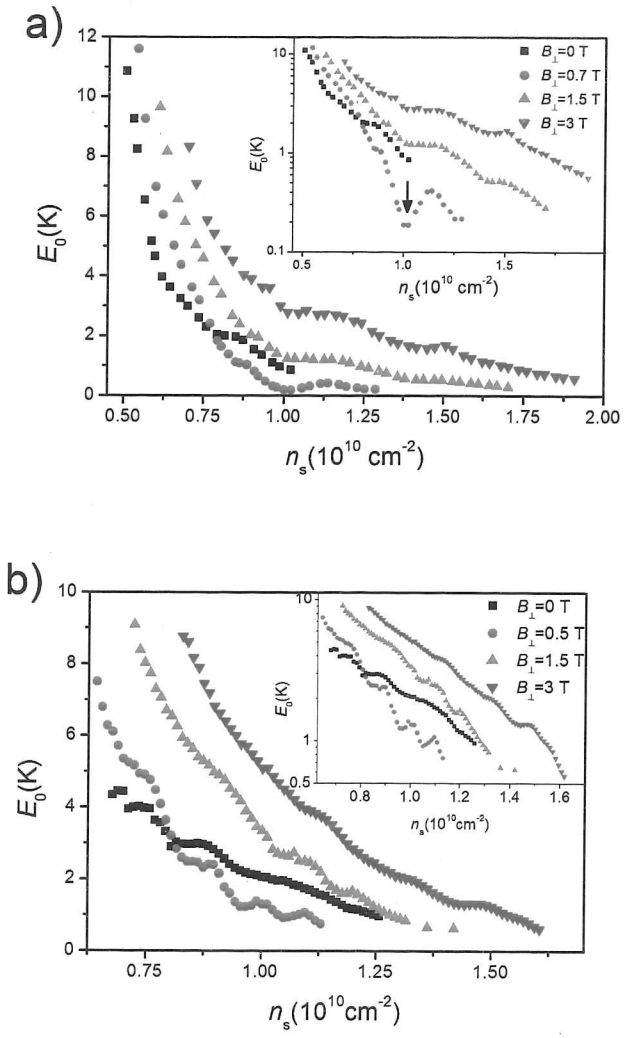

Figure 6.17: Activation energies at various perpendicular magnetic fields extracted from exponential fits to the high temperature range as shown in Fig. 6.6. Inset: Same data but with a logarithmic y-axis. Devices: a) A78e, b) C67b [92].

However, if Coulomb blockade is ignored, the qualitative behaviour on E_0 can be explained. For the situation $E_0 = E_\mathrm{b}$, the barrier height is expected to increase with decreasing n_s, which decreases the energy of the highest occupied level in the puddle relative to the barrier height. If $E_0 = E_\mathrm{t}$ one can expect

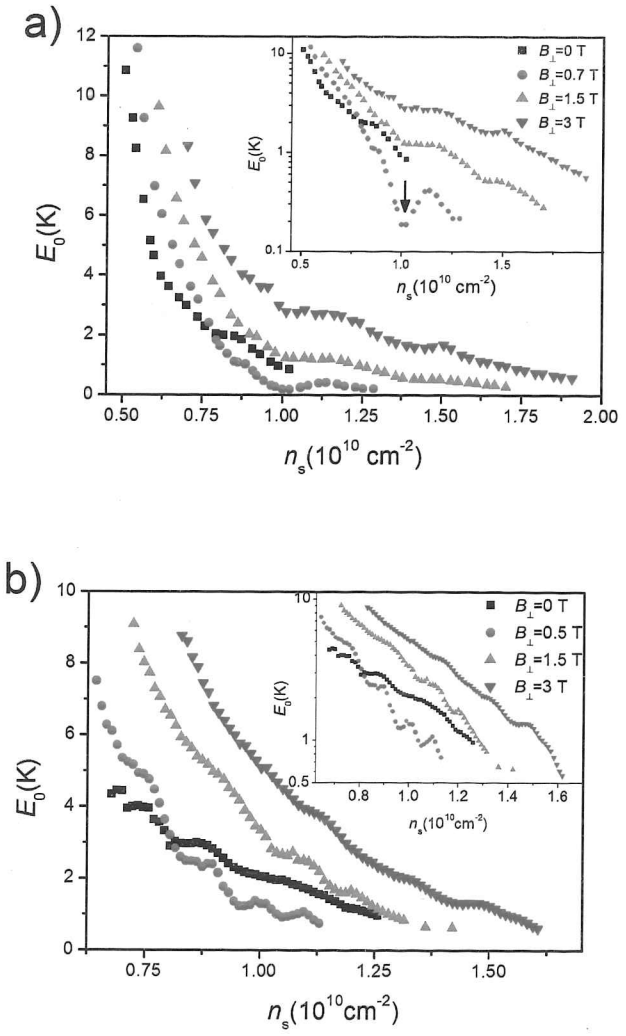

Figure 6.17: Activation energies at various perpendicular magnetic fields extracted from exponential fits to the high temperature range as shown in Fig. 6.6. Inset: Same data but with a logarithmic y-axis. Devices: a) A78e, b) C67b [92].

However, if Coulomb blockade is ignored, the qualitative behaviour on E_0 can be explained. For the situation $E_0 = E_\mathrm{b}$, the barrier height is expected to increase with decreasing n_s, which decreases the energy of the highest occupied level in the puddle relative to the barrier height. If $E_0 = E_\mathrm{t}$ one can expect

a better disorder screening at higher n_s to reduce the confinement and, hence, level separation in the puddles. This effectively increases the density of states at the Fermi energy, thereby reducing E_t.

Defects in an Electron Solid

The situation of defect transport in a electron solid is very difficult to discuss even qualitatively. For $E_0 = E_d$, i.e. the case of thermal creation of defects, a calculation has been done by Cockayne and Elser [113]. They proposed the energy of a point defect in a Wigner crystal to be $E_d = C_C/r_s + C_{zpv}/r_s^{3/2} + O[1/r_s^2]$ with the first term the change in Coulomb energy and the second term the change of zero-point vibrational energy. C_C is positive and C_{zpv} is negative, which means that E_d decreases with increasing electron density at large enough n_s, as observed. These calculation ignored disorder and are only of limited validity.

For $E_0 = E_t$, the density of defect states in space is proportional to n_s. Assuming a random scattering in the energy of the defect states, the density of states in energy will change in the same fashion as in space. This could explain the observed trend. However, if the activated part at high temperature was, indeed, arising from phonon assisted tunnelling between nearest neighbours, rather than activation across the barrier, the low temperature behaviour with saturation or metallicity could not be explained anymore, which was the main reason for introducing the picture of defect transport in an electron solid in the first place.

Unfortunately, the case which is considered most likely, namely $E_0 = E_b$ is the most difficult to discuss and no literature is available about the height of the energy barrier between defect states compared to their energy. The situation is fundamentally different from the case of simple localisation in potential minima arising from disorder, since, here, the traps are arising from the electrons themselves and change with electron density. The probable presence of strong quantum mechanical effects and the additional influence of the external disorder potential may lead to a complex behaviour of E_b on which the author would not like to speculate. In conclusion, the observed n_s-dependence of E_0 can neither support, nor refute the proposed transport mechanism of quantum diffusion in an electron solid.

Plateaux and Dips

A close look at Fig. 6.17 reveals a formation of plateaux or even dips in E_0 as function of n_s. This will be discussed in more details in Chapt. 7, in particular the plateaux. Nevertheless, a remark on the dips should be made here. The dips, clearest visible on the logarithmic scale in the insets, only occur at low magnetic fields and they always coincide with pockets of metallic behaviour. While this could have a physical origin, it is most likely an artefact, arising from a strong metallic transport component even in the insulating range. This would effectively lower the slope of the "exponential" part and reduce E_0. Indeed, for the strong minimum marked by an arrow in the inset to Fig. 6.17 a), if Eq. (6.3) is used to fit the data, the activation energy never falls below $E_0 \approx 0.8\,\mathrm{K}$.

6.4.2 B-Field Dependence of E_0

It is illustrative to have a look at the influence of a perpendicular magnetic field in a disorder free 2DES. The magnetic confinement can be expressed as an effective parabolic potential [81]

$$V_B = \frac{1}{2m^*}\left(\frac{eB_\perp r}{2}\right)^2, \tag{6.7}$$

where r is the distance in the plane of the 2DES. This means that an electron travelling over distance r_{hop} must overcome a magnetic barrier that increases quadratically with r_{hop} and $B_\perp$. This magnetic barrier immediately explains the increase with $B_\perp$ for $E_0 = E_b$, i.e. activation across a potential barrier. Eq. (6.7) gives a quantitative estimate of the expected additional energy barrier if the hopping distance is known.

In Chapt. 5 a hopping distance of $r_{ee} \approx 1/\sqrt{n_s}$ was observed. For the density regime shown in Fig. 6.17, $r_{ee} \approx 70 - 140\,\mathrm{nm}$. This would correspond to a magnetic barrier $E_B \approx 20 - 170\,\mathrm{K}$ at $B_\perp$=1.5 T or even $E_B \approx 170 - 670\,\mathrm{K}$ for $B_\perp$=3 T. This is, of course, much larger than any of the observed activation energies. The large discrepancy could be explained if the hopping distance is much smaller, for example, the observed difference of $\Delta E_0 = 1-2\,\mathrm{K}$ between $B_\perp$=1.5 T and $B_\perp$=3 T would suggest $r_{hop} < 10\,\mathrm{nm}$. This seems rather

small. However, another possible scenario is that disorder reduces the effective magnetic barrier. For the case of point scatterers along the hopping path, it has been shown that the magnetic barrier is strongly suppressed because it is "reset" at every scattering event [114]. This is schematically shown in Fig. 6.18. A more complex disorder potential may have a similar effect and could explain the relatively small change in E_0 with increasing $B_\perp$. The considerations in this paragraph should apply to all the localisation pictures discussed above, as long as the dominant transport mechanism is activation across a potential barrier between localised states.

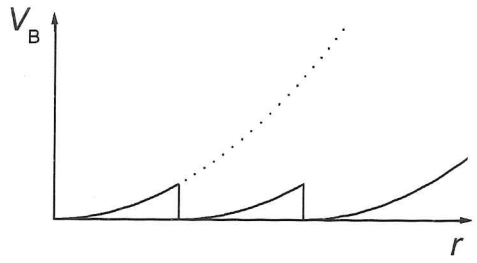

Figure 6.18: Magnetic confinement potential without scatterers (dotted line) and with scatterers (solid lines).

In the case where transport occurs by phonon assisted tunnelling and $E_0 = E_t$, the activation energy depends on the energies of the localised states themselves and not on the barrier height between them. In a clean 2DES a perpendicular magnetic field changes the density of states from a constant into a set of equispaced delta peaks, broadened by moderate disorder (see Sect. 4.1.2). This is not directly applicable to the strongly localised regime, but the magnetic confinement will still have an impact on the energies of the localised states. The change in energy would be expected to be in the order of the cyclotron energy $\hbar\omega_c/2$ ($\cong 10$ K for $B_\perp = 1\,\mathrm{T}$), which is the level spacing in a harmonic potential of the form (6.7). However, to determine E_t, the crucial thing is how the energy levels of different localised states change relative to each other. It is not clear how a magnetic field would affect the average energy difference between localised states in a complex system as a disordered interacting 2DES.

In Fig. 6.17, one can see that for both devices above a certain electron density, E_0 actually decreases when $B_\perp$ is increased from 0 to 0.5 and 0.7 T, respectively. This observation may be related to the negative magnetoresistance discussed in Sect. 5.4.1, which occurred over a similar range in $B_\perp$ and was assigned to interference effects. It is not clear how this could affect the activation energies, in particular since interference effects are not expected to be strong in the high temperature range where the activated behaviour was observed.

Chapter 7

Magnetic Field Induced Resistance Oscillations

This chapter discusses strong oscillations in the resistivity of localised mesoscopic 2DES that appear as a function of electron density and are induced when a strong perpendicular magnetic field is applied. Oscillations of this kind have not been previously reported in literature.

Importantly, the positions of peaks and troughs do not change with changing magnetic field. A possible universality of the positions of peaks is discussed, where peaks occur favourably at integer and half-integer values of r_s.

Scenarios that could cause such a behaviour are discussed, in consideration of the results presented in other chapters.

7.1 Overview

Fig. 7.1 gives an overview of the magnetically induced resistance oscillations for four devices with spacer width δ_{sp}= 20, 40, 60 and 80 nm at $T \cong 300$ mK. The dimensions of all the devices shown in this figure are $L \times W \cong 2-3\,\mu\text{m} \times 8\,\mu\text{m}$.

With decreasing n_s, the devices with intermediate disorder (Fig. 7.1 b) and c) with δ_{sp}=40 and 60 nm) exhibit a monotonic increase of resistivity with weak features at zero field (thick black lines). However, when a perpendicular magnetic field is applied, oscillations emerge with peaks that become more

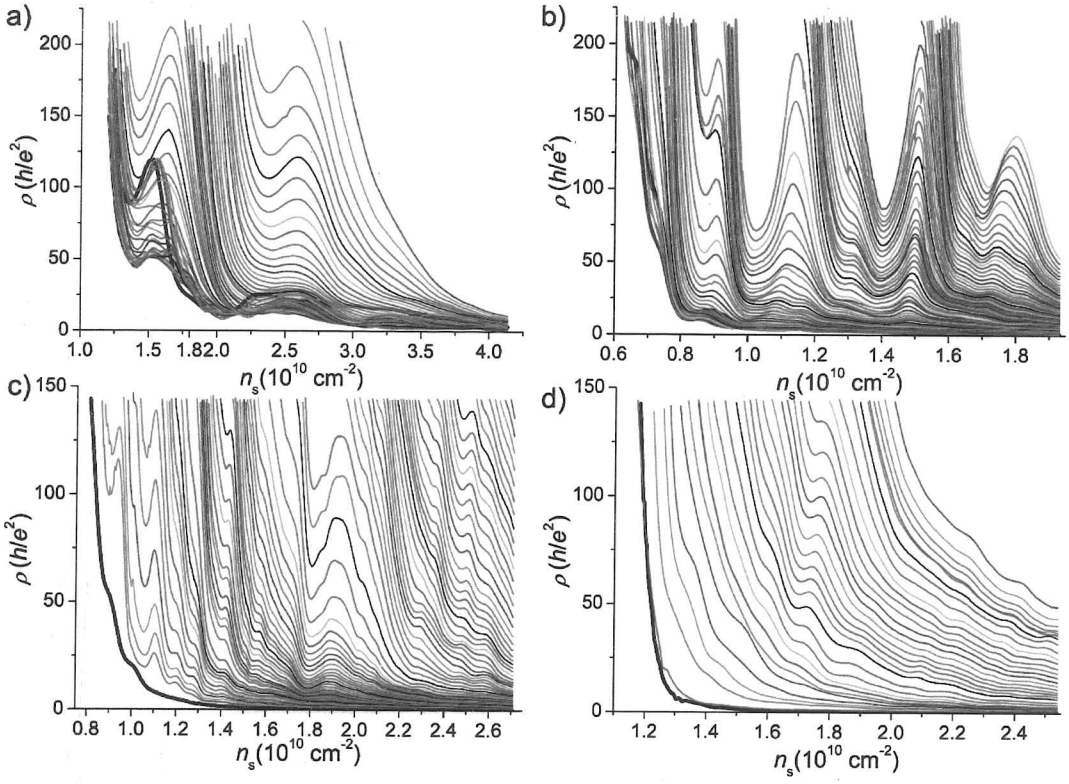

Figure 7.1: Overview of magnetic field induced resistance oscillation for devices from four different wafers. While at zero magnetic field (thick black lines) the resistivity increases mostly monotonically with decreasing n_s, peaks appear in a magnetic field, becoming more pronounced as $B_\perp$ gets stronger. All measurements at $T \cong 300\,\mathrm{mK}$.
a) A07b ($\delta_{sp} = 20\,\mathrm{nm}$), $B_\perp = 0 - 3\,\mathrm{T}$, $\Delta B_\perp = 0.05\,\mathrm{T}$. b) A78e ($\delta_{sp} = 40\,\mathrm{nm}$), $B_\perp = 0 - 4\,\mathrm{T}$, $\Delta B_\perp = 0.05\,\mathrm{T}$. c) C67b ($\delta_{sp} = 60\,\mathrm{nm}$), $B_\perp = 0;\ 0.92 - 6.7\,\mathrm{T}$, $\Delta B_\perp = 0.08\,\mathrm{T}$. d) T46a ($\delta_{sp} = 80\,\mathrm{nm}$), $B_\perp = 0 - 9.6\,\mathrm{T}$, $\Delta B_\perp = 0.3\,\mathrm{T}$ [92].

pronounced with increasing $B_\perp$. The device with strongest disorder (Fig. 7.1 a) with δ_{sp}=20 nm) shows one strong and one weaker peak even at zero field. As $B_\perp$ increases, the peaks are suppressed at first, but then become stronger again, eventually becoming much clearer than at $B_\perp = 0$. In all cases, the peak position in n_s remains practically unchanged as $B_\perp$ increases over ranges

of up to several Tesla.

The device with weakest disorder (Fig. 7.1 d) with δ_{sp}=80 nm) shows a rather different behaviour, where peaks are absent up to $B_\perp$ as large as 9.6 T, apart from one weak feature. Note that devices with δ_{sp}=80 nm also showed a qualitatively different behaviour of low field magnetoresistance (Chapt. 5) and temperature dependence (Chapt. 6) than devices with δ_{sp}=20-60 nm.

Devices made from the 40 nm δ-doped wafer A2678 generally were most stable and displayed strongest oscillations (as well as most interesting T-dependence, as discussed in Chapt. 6). Therefore, a second device from this wafer (A78f, $L \times W \cong 4\,\mu\text{m} \times 8\,\mu\text{m}$) is shown in Fig. 7.2 in several cooldowns. Fig. 7.2 a) was taken at $T \cong 300$ mK. Fig. 7.2 b) is at $T \cong 300$ mK as well, but in a different cooldown. Here, a different measurement set-up was used, that allowed to measure higher resistances, at cost of a lower accuracy (see Sect. 3.3.1 for details). It seems like the oscillations might become weaker again with increasing field in the very high resistivity regime, a trend that was never observed for $\rho \lesssim 200 \times h/e^2$. Finally, Fig.7.2 c) shows a measurement in a different cryostat at $T \cong 70$ mK. It exhibits the strongest oscillations of any device. The obvious reason for this would be the lower temperature. However, a different measurement of the same device showed only a very weak dampening of the oscillations at low n_s and low $B_\perp$, respectively, when the temperature was increased from $T \cong$65 mK to 300 mK (not shown). A strong T-dependence of the oscillations was only observed at very high fields $B_\perp \gtrsim 7$ T and small $r_s \lesssim 3.5$. This observation is in agreement with the saturation of the temperature dependence of resistivity at low temperatures as discussed in Chapt. 6, which was also weakened at high magnetic fields.

7.2 Universality in n_s or r_s?

When comparing the electron densities at which the peaks occur in Figs. 7.2 a)-c), one can observe a striking similarity. In particular at low densities a correlation between different cooldowns is observed both in spacing between the peaks and their actual positions. A first peak appears at $n_s \approx 10^{10}\,\text{cm}^{-2}$ followed by a series of peaks in the approximate separation of $\Delta n_s \approx 0.2 \times 10^{10}\,\text{cm}^{-2}$, although the peaks in a) seem to be slightly shifted towards higher

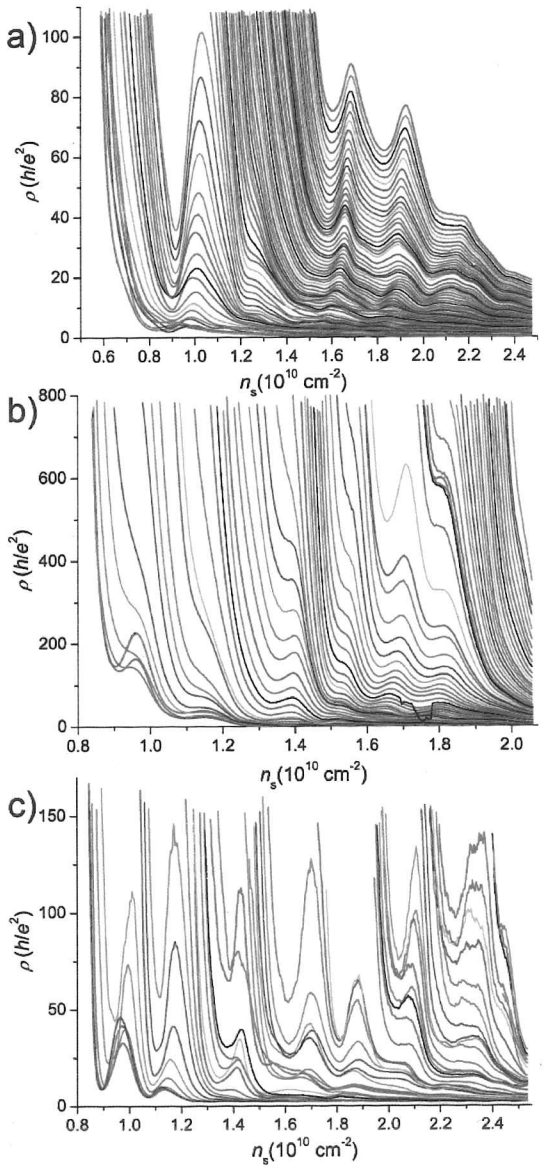

Figure 7.2: Overview of magnetic field induced resistance oscillations in different cooldowns for device A78f.

a) $B_\perp = 0 - 7\,\mathrm{T}$, $\Delta B_\perp = 0.1\,\mathrm{T}$, $T \cong 300\,\mathrm{mK}$. b) Different cooldown but same temperature $T \cong 300\,\mathrm{mK}$, measured to higher resistance in a different set-up (see Sect. 3.3.1). $B_\perp = 0 - 8\,\mathrm{T}$, $\Delta B_\perp = 0.125\,\mathrm{T}$ c) Measurement at lower temperature $T \cong 70\,\mathrm{mK}$ in a different cryostat. $B_\perp = 0 - 7.5\,\mathrm{T}$, $\Delta B_\perp = 0.15\,\mathrm{T}$.

densities. Remarkably, a clear correlation of peak position exists also to a different device from the same wafer (Fig. 7.1 b)) and to some extent even to a device from a different wafer (Fig. 7.1 c)). In particular, in all devices a strong single or double peak is observed at $n_s = 1.8 \pm 0.1 \times 10^{10}\,\mathrm{cm}^{-2}$. Even the low disorder device in Fig. 7.1 d) shows a feature at this density, which does not display any other peaks at all. The observation of a strong feature around $n_s = 1.8 \times 10^{10}\,\mathrm{cm}^{-2}$ was confirmed in *all measured devices*, including the ones not shown here.

The correlation between different cooldowns, different devices and even different wafers raises the question of what distinguishes particular densities where the peaks occur and if there may be a more appropriate quantity than n_s to express a possible universality in peak position and separation. In Chapt. 5 we have seen that certain properties of magnetoresistance were determined only by $r_{ee} \cong 1/\sqrt{n_s}$ for a wide range of devices and wafers. Also, resistance oscillations periodic in $1/\sqrt{n_s}$ have been reported before in 2DES of similar dimensions to the ones used here, although for the case of much stronger disorder in the impurity band of GaAs [115]. In fact, when the periodicity observed in Ref. [115] is expressed in terms of $r_s = 1/a_B^*\sqrt{\pi n_s}$, ones finds $\Delta r_s \approx 1/2$.

In view of this, it is instructive to look at the observed oscillations as a function of r_s rather than n_s. A first observation is that the density $n_s = 1.8 \times 10^{10}\,\mathrm{cm}^{-2}$, which appears to be somehow distinct, corresponds to an integral value of $r_s \cong 4$. In Fig. 7.3 four devices made from wafers with $\delta_{sp} = 20$, 40 and 60 nm are shown on a r_s-scale (these measurements are also shown in Figs. 7.1 and 7.2 but on a n_s-scale). Indeed, for all devices, a periodicity of $\approx 1/2$ is observed between the strongest peaks, except for device A07b (Fig. 7.3 a)), where the two peaks are separated by about 0.9. Also, in device A78f (Fig. 7.3 d)), the frequency seems to double at $r_s \leq 4$, but this could also be interpreted as a change to double peaks with the same frequency. With some good will, one can even assign the positions of the peaks to integral and half integral values of r_s, starting from $r_s = 5.5$ in Figs. 7.3 b)-d).

At this point, one should have a look at how strong an impact a possible error in the electron density measurements would have on r_s. It is crucial to know if the error in r_s is small enough to actually allow for a statement about the peak position to a precision smaller than 1/2. The density mea-

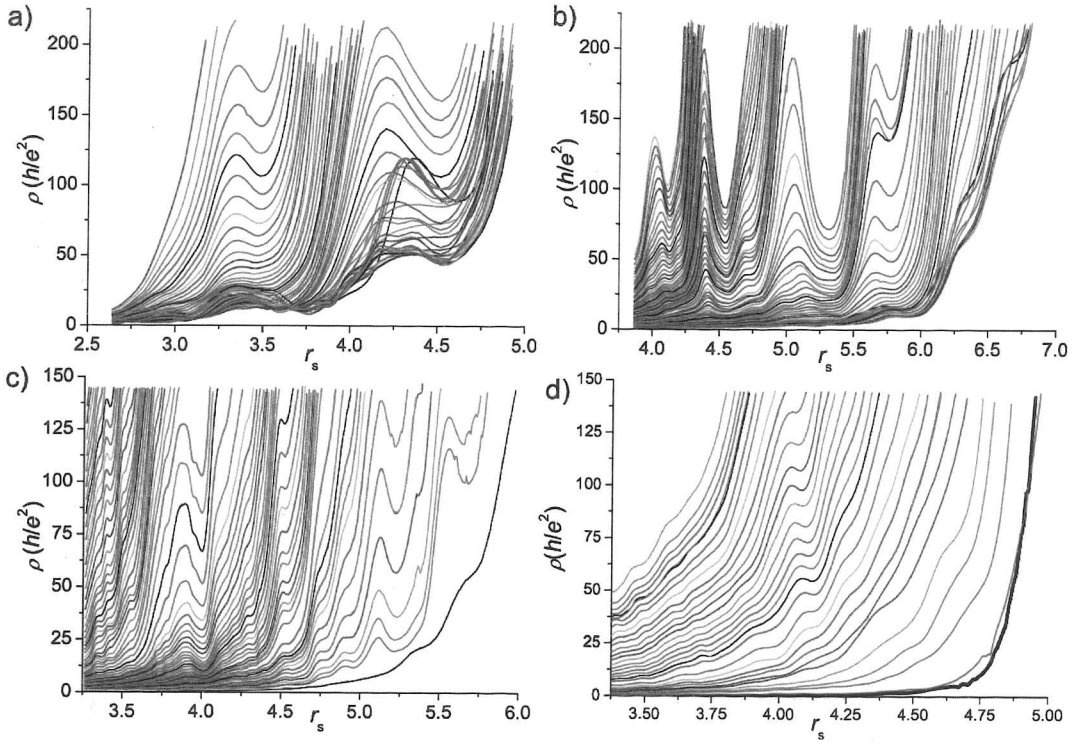

Figure 7.3: Oscillations for various devices with $\delta_{sp} = 20 - 60\,\mathrm{nm}$ on a r_s rather than n_s scale. In all cases, the separation between strong peaks appears to be $\Delta r_s \approx 1/2$, at least at lowest densities. One can even make out a possible trend of peaks appearing at half integral values of r_s or double peaks in d) at $r_s = 3.5$ and 4. In particular, all the measurement show a broad single or double feature at $r_s \approx 4$.

a) A07b ($\delta_{sp} = 20\,\mathrm{nm}$), $B_\perp = 0 - 3\,\mathrm{T}$, $\Delta B_\perp = 0.05\,\mathrm{T}$ (same measurement as Fig. 7.1 a)). b) A78e ($\delta_{sp} = 40\,\mathrm{nm}$), $B_\perp = 0 - 4\,\mathrm{T}$, $\Delta B_\perp = 0.05\,\mathrm{T}$ (same as Fig. 7.1 b)). c) C67b ($\delta_{sp} = 60\,\mathrm{nm}$), $B_\perp = 0$; $0.92 - 6.7\,\mathrm{T}$, $\Delta B_\perp = 0.08\,\mathrm{T}$ (same as Fig. 7.1 c)). d) A78f ($\delta_{sp} = 40\,\mathrm{nm}$), $B_\perp = 0 - 7.5\,\mathrm{T}$, $\Delta B_\perp = 0.15\,\mathrm{T}$ (same as Fig. 7.2 c)) [92].

surement technique used in our experiments and a way of estimating its error are discussed in Chapt. 4. The relative error increases with decreasing n_s, leading to a larger error at large r_s. The periodicity is, of course, less affected. For all devices from wafer A2678 an excellent density measurement could be done. Nevertheless, an error of $r_s^{Err} \approx 0.35$ has to be expected at $r_s = 5.5$ or $r_s^{Err} \approx 0.15$ at $r_s = 4$, an estimate which applies to the measurements shown in Fig. 7.3 b) and d). The measurement in Fig. 7.3 c) has a slightly larger error margin with $r_s^{Err} \approx 0.5$ at $r_s = 5.5$ and $r_s^{Err} \approx 0.3$ at $r_s = 4$. Fig. 7.3 a) has the largest uncertainty with $r_s^{Err} > 0.5$ even at $r_s = 4$. Such a large error could even explain the deviation from a 1/2 separation between the two peaks in this measurement.

In view of the relatively large error at high r_s, one should not overestimate the importance of the apparent coincidence of peaks with integral and half-integral values of r_s. However, at relatively low r_s the error is reasonably small, and the appearance of a strong peak at a universal value of $r_s \approx 4$ may be real.

An attempt at a more quantitative analysis of the peak positions is shown in Fig. 7.4. In a), the positions of clear peaks in terms of r_s have been determined and are presented in a histogram for 10 devices from five different wafers (δ-doped with $\delta_{sp} = 20$, 40, 60 and 80 nm and bulk-doped with $\delta_{sp} = 40$ nm) with gate dimensions $L \times W \cong 0.5 - 4\,\mu\text{m} \times 8\,\mu\text{m}$. In order to avoid too large an influence of a single device, each device was only analysed once, even when data from several cooldowns was available. Also, only measurements were used where at least a range of $r_s = 3.5 - 5$ was available. This makes sure that a peak in the histogram does not arise from the availability of data from more devices within this range. The histogram in Fig. 7.4 a) shows a relatively uniform distribution in that there is no overall trend of increase or decrease of peak density with increasing r_s. The latter would be expected, if the peaks where distributed uniformly in n_s rather than r_s. However, a clear maximum is observed around $r_s \approx 4$ and a weaker one at $r_s \approx 5$. The decrease in number of peaks for $r_s > 5$ must arise from the lack of available data due to pinch-off of transport in some of the devices at such low electron densities.

Fig. 7.4 b) shows a histogram of the measured separation in r_s between adjacent peaks. It exhibits a clear, if rather broad, maximum at $\Delta r_s \approx 0.4 -$

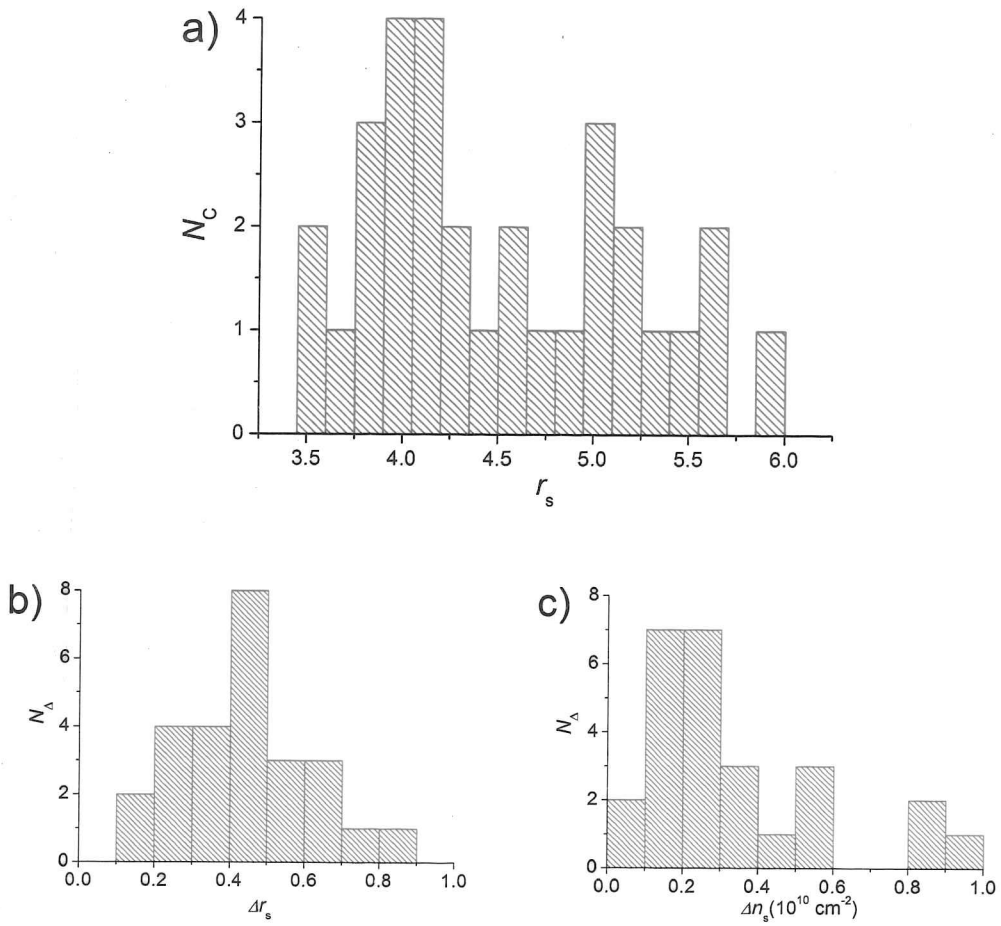

Figure 7.4: Histograms of the peak distribution from 10 devices from various wafers and of varying dimensions.

a) Peak counts N_c on an r_s-scale, showing a clear maximum around $r_s \approx 4$. b) and c) Separation between adjacent peaks in terms of r_s and n_s, respectively. Δr_s shows a broad maximum around 0.5, while Δn_s has a relatively sharp maximum around 0.2 but otherwise a more even distribution over the whole range.

0.5. If the peak separation is expressed in terms of n_s, a sharp peak appears around $\Delta n_s \approx 0.2$ but apart from that, there is a scattering of the distribution over quite a large range. This gives some evidence that the peaks may, indeed, be evenly spaced in r_s with a periodicity of approximately 1/2.

The problem in the experimental confirmation of a possible universality in the peak position in r_s is twofold. First of all, as discussed above, the error in measuring the electron density might be, in some cases, as large as the peak separation. In additions, there is also a more fundamental problem: An universality in peak position in r_s, independent of (mesoscopic) device dimensions and disorder strength within a certain window would, undoubtedly, suggest a fundamental origin of the observed resistance oscillations. However, it is also clear that disorder does play an important role. This is expressed in the difference of the strength of the peaks between different cooldowns and also by the fact that the oscillations practically disappear in a very low disorder device with $\delta_{sp} = 80\,\text{nm}$. The local disorder topology could lead to a deviation of the peaks from their fundamental position. For example, even though it is believed that the electron distribution is homogeneous on the length scale of our device dimensions, some fluctuations may, nevertheless, occur, inhibiting a perfectly well defined peak position.

In conclusion, some evidence of a universality of peak position in terms of r_s and a periodicity of $\Delta r_s \approx 0.5$ has been given. The available results do not allow for a definite conclusion in this direction. Nevertheless, due to the far reaching implications that a universality in such a fundamental quantity as r_s would have, I believe that the observation deserves the attention it was given in this section.

7.3 Temperature Dependence of Oscillations

Fig. 7.5 a) shows the temperature dependence of oscillations at $B_\perp$=2 T for device A78e in a temperature range $T = 0.3-4.6\,\text{K}$. One can see that the peaks are damped rather quickly and have disappeared at $T \approx 2\,\text{K}$. It is interesting to directly compare the temperature dependence of peaks and troughs. This is done in Figs. 7.5 b) and c), where the resistivity is plotted versus inverse

temperature $1/T$ for two pairs of adjacent minima and maxima. Interestingly, in both cases the activated part at high temperatures is only shifted in its resistivity, but the slopes and, hence, activation energies, are virtually unchanged between peak and trough. However, while in the minima, the saturation sets in at $T \approx 2\,\mathrm{K}$ transport remains activated down to $T < 1\,\mathrm{K}$ at position of the maxima. This observation clearly suggests a common origin of the oscillations and the saturated temperature dependence. The appearance of the oscillations seems to be caused by a shift in the saturation temperature and they disappear at a temperature where the behaviour is activated at all densities.

Qualitatively, a similar behaviour was observed in all investigated temperature dependences, even though the activation energy did not always remain entirely constant. The latter will be discussed in some more details in Sect. 7.3.2. As discussed in Sect. 6.3, the saturation tends to get weaker at high magnetic fields. In agreement with this, the peaks seem to become more sensitive to temperature changes at high fields. However, it is hard to quantify this effect, partly due to a lack of available data, but mainly because with increasing $B_\perp$ the low density peaks get pinched-off and new peaks appear at higher densities. Therefore, one would have to compare not only different fields, but also different electron densities, which makes a quantitative analysis difficult.

7.3.1 Connection to Metallic Behaviour

In the previous section, a possible relation between the saturated temperature dependence and the resistance oscillations was discussed. On the other hand, as discussed in Chapt. 6, a close connection between saturated and metallic behaviour of resistance must be assumed. It suggests itself that the resistance oscillations may also be connected to the metallic behaviour. A problem is, of course, that the metallicity gets suppressed in strong perpendicular magnetic fields, while the resistance oscillations are induced by such a field. Therefore, one has to investigate intermediate fields, where a possible metallic behaviour is not yet suppressed, but oscillations are already appearing.

A nice example is shown in Fig. 7.6 for device C67b, which displayed clear oscillations at a low perpendicular field $B_\perp = 0.5\,\mathrm{T}$, but also very strong metallic pockets. In a), one can clearly see a non-monotonic behaviour of the

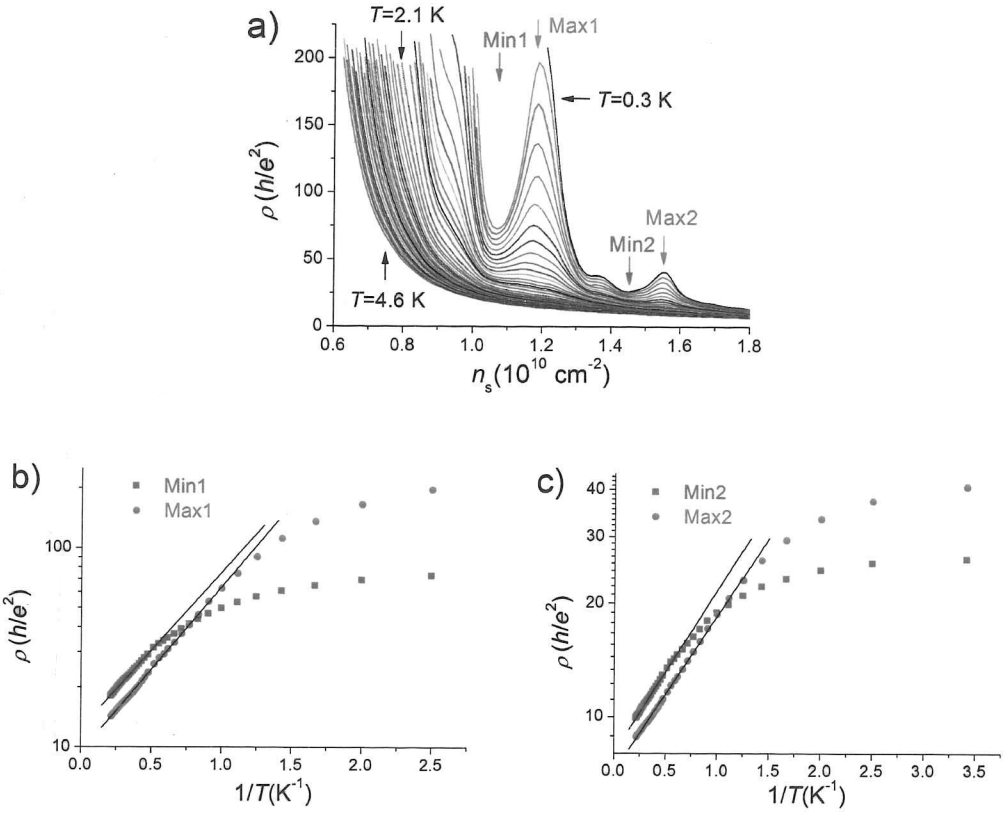

Figure 7.5: a) Temperature dependence of oscillations at $B_\perp$=2 T for device A78e, T=0.3-4.6 K. b) and c) Resistivity versus inverse temperature $1/T$ comparing pairs of minima/maxima as indicated in a). The solid lines are exponential fits to the activated parts on the T-dependence. While the slope (i.e. activation energy) remains practically unchanged between adjacent minimum and maximum, the saturation sets in at much higher temperatures at the minima [94].

temperature dependence of resistivity in the two minima that are marked with arrows. The resistivity as a function of inverse temperature $1/T$ is shown for these two troughs in Figs. b) and c), in comparison with the adjacent peak, also marked by arrows. The activated parts exhibit a very similar behaviour

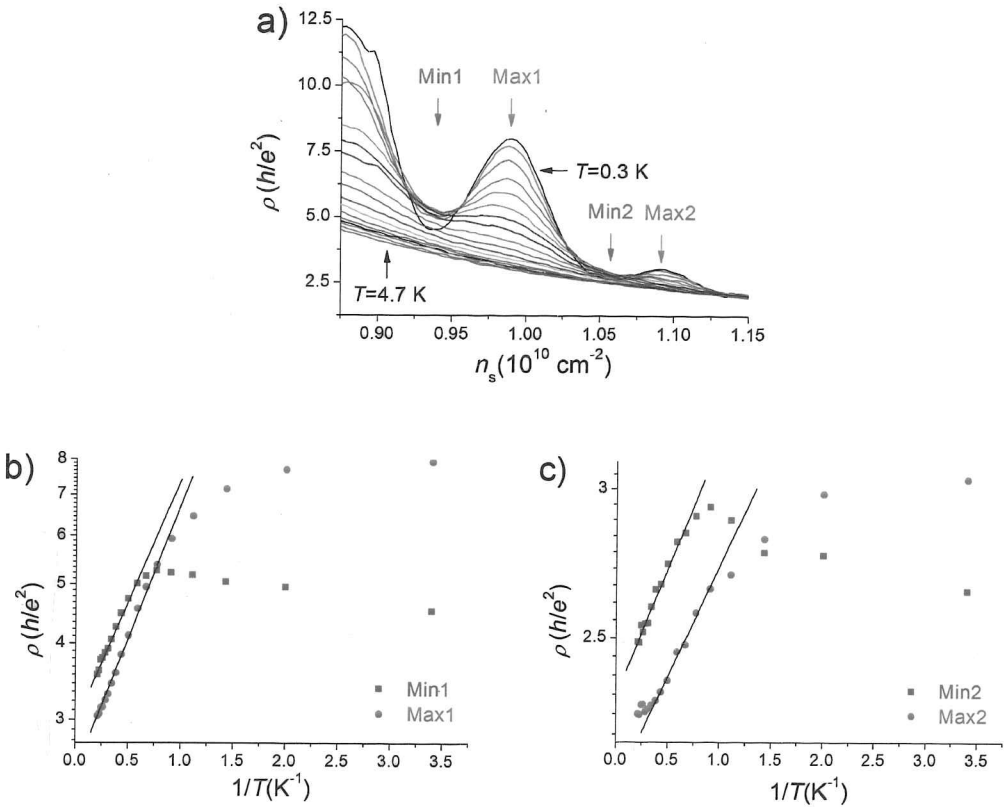

Figure 7.6: a) Temperature dependence of oscillations at $B_\perp$=0.5 T for device C67b, T=0.3-4.7 K. b) and c) Resistivity versus inverse temperature $1/T$ comparing pairs of minima/maxima as indicated in a). The solid lines are exponential fits to the activated parts on the T-dependence. As can be seen even under close inspection of a), a clear metallic behaviour occurs in the minima, while at the maxima a saturated but non-metallic T-dependence is observed.

to those shown in Fig. 7.5, with the activation energies virtually unchanged between adjacent minimum and maximum. However, while the T-dependence of the maxima only saturates, that of the minima turns into a clear metallic behaviour. Device A78e also showed a metallic pocket at $B_\perp = 0$ in the ap-

proximate position of minimum "Min1" as indicated in Fig. 7.5 a) and another one at a different magnetically induced trough. However, in this case, the oscillations were very weakly pronounced at the lowest fields. The observation of a coincidence between metallic behaviour with troughs gives further support to the conjecture that the origin of the magnetically induced oscillations is related to the saturated and metallic temperature dependence as discussed in Chapt. 6.

The two devices discussed so far in this section are the ones presented in the top two panels of Fig. 6.5. The lower two panels show much broader ranges of metallic behaviour. It should be noted that those two devices did not exhibit any magnetically induced oscillations in the range shown.

7.3.2 Activation Energies

In Sect. 6.4 the electron density and magnetic field dependence of the activation energies extracted from the high temperature exponential T-dependence was discussed. A general trend of decreasing activation energies with increasing n_s was observed. However, the decrease was not entirely steady, with plateaux or even dips formed at some densities. Here, this observation is revisited in connection with the resistance oscillations that are the topic of this chapter.

Fig. 7.7 shows the activation energies E_0 again for two devices from different wafers, but this time in direct comparison to the resistance oscillations of the respective device. A connection between resistance oscillations and the plateaux in the activation can immediately be seen, particularly clearly at the high field activation energies for device A78e (panel a)). E_0 is virtually unchanged between a trough in resistance and the next peak in direction of increasing n_s. Device C67b shows a qualitatively similar behaviour, but the plateaux are not as pronounced. This is not surprising since the oscillations themselves are also much weaker in this case.

The activation energies at low but finite field ($B_\perp = 0.7$ and $0.5\,\mathrm{T}$, respectively) show weak oscillations rather than plateaux. Both devices also showed strong metallic behaviour at these magnetic fields at some electron densities. As discussed in Sect. 6.4, the oscillations may be assigned to artefacts arising from a metallic component of transport impacting on the insulating trans-

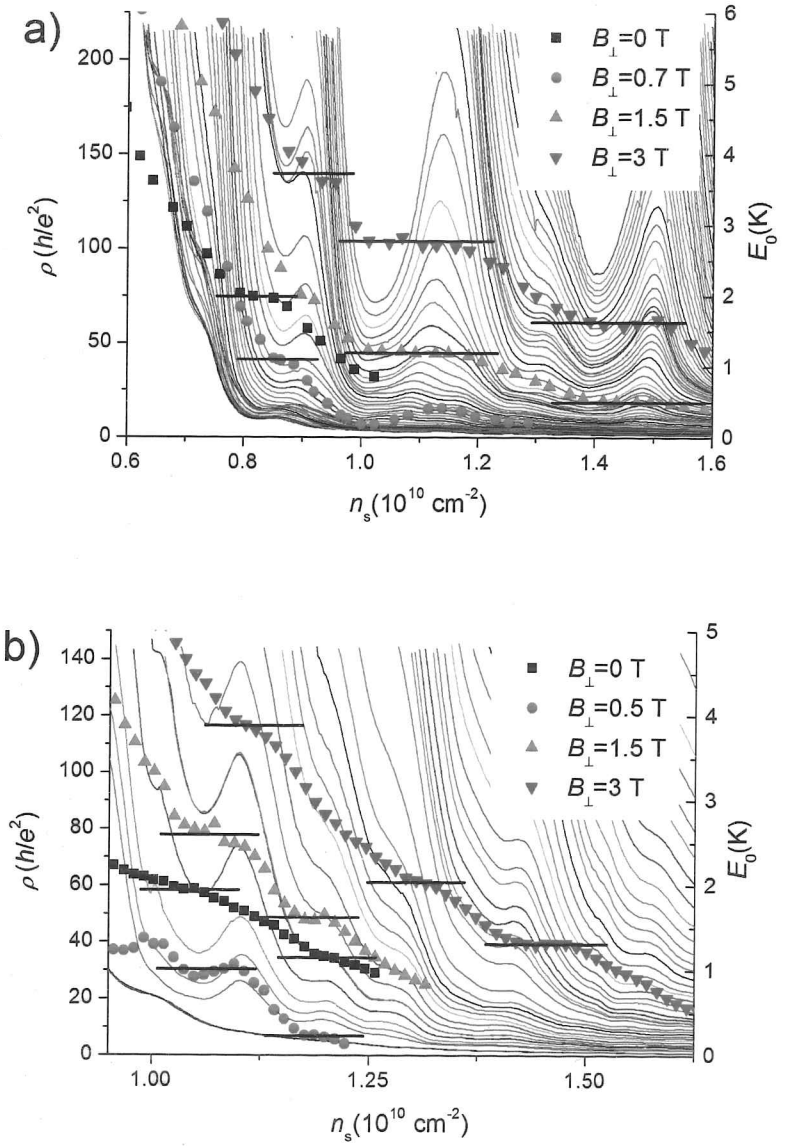

Figure 7.7: Activation energies E_0 and resistivity oscillations.
a) Device A78e: Several clear plateaux are formed in accord with the oscillations. They start approximately at the position of a trough and end at the next peak with increasing electron density. b) Device C67b: Qualitatively similar behaviour as A78e, but less pronounced [92].

port. On the other hand, it cannot be ruled out that the plateaux at higher fields arise from an oscillatory behaviour of E_0 on a strongly decreasing background. However, the broad horizontal characteristics of the plateaux make this unlikely.

7.4 Discussion

7.4.1 Magnetically Induced Coulomb Blockade Oscillations

Tripathi and Kenneth (TK, Refs. [97, 99]) have put forward a model to explain the behaviour of magnetoresistance and temperature dependence as presented in Chapts. 5 and 6 but also the resistance oscillations that appear at high fields, which they attribute to magnetic field induced Coulomb blockade oscillations. In this section, this picture is critically discussed and compared with the experimental data.

Brief Introduction to Coulomb Blockade Oscillations

The following short introduction to Coulomb blockade is based on the review articles Refs. [111, 116, 117].

Consider an isolated island of electrons separated from a source and drain by tunnelling barriers and separated from a metallic gate by a distance d_g. Because the island is isolated, the number of electrons N_e must be integral. For a current to flow through the island, an electron or a hole have to be added to the island. However, due to Coulomb repulsion, adding an electron costs an energy $E_c = e^2/2C$ (C the capacitance between island and the universe). This energy becomes large for a small island and, hence, small capacitance. This causes a gap in the tunnelling density of states of width e^2/C as shown schematically in Fig. 7.8 a).

The electrostatic energy of the island with charge Q is $E = -QV_g + Q^2/2C$ which can be rewritten as $E = (Q - Q_0)^2/2C$ within an additive constant, with $Q_0 = CV_g$. For any given V_g, Q will be adapted in order to minimise

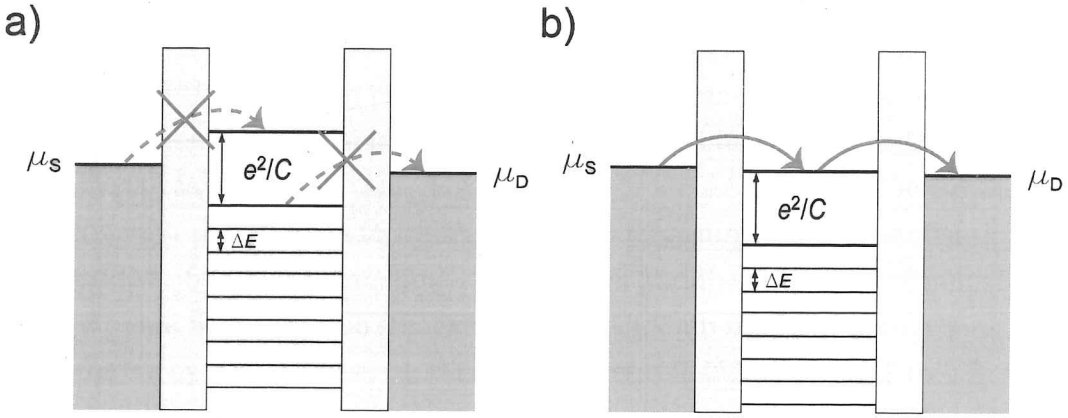

Figure 7.8: Schematic diagram of the Coulomb blockade effect.
a) The charging energy e^2/C blocks the tunnelling of an electron into the island (strictly at $T = 0$), the system is in the Coulomb blockade regime.
b) The highest unoccupied level in the island is aligned with the chemical potential in the leads ($\mu_{S,D}$) and the Coulomb blockade is lifted.
ΔE is the energy level spacing arising from confinement of the electrons.

E by tunnelling of electrons in or out of the island, with Q limited to integer multiples of e. When $Q_0 = Ne$, an integer number of electrons minimises E and for current to flow an activation energy $E_0^{\max} = e^2/2C$ is required. This situation is called Coulomb blockade regime and is schematically shown in Fig. 7.8 a). However, when $Q_0 = (N + 1/2)e$, the state with $Q = Ne$ and that with $Q = (N+1)e$ are degenerate and the Coulomb blockade is lifted (Fig. 7.8 b)). This effect leads to peaks in the conductance as the gate voltage is swept, with periodicity $\Delta V_g = e/C$. The activation energy E_0 varies between 0 and $E_0^{\max}$ over one period.

In very small islands (also called quantum dots), the energy level spacing ΔE arising from the confinement of the electrons may become comparable to the charging energy. Taking this into account, the periodicity changes to

$$\Delta V_g = e/C + \Delta E/e, \tag{7.1}$$

and the maximum activation energy becomes $E_0^{\max} = \frac{1}{2}(e^2/C + \Delta E)$.

Coulomb Blockade Oscillations in Disordered 2DES

TK propose that electron puddles formed at minima of the screened disorder potential should be considered as charged islands in which Coulomb blockade effects may be important. For Coulomb blockade to occur, the tunnelling rate between puddles has to be small enough to ensure charge quantisation on the puddles. Since the tunnelling rate between puddles decreases exponentially with $B_\perp^2$ (see Sect. 5.5) one can expect that Coulomb blockade oscillations may be induced by a strong perpendicular magnetic field. According to TK, in a situation of many droplets, the activation energies should be distributed randomly in the interval $[0,E_0^{\max}]$, changing with gate voltage. This should lead to a behaviour of resistance comparable to that observed in our mesoscopic devices. With increasing device dimensions and a large number of droplets, there will be some with arbitrarily low activation energy, giving rise to variable range hopping, which would explain the absence of the oscillation in macroscopic devices.

While this proposal is convincing in its simplicity and ability to explain several (but not all) other aspects of transport in the systems used in this thesis, there are a number of issues of both qualitative and quantitative nature.

The shape of the conductance peaks as a function of E_0 and V_g, which are linearly related, can be derived as [111]

$$G = \frac{G_0}{\cosh^2(\frac{E_0}{2k_BT})}, \quad G_0 = \frac{g_s e^2}{4hk_BT}\frac{\Gamma_l\Gamma_r}{\Gamma_l+\Gamma_r}, \tag{7.2}$$

where G_0 is the peak conductance with tunnelling rates $\Gamma_{l,r}$ with left and right neighbours and g_s the spin degeneracy. An attempt to fit this expression to several conductance peaks ($\sigma = 1/\rho$) is shown in Fig. 7.9. Note that Eq. (7.2) applies to the minima in resistance or maxima in conductance, respectively. The assumption $E_0 \propto (V_g - V_0)$ was made, with V_0 the position of the peak maximum. The agreement of the fits is rather poor. This can partly be explained by the asymmetry of the peak shapes. This could arise from an asymmetric change in the tunnelling barriers, leading to a V_g-dependent G_0. Such a change would not be surprising in the picture of TK where the quantum dots are not expected to be very symmetric and the tunnelling barriers are not decoupled from the main gate, as it would be the case in a lithographically

defined quantum dot. However, even in the cases where the peaks are relatively symmetric, the agreement with the fits is not good and it seem like the peak shape is qualitatively different from that predicted by Eq. (7.2).

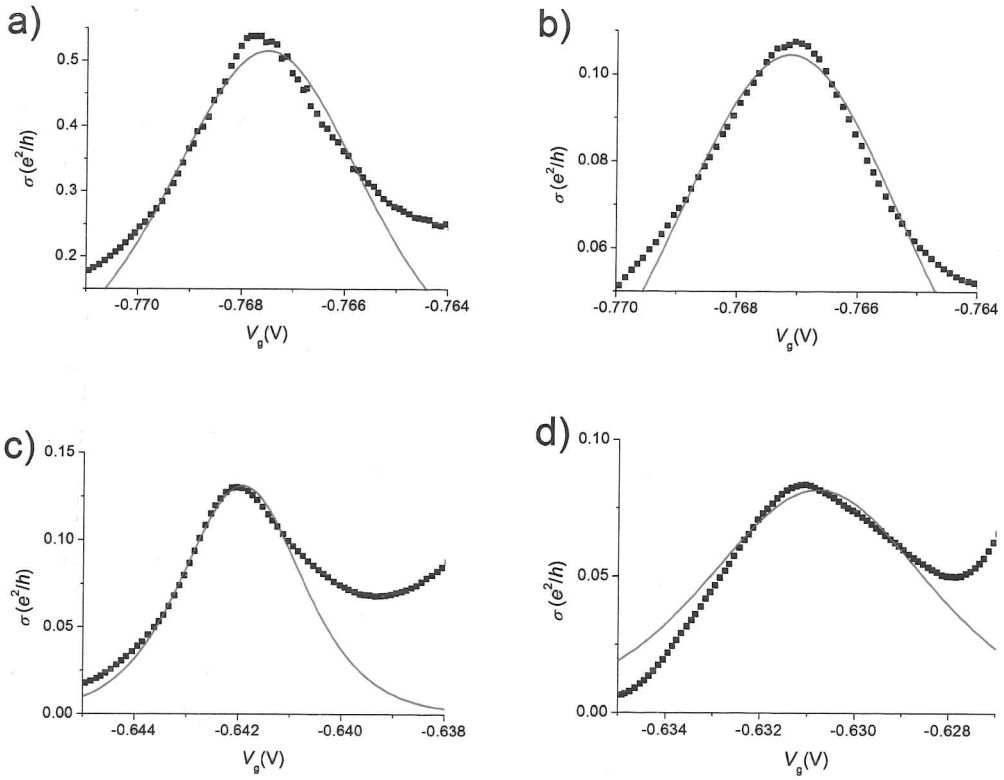

Figure 7.9: Fit of Coulomb blockade expression Eq. (7.2) to conductance peaks ($\sigma = 1/\rho$) for device A78f at various magnetic fields.
a) $B_\perp$=0.4 T, T=300 mK. b) $B_\perp$=1 T, T=300 mK. c) $B_\perp$=0.45 T, T=65 mK. d) $B_\perp$=1.35 T, T=65 mK.

TK also estimated the involved energy scales. For the case of of $\delta_{sp} = 50$ nm, they calculated an energy level spacing of $\Delta E \approx 6$ K and an effective charging energy $E_c^{Eff} \approx 4.4$ K, taking a depolarising effect from surrounding droplets into account. This gives a total maximum activation energy $E_0^{max} = \Delta E + E_c^{Eff} \approx 10$ K. According to Eq. (7.1) one gets a periodicity of Coulomb blockade

oscillations in gate voltage $\Delta V_g = 2E_0^{max}/e \approx 2\,\mathrm{mV}$. With a droplet diameter of 30 nm and separation of similar order (as estimated by TK), one would expect transport to occur through many droplets in parallel and in series. This should lead to an even shorter periodicity of oscillation. In fact, since the activation energies of the droplets should be distributed randomly in the interval $[0, E_0^{max}]$, one would expect a random distribution of peaks/troughs with average separation <2 mV. This is in strong contrast to the experimental observation of rather regularly spaced peaks/troughs, with an usual separation $\Delta V_g \approx 10 - 20\,\mathrm{mV}$.

The magnetic confinement arising from a strong perpendicular magnetic field also has an impact on the energy levels in the puddles. A rough estimate of the energy scales can be given as $\hbar\omega_c/2 \approx 10\,\mathrm{K}$ at $B_\perp = 1\,\mathrm{T}$ or 80 K at $B_\perp = 8\,\mathrm{T}$ [99]. One can see that this is of the order of or larger than ΔE and E_c^{Eff}. Hence, the Coulomb blockade oscillations should strongly depend on the magnetic field, which is, again, opposite to the observation that the peak and trough positions are virtually unchanged over ranges of up to several Tesla.

Finally, the picture of TK would predict the activation energies extracted from the high temperature activated part of the temperature dependence to be oscillatory in the interval $[0, E_0^{max}]$ with a disappearing E_0 in the resistance minima. While the activation energies at low fields show a weak oscillatory behaviour in some cases (although $E_0 = 0$ is never observed), the behaviour at higher fields, where resistance oscillations are strong, does not show oscillations but merely a formation of plateaux (Fig. 7.7).

Overall, while the scenario proposed by TK does give a qualitative description of some of our observations, the various qualitative and quantitative disagreements suggest that it does not fully explain the phenomenon.

However, in some cases a transport behaviour was observed that seems to agree better with TK's picture of puddle formation: Fig. 7.10 a) shows the resistivity as function of gate voltage at various magnetic fields for device A78f in a "bad" cooldown. Here, a top loading fridge was used, where a controlled slow cooldown is very difficult to achieve and where there might also have been a grounding problem during the cooldown. This might have prevented a smoothing of the disorder potential due to redistribution of remaining electrons

in the dopant layer, leading to a strongly inhomogeneous electron distribution even on a short length scale (see also Sect. 3.3.3). Note that TK do not take incomplete ionisation or correlations in the dopant layer into account. Hence, a device after a "bad" cooldown might be closer to the situation described by their theory.

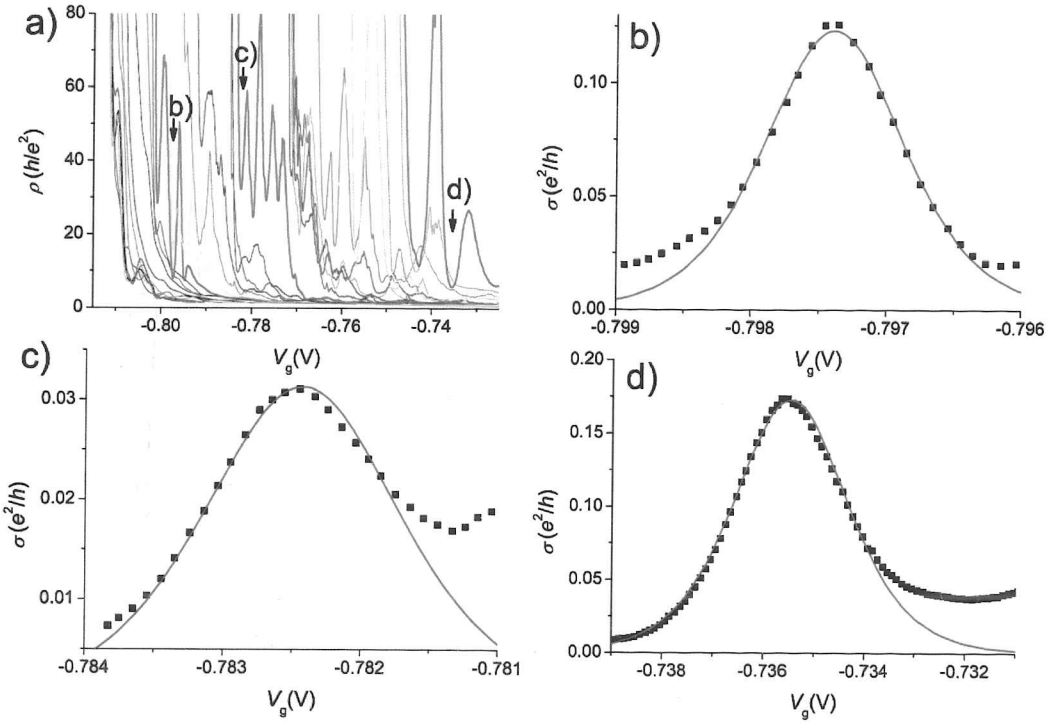

Figure 7.10: a) Resistivity with increasing magnetic field $B_\perp = 0 - 2.7\,\mathrm{T}$ for device A78f in a "bad" cooldown. Note that this measurement, while looking messy, is entirely reproducible. (T=25 mK)
b)-d) Fit of Coulomb blockade expression Eq. (7.2) to conductance peaks indicated by arrows in a). The agreement is significantly better than in a "good" cooldown. b) $B_\perp = 1\,\mathrm{T}$, c) $B_\perp = 1.6\,\mathrm{T}$, d) $B_\perp = 2.7\,\mathrm{T}$.

Indeed, the behaviour shown in Fig. 7.10 a) agrees better with TK's predictions in several respects. This data, while looking a bit messy, was entirely reproducible. Individual ρ vs. V_g traces at constant field generally show an ir-

regular appearance of peaks, which could be explained by uncorrelated change between Coulomb blockade and resonance of various puddles. However, in some cases, a rather regular set of oscillations occurs, which could be caused by a single dot dominating transport over a certain range of gate voltage. Three of these traces are highlighted in Fig. 7.10 a). The periodicity of these oscillations is approximately $3 - 10\,\mathrm{mV}$ which is much closer to the expected value $\Delta V_\mathrm{g} \approx 2\,\mathrm{mV}$. Fitting of expression (7.2) to conduction peaks in this case was much more successful (but still not perfect) as shown in Figs. 7.10 b)-d). As the magnetic field is increased stepwise, the oscillations change in a seemingly random manner, which could be explained by the change in the dot energy levels by a change in the strength of magnetic confinement.

7.4.2 Alternative Explanations

Here, some alternative explanations of the discussed resistance oscillations are presented. They are mainly qualitative and in some cases speculative due to lack of a good theoretical understanding of interacting disordered two-dimensional electron systems.

Interference or Quantum Hall Effect

It is highly unlikely that any effect related to the quantum Hall effect or an interference effect is the cause of the resistance oscillations. Both effects would have to depend strongly on magnetic field. If e.g. the resistance peaks were arising from some kind of coherent backscattering, the area enclosed by the involved loops would have to be so small that the change in magnetic flux $\phi \ll \phi_0 = h/2e$ (ϕ_0, the flux quantum) over the range of magnetic field where the peak position remains unchanged. For a change of $\Delta B_\perp$=4 T, this means that the loop areas would have to be much smaller than $5\times10^{-16}\,\mathrm{m}^{-2}$, corresponding to a circle of radius 12 nm, which seems unrealistic. Similarly, if the peaks were related to a certain quantum Hall filling factor, a change in magnetic field from $B_\perp = 1$ to 5 T would require the electron density to change by a factor of 5 in order to keep the filling factor constant, which can be ruled out from the experimental observation.

Commensurability of an Electron Solid

If the electrons are forming a crystal, there could be a commensurability effect between the lattice constant of the solid with another length scale of the device. As the electron density changes, the lattice would repeatedly change in and out of commensurability with strong impact on the ordering of the crystal. There could, for example, be a trend for the crystal to remain commensurate over a small range of electron density by introduction of defects rather than change of the lattice constant, followed by a sudden reorganisation and change to the next commensurate lattice constant. Any such commensurability effect could be enhanced by an increased sturdiness of the solid due to the localising effect of the magnetic field.

A possible length-scale could be the width of the device, e.g. the width being a multiple of the lattice constant. For this case, a rough quantitative estimate can be made: Let us assume for simplicity that the lattice constant is $r_{\mathrm{ee}} = 1/\sqrt{n_{\mathrm{s}}}$. At a width of $8\,\mu$m the commensurate state of 100 lattice constants fitting into the width corresponds to $r_{ee} = 80\,$nm, which is a typical value for our experiments. The change in r_{ee} to reach the next commensurate state is $\Delta r_{\mathrm{ee}} < 1\,$nm, which is more than an order of magnitude smaller than the usual observation of $\Delta r_{\mathrm{ee}} \gtrsim 10\,$nm. An uncertainty in the width or a different lattice geometry cannot explain such a large discrepancy. Hence, this kind of commensurability is unlikely to explain the observation.

A different origin of the commensurability could be with the background disorder. Such an effect would be particularly strong if there was some regularity in the disorder. In fact, due to the incomplete ionisation of the dopants, a certain degree of correlation in the disorder potential is possible (see Sects. 2.2.2, 3.3.3 and 9.2.1). Indeed, some evidence of an ordering in the background potential with possible formation of an antidot array with a separation of approximately $0.5 - 0.6\,\mu$m has been found in devices similar to the ones used here [118]. When doing a similar estimate of commensurability conditions as above, but compared to a length scale of $0.6\,\mu$m, one gets $\Delta r_{\mathrm{ee}} \cong 5 - 20\,$nm for a realistic range of $r_{\mathrm{ee}} \cong 50 - 120\,$nm with largest Δr_{ee} at largest r_{ee}. This is in much better quantitative agreement with the observed behaviour. Even if the background potential is completely irregular, due to the finite size of the device, there could be certain electron densities where the electron lattice is

in better or worse "agreement" with the background disorder. This could still lead to resistance oscillations, even though in this case they would probably be quite irregularly spaced.

A third possible length-scale could be the lattice constant of the GaAs itself, which is $a_0(\mathrm{GaAs}) = 5.65\,\text{Å}$ [28]. In this case, one would expect a commensurability to arise from the lattice constant of the electron solid being an integer multiple of the lattice constant of GaAs. This would lead to a periodicity $\Delta r_{\mathrm{ee}} \cong a_0(\mathrm{GaAs})$, which is much smaller than the observed value. Therefore, this kind of commensurability can be practically ruled out.

In view of the idea of quantum diffusion and defect delocalisation (discussed mainly in Chapt. 6), another closely related explanation is possible. The transitions between metallic and non-metallic phase were interpreted as changes between ordered and disordered states of an electron crystal, enabling and suppressing defect delocalisation, respectively. Also, in Sect. 7.3.1 of this chapter, a possible connection between metallic behaviour of temperature dependence and minima in the resistance oscillations was presented. One could imagine that the metallic phase is much less affected by a perpendicular magnetic field, leading to the appearance of trough in the resistance oscillations. The change of disorder of the crystal could, of course, be related to the commensurability effects discussed above.

More Exotic Scenarios

In Sect. 2.4.2 theoretical predictions of several exotic phases of interacting 2DES were mentioned, including striped or bubble phases or a coexistence between Wigner crystal and Fermi liquid. Not much is known about the transport behaviour in such phases, but density driven transitions of the phase, e.g. changes in bubble size, changes from bubble to stripe phase or vice versa, may well lead to sudden changes in the resistivity of the system. Of course, there could be something completely new which nobody has thought of (or someone has, but I have not heard of).

None of the scenarios discussed here give a good explanation of a possible universality in r_{s} and the observations discussed in Sect. 7.2 have to be left unexplained, for now at least.

Chapter 8

Amplified SdH-Oscillations and Modified Hall Resistance

This chapter presents experimental results that concern the Shubnikov-de Haas oscillations and the quantum Hall effect in small Hall bars. They were discovered along the way and seem not immediately connected to the main focus of the thesis, which is transport on a mesoscopic length-scale in the low-density regime. However, the discussion introduces some ideas that suggest that the observations may be more closely related to the mesoscopic low-density 2DES than one would think at first sight.

It was observed that the low-field magnetoresistance in the high resistance regime under the gate, picked up the SdH-oscillations of the ungated part of the device and reproduced them with a strongly amplified amplitude, which cannot be explained as a simple series resistance effect. Furthermore, the Hall resistance in the quantum Hall regime, which should not be affected by the presence of a gate in the middle of the Hall bar, showed strong modifications when the gate was swept into the low-density regime.

To the author's knowledge, neither of the observations have been previously reported. The finding was not investigated with priority and therefore, this chapter should be viewed as presentation of preliminary results. Accordingly, the discussion is kept short and only some ideas for possible direction of the interpretation are given.

8.1 SdH-Like Oscillations

8.1.1 Overview

In Chapt. 5 the magnetoresistance in the localised regime of mesoscopic 2DES was discussed in detail. One observation that was not presented was that the low field MR often had very clear oscillations superimposed on it. One example is shown in Fig.8.1 for several gate voltages, but similar behaviour was observed in many devices. While the amplitude of the oscillations decreases rapidly with increasing gate voltage (increasing electron density), the position of peaks and troughs is perfectly unaffected by the change in V_g.

The oscillations are clearly periodic in the inverse of the perpendicular magnetic field $1/B_\perp$. In fact, it turns out that they are almost perfectly in sync with the Shubnikov-de Haas oscillations in the ungated part of the device. These can, of course, be measured when the gate voltage is set to 0. A comparison between the normal SdH-oscillations (blue) and their equivalent in the high resistance regime (red), in the following called SdH-like oscillations, is shown in Fig. 8.1 b). A clear correlation between the two is observed, but the SdH-like oscillations are slightly shifted towards smaller $B_\perp$.

The most obvious explanation of the observation is that the four-probe resistance measurement simply picks up the normal SdH-oscillations from the ungated part of the device as a series resistance. However, this cannot be the case: The amplitude of the SdH-oscillations is at most $0.06\,\mathrm{k}\Omega$, but that of the SdH-like oscillations is up to $0.2\,\mathrm{M}\Omega$, i.e. more than 3 orders of magnitude larger.

8.1.2 V_g-Dependence

The amplitude ΔR of the SdH-like oscillations is strongest at lowest gate voltage (lowest density under the gate) and becomes very small at higher gate voltage. This is shown for two devices in Fig. 8.2. Both devices show an overall decreasing trend with increasing V_g, but while device A77a shows a mostly monotonic decrease, C67b shows a strong peak at intermediate gate voltages.

This peak becomes even clearer, when the data is presented in terms of

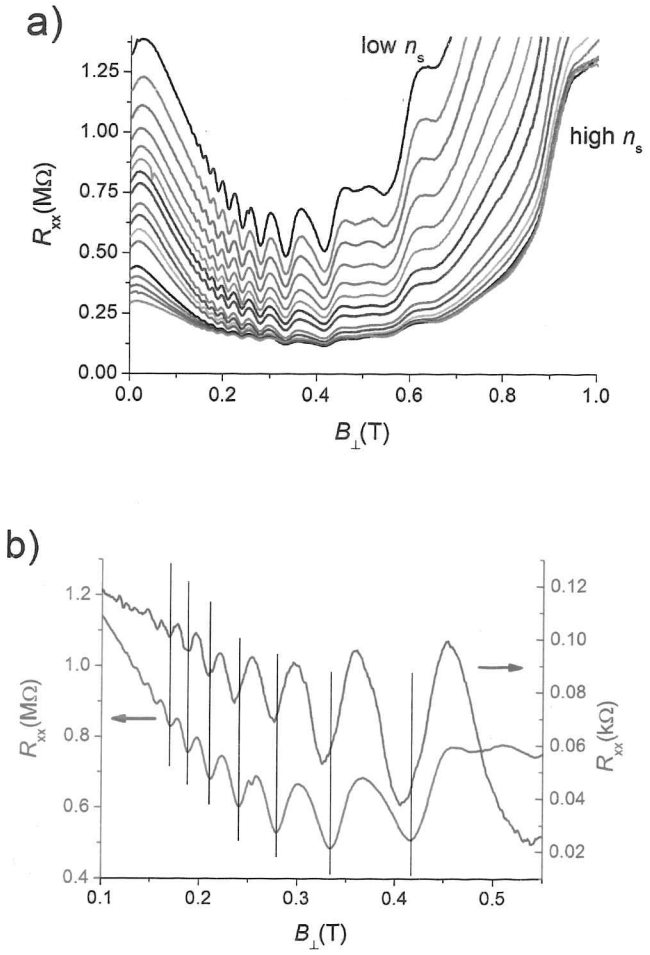

Figure 8.1: SdH-like oscillations in device C67b at T=300 mK.

a) Comparison of oscillations at various gate voltages ($V_g = -0.152 \rightarrow -0.149$ V). While the oscillations get weaker with lowering electron densities under the gate, the periodicity is completely unaffected. b) Comparison between SdH-like oscillations at $V_g = -0.152$ V with the SdH oscillations at $V_g = 0$. A clear correlation between the two is observed, even though peaks and troughs are shifted slightly towards higher $B_\perp$ in the SdH-like oscillations. The maximum amplitude of the SdH-like oscillations is $\approx 0.2\,\mathrm{M}\Omega$ compared to $\approx 0.06\,\mathrm{k}\Omega$ in normal SdH oscillations, ruling out a simple series resistance effect.

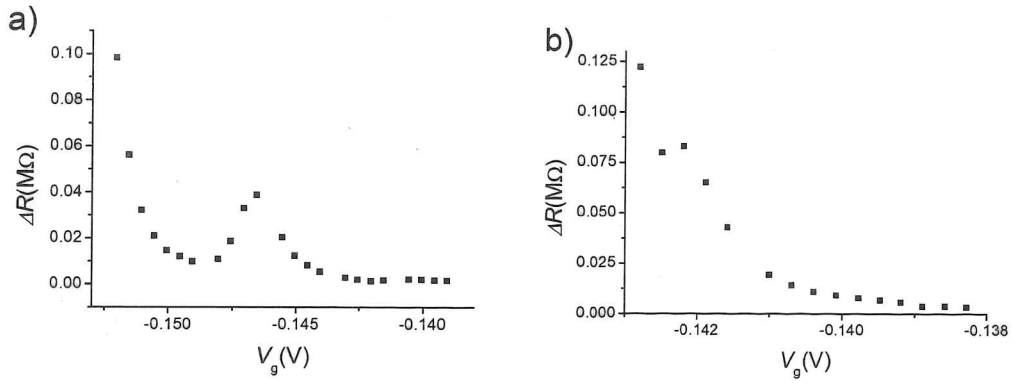

Figure 8.2: Gate voltage dependence of the amplitude ΔR of SdH-like oscillations at T=300 mK.

a) C67b, $B_\perp \cong 0.33$ T ("filling factor" $\nu = 10$). b) A77a, $B_\perp \cong 0.46$ T ("filling factor" $\nu = 14$).

relative amplitude $\Delta R/R$ as shown in Fig. 8.3, where $\Delta R/R$ is actually significantly larger at intermediate gate voltages than at the lowest V_g. The figure also includes the V_g-dependence of the longitudinal resistance at various fixed magnetic fields, showing the resistance oscillations discussed in Chapt. 7.

Interestingly, the peak in $\Delta R/R$ seems to be approximately situated between two peaks in $R_{xx}(V_g)$. The peak $\Delta R/R$ starts approximately at the position of one peak in R_{xx} and ends approximately at the next following R_{xx}-minimum. It should be noted, that device A77a, which shows a more monotonic behaviour of ΔR also did not show any strong peaks in $R_{xx}(V_g)$. These observations give some evidence that the strength of the SdH-like oscillations might be related to the resistance oscillations. However, for a definite statement, more data would be required.

8.1.3 T-Dependence

The temperature dependence of the SdH-like oscillations in device C67b for a range of $T = 0.3 - 2.1$ K is shown in Fig. 8.4 a). The oscillations are

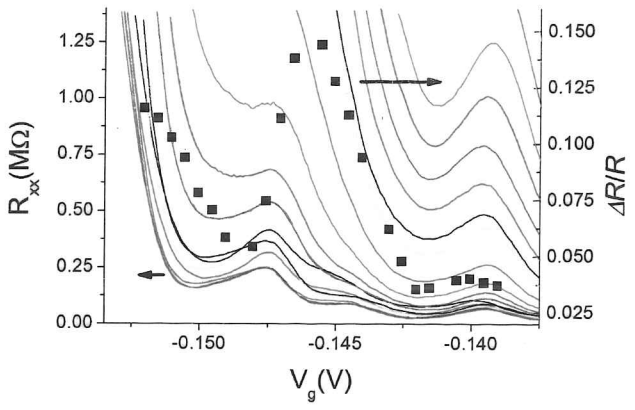

Figure 8.3: Gate voltage dependence of the amplitude $\Delta R/R$ of SdH-like oscillations at T=300 mK for device C67b, compared to magnetic field induced resistance oscillations (see Chapt. 7).

damped quickly and by $T = 1.5\,\mathrm{K}$ they have practically disappeared. The temperature dependence of the relative amplitude $\Delta R/R$ at "filling factor" $\nu = 8$ ($B_\perp \cong 0.41\,\mathrm{T}$) is shown in Fig. 8.4 b). As discussed in Sect. 3.3.2, the temperature dependence of normal SdH-oscillations should follow Eq. (3.1). The solid line in Fig. 8.4 b) represents an attempt to fit this expression to the T-dependence of SdH-like oscillations. Clearly the agreement is poor and the damping in the data seems to be faster than predicted by Eq. (3.1).

For comparison, the T-dependence of the real SdH-oscillations in the same device and at the same filling factor is shown in Fig. 8.4 c). Here, a fit of Eq. (3.1) produces an excellent result. This direct comparison confirms that the temperature dependence of the SdH-like oscillations is qualitatively different from that of the normal SdH-oscillations.

8.1.4 Discussion

The edge state picture of the quantum Hall effect (discussed in Sect. 4.1.5) could give a possible explanation of the SdH-like oscillations, or at least a direction for a possible explanation.

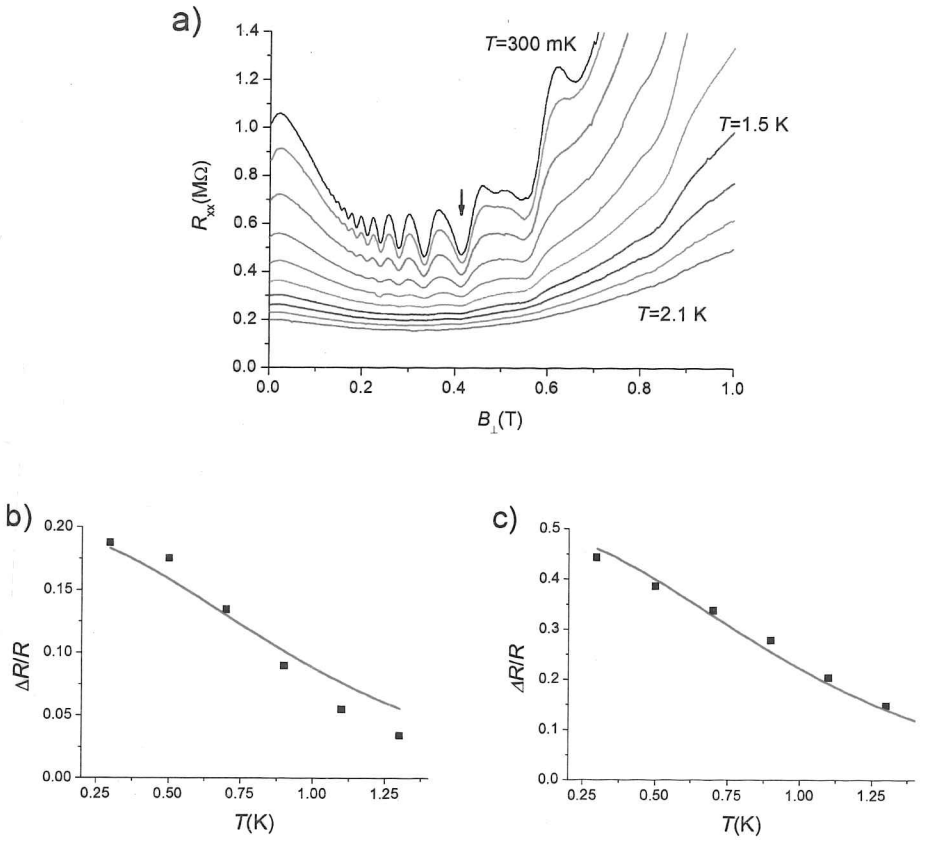

Figure 8.4: a) Temperature dependence of SdH-like oscillations in device C67b at V_g=-0.15 V. At T=1.5 K the oscillations disappear almost completely. b) Temperature dependence of relative amplitude $\Delta R/R$ of SdH-like oscillations at "filling factor" $\nu = 8$ ($B_\perp \cong 0.41$ T), indicated by arrow in a). The solid line is an attempted fit of Eq. (3.1). No good agreement is found and the temperature dependence seems to be stronger than that of normal SdH-oscillations. c) Temperature dependence of relative amplitude for normal SdH-oscillations in same device at the same filling factor. The fit of Eq. (3.1) is in much better agreement.

Unfortunately, in both devices where SdH-like oscillations were investigated, a reliable density measurement was not possible. However, one can safely assume that in the regime of gate voltage and magnetic field where the oscillations were observed, the electron density was low enough for most, if not all, edge states to be reflected at the gate. In all cases, the 2DES under the gate was localised with a resistivity $\rho > h/e^2$. In this case, even when the filling factor $\nu > 1$, edge states cannot really exist under the gate. In such a situation the charge carriers travel along the width of the gate in the edge states. Transport across the gate occurs by hopping of electrons out of the edge states, into and through the localised 2DES under the gate and into the edge states on the other side. As the magnetic field is swept upwards, the filling factor in the ungated part and, hence, the number of edge states decreases and the current along the gate will now be carried among fewer edge states. It seems likely that transport across the gate, while dominated by the resistance of the localised 2DES, will be affected by these repeated changes in the edge states. This could lead to a situation where the total resistance in dominated by the localised 2DES but modulated by changes in the leads.

The non-monotonic dependence of the amplitude of the SdH-like oscillations on gate voltage suggests that the gate cannot be viewed just as a simple non-interacting barrier in our case and that the oscillations are affected by the state of the 2DES under the gate as well as by the 2DEG in the ungated part of the device.

A possible scenario how this could happen might be related to the work of Freyn *et al.* [119], who studied the transmission $|t_s|^2$ of an interacting scatterer connected to one dimensional leads of non-interacting electrons. They found that the transmission of an interacting scatterer is non-local and depends on the non-interacting measurement probes. When the phase of the Friedel oscillations in the leads was changed, $|t_s|^2$ varied significantly. This effect disappeared when the interactions in the scatterer were switched off. While these results cannot be directly applied to the observation describe here, the systems do have a close similarity to the model studied by Freyn *et al.*, the main difference being that both leads and "scatterer" (the localised 2DES under the gate) are two-dimensional. The changes occurring in the leads due to quantum Hall effects may have a similar impact on the transport across the localised

2DES, if the latter is strongly interacting.

8.2 Modification of Hall Resistance

8.2.1 Overview

When measuring the gate voltage dependence of the Hall resistance R_{xy} on either side of the gate, another unexpected effect occurred. At $V_g = 0$ the expected behaviour of the Hall resistance was seen, with a linear $B_\perp$-dependence at low fields and formation of Hall plateaux at higher field. However, at negative enough gate voltages, a strong modulation of the Hall resistance in the quantum Hall regime was observed. Note that it was made sure that the gate never pinched off too much and the excitation current remained constant at all times. In order to avoid heating, but still get a reasonable measurement signal, a current I_{ex}=300 pA was used.

As shown in Fig. 8.5, the Hall resistance showed strong oscillations. These oscillations were correlated to the quantum Hall effect, with one period corresponding to a change in ν by two (odd ν were not resolved). Interestingly, the sign of the oscillations depended on the configuration of the current and voltage probes in the four-probe constant current set-up. To explain this, a schematic of the device with numbered current and voltage probes is shown in Fig. 8.6. Assume that the current probes I_+ and I_- are connected to I_1 and I_2, respectively. When the voltage probes V_+ and V_- were connected to V_1 and V_3, i.e. on the side of I_+, an increase of R_{xy} was observed at the position where a quantum Hall plateau was expected and a dip was seen at the risers between two plateaux.

When V_+ and V_- were connected to V_2 and V_4, i.e. on the side of I_-, the sign of the total measured R_{xy} remained the same, as expected. However, the modulation of the Hall resistance now showed the exact opposite behaviour, with a dip where a plateau is expected and a peak in place of the risers. Qualitatively the same behaviour was observed in both devices that were investigated for these modulations of Hall resistance.

Fig. 8.7 shows the deviation more clearly. Here, $\Delta R_{xy} = R_{xy} - R_{xy}(V_g = 0)$ at various gate voltages is shown as a function of the perpendicular magnetic

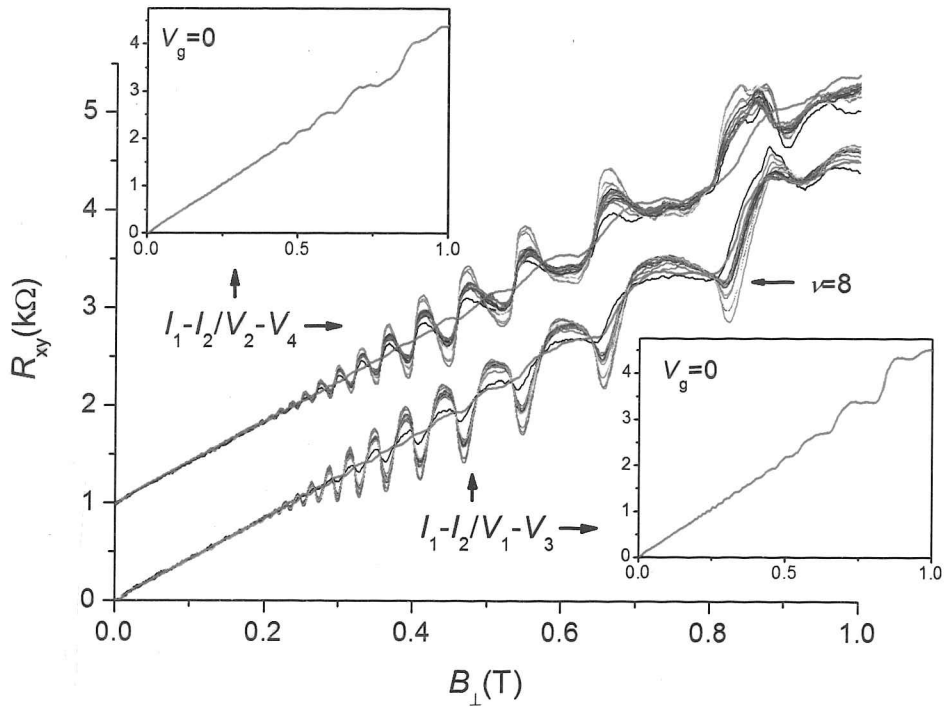

Figure 8.5: Modification of Hall resistance R_{xy} at various gate voltages ($V_g = -0.143 \rightarrow -0.13\,V$) for device A77a at $T = 300\,mK$. Two different combinations of current and voltage probes in the four-probe measurement are shown (see Fig. 8.6 for labelling), with one of them offset by $+1\,k\Omega$. The Hall resistance at $V_g = 0$ is included in the main graph (red lines) but also shown in the insets. While the Hall resistance at $V_g = 0$ exhibits the expected behaviour, at strong negative gate voltage, strong oscillations appear. The phase of the oscillations depends on the side on which the resistance is measured: If R_{xy} is measured on the I_+-side, it is increased at the plateaux positions and suppressed at the risers. The opposite is observed when the Hall probes are on the I_--side.

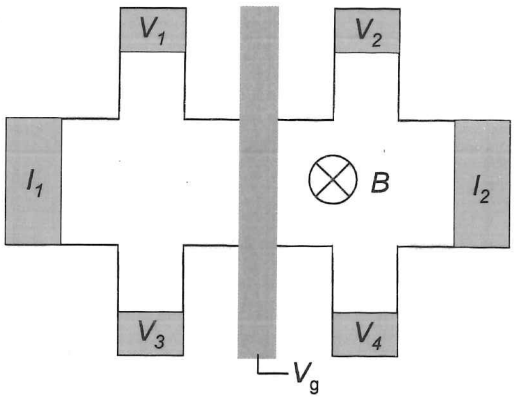

Figure 8.6: Schematic of a Hall bar device with current and voltage probes and gate.

field, i.e. the Hall resistance at zero gate voltage has been subtracted from the measured Hall resistance when a large negative gate bias was applied. It shows very clear oscillations of varying amplitude, but sharp crossing points with the magnetic fields where $\Delta R_{xy} = 0$ almost identical for all gate voltages.

8.2.2 V_g-Dependence

An interesting observation is that, while at a fixed magnetic field, the sign of ΔR_{xy} is opposite on opposite sides of the gate, the amplitude is strongly correlated. In Fig. 8.8, ΔR_{xy} is shown as a function of gate voltage for three different magnetic fields in two different devices. In each panel, ΔR_{xy} measured with voltage probes on one side of the gate is compared to $-\Delta R_{xy}$ measured with voltage probes on the other side. In all cases, but most clearly in Fig. 8.8 c), the relative changes of ΔR_{xy} are very similar on opposite sides, even though the absolute values are different.

This behaviour makes it very unlikely, that the modification of the Hall resistance is caused by device details on either side, such as an asymmetry between Hall probes, which could cause a pick-up of longitudinal resistance and, hence, a superposition of SdH-oscillations on the Hall resistance. While it is unclear why such an effect should be enhanced by application of a gate voltage, it seems inconceivable how it could lead to the same, strongly non-

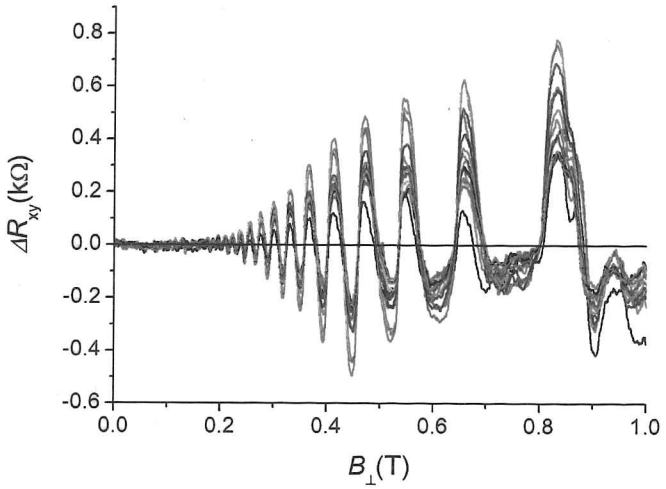

Figure 8.7: Deviation of Hall resistance $\Delta R_{xy} = R_{xy} - R_{xy}(V_g = 0)$ at various gate voltages ($V_g = (-0.143) - (-0.13)$ V) in device A77a in the measurement configuration $I_+ - I_-/V_+ - V_- = I_1 - I_2/V_2 - V_4$.

monotonic, V_g-dependence (with opposite sign) on both sides of the gate.

It seems more likely that the observation is related to transport under the gate itself, which is common to both sides. Additional support to this idea comes from the comparison of gate voltage dependence of ΔR_{xy} with the magnetically induced resistance oscillations discussed in Chapt. 7.

This is shown in Fig. 8.9, where the resistance oscillations are plotted in the same graph as ΔR_{xy} for device C67b. A clear connection between the two seemingly independent quantities is observed. At the positions of the two strong peaks in longitudinal resistance, ΔR_{xy} shows rather sharp dips and a weaker one at the position of a third, less pronounced peak. Device A77a, which shows a smoother V_g-dependence of ΔR (see Fig. 8.8 a) and b)), also did not show any strong magnetically induced resistance oscillations.

8.2.3 T-Dependence

The temperature dependence of the modified Hall resistance is summarised in Fig. 8.10. Panel a) shows the measured Hall resistance at $V_g = 0$ and

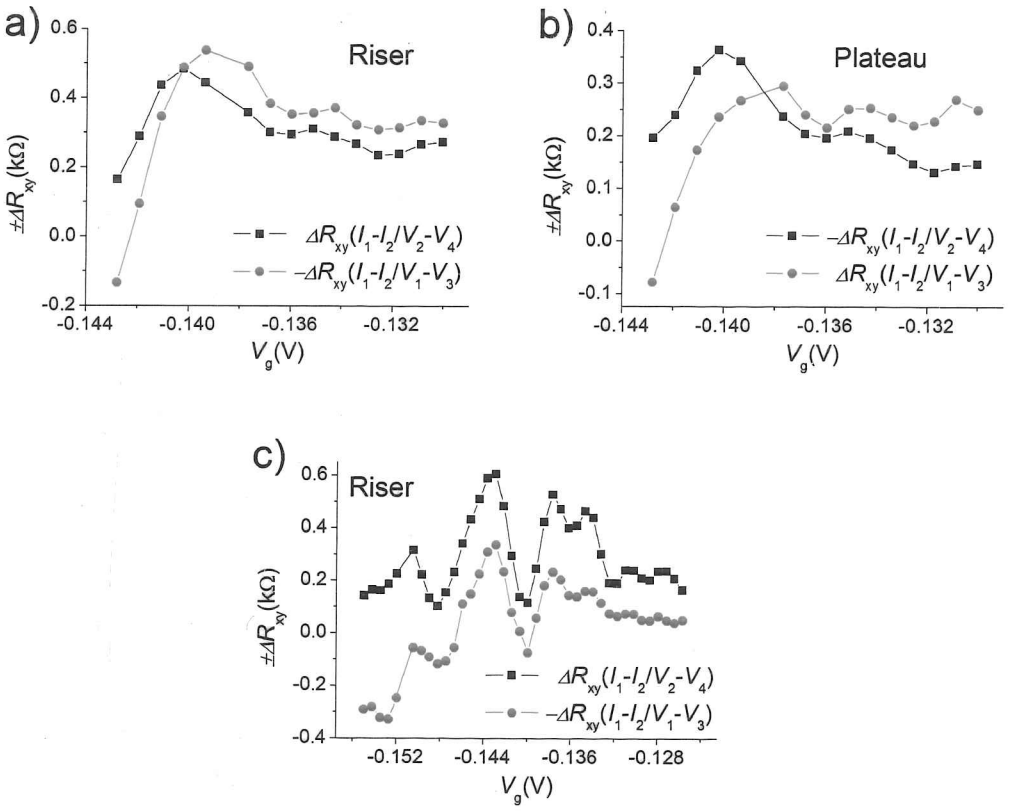

Figure 8.8: Comparison of deviation of Hall resistance $\Delta R_{\mathrm{xy}} = R_{\mathrm{xy}} - R_{\mathrm{xy}}(V_{\mathrm{g}} = 0)$ as a function of gate voltage at fixed magnetic field for two different configurations of current and voltage probes. Three different instances are shown, in each case, the sign of ΔR_{xy} has been changed for one of the two measurements for clarity. In all cases, a clear correlation between the ΔR_{xy} measured on opposite sides of the gate is observed.

a) Device A77a at $B_{\perp} \approx 0.47\,\mathrm{T}$ (riser between $\nu = 14$ and $\nu = 12$). b) Device A77a at $B_{\perp} \approx 0.51\,\mathrm{T}$ (plateau at $\nu = 12$). c) Device C67b at $B_{\perp} \approx 0.434\,\mathrm{T}$ (riser between $\nu = 8$ and $\nu = 6$)

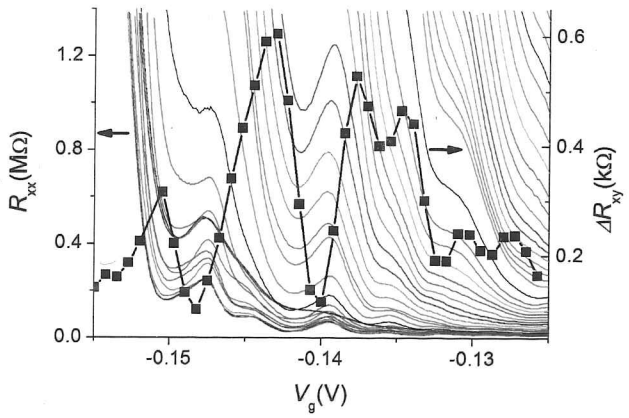

Figure 8.9: Comparison of deviation of Hall resistance $\Delta R_{xy} = R_{xy} - R_{xy}(V_g = 0)$ for device C67b compared to magnetic field induced resistance oscillations (see Chapt. 7). Minima in ΔR_{xy} seem to coincide with maxima of the resistance oscillations.

$V_g = 0.143\,V$ at two different temperatures T=0.3 K and T=1.1 K. At base temperature, a very clear deviation of R_{xy} is observed between the two gate voltages. At T=1.1 K (offset by +1 kΩ), the difference has practically disappeared, but quantum Hall plateaux are still discernible at higher magnetic fields. This already suggests that the temperature dependence of the modified Hall resistance is stronger than that of the QHE itself.

Figs. 8.10 b) and c) show the temperature dependence of ΔR_{xy} at a fixed magnetic field. In b) both axes are linear. At first sight, the T-dependence looks similar to what one would expect for SdH-oscillations. However, an attempted fit of Eq. (3.1) gives a very poor agreement, with a much stronger T-dependence observed experimentally than predicted theoretically. This supports the notion that the phenomenon cannot arise from a longitudinal resistance component picked up in the supposedly transverse resistance.

Panel c) shows the same data as b), but on a $\log(\Delta R_{xy}) - 1/T$-scale. In this representation, a striking similarity with the temperature dependence of the longitudinal resistance in the high resistivity regime becomes apparent (see Chapt. 6): A strong increase of ΔR_{xy} (possibly exponential) is observed

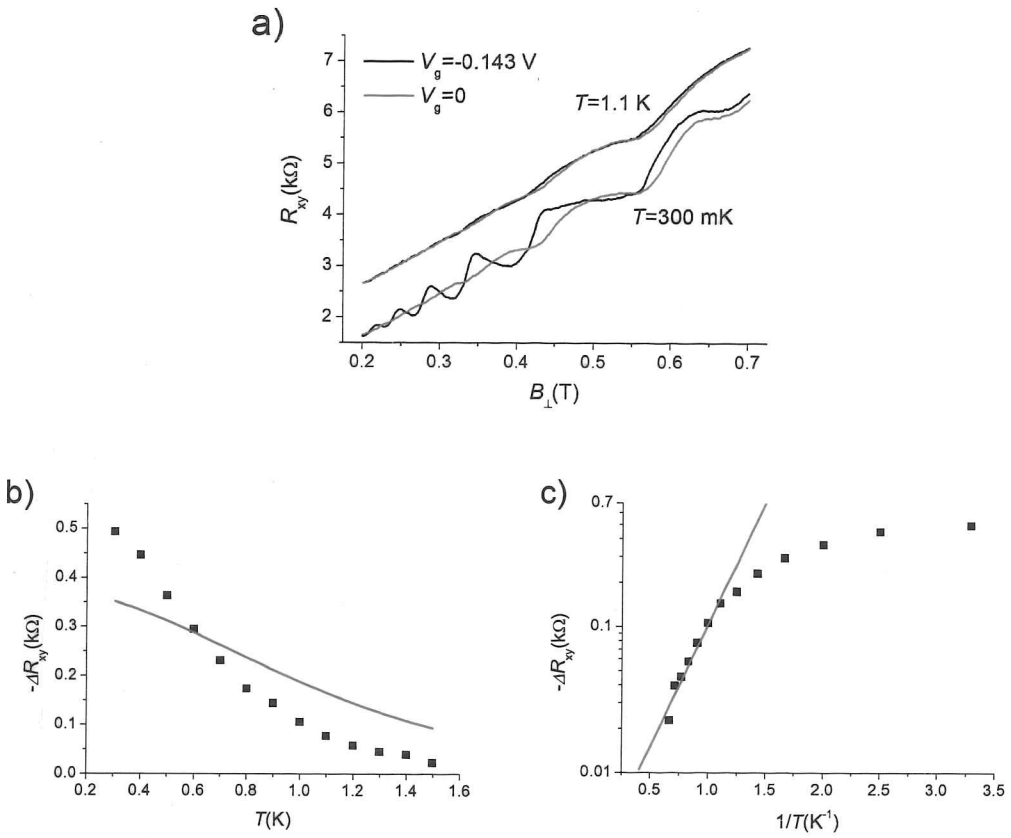

Figure 8.10: a) Comparison of Hall resistance for device C67b at $V_g = -0.143\,V$ and 0 for two temperatures. At T=300 mK, a strong modulation is observed when a gate voltage is applied. At T=1.1 K (offset by +1kΩ), the difference has practically disappeared, but quantum Hall plateaux are still discernible. b) Temperature dependence of $\Delta R_{xy} = R_{xy} - R_{xy}(V_g = 0)$ for device A77a at the plateau at $B_\perp \approx 0.45\,T$. An attempted fit of Eq. (3.1) shows very poor agreement. c) Same data as in b), but on logarithmic scale vs. 1/T. The T-dependence shows remarkable similarity to the one of the longitudinal resistivity in the strongly localised regime under the gate (see Chapt. 6).

at high temperatures, followed by a flattening and weaker T-dependence at lowest temperatures. This observation further highlights the possible connection between the modification of Hall resistance and transport in the strongly localised 2DES under the gate.

8.2.4 Discussion

Komiyama *et al.* [120] studied transport in the QHE regime in the presence of a non-equilibrium population of edge states, i.e. a difference in the chemical potential between edge states. For a configuration as used here (i.e. a Hall bar with a potential barrier), with two edge states, they predicted a correction to the Hall resistance

$$\Delta R_{xy} = \alpha\beta\gamma(h/4e^2). \tag{8.1}$$

The coefficients α, β and γ are defined as follows: $\alpha = (T_{1G} - T_{2G})/(T_{1G} + T_{2G})$, with T_{iG} the transmission probability of the i^{th} edge state across the potential barrier, is a measure of the non-equilibrium caused by the gate when the edge states travel along it. $\gamma = (T_{1V} - T_{2V})/(T_{1V} + T_{2V})$, with T_{iV} the transmission probability for the i^{th} edge state of the contact into which the edge states are injected after travelling along the gate. Hence, γ is large for non-ideal contacts where there can be a difference between the transmission of edge states, but disappears in ideal contacts. Finally, $\beta = \exp(-L/l)$, with L the length between the gate and the voltage probes and l the equilibration length between edge states.

This theory gives a possible approach for the explanation for the observation under the conditions that the transmission across the gate is not identical for all edge states, the voltage probe ohmics are not ideal and that the equilibration length between edge states is large compared to the distance between gate and voltage probe ohmics.

The equilibration length in high mobility GaAs/AlGaAs heterostructures was estimated as several hundred μm in Ref. [120], although they were investigating larger fields but also higher temperatures. In the devices used for here, the voltage probes were approximately 200 μm away from the gate, which should be well within the equilibration length. The devices were never illuminated, which could be a reason for non-ideal contacts. It is not clear in

detail, how the 2DES under the gate will influence the transmission rates for different edge states. However, it is quite likely that there will be some impact and that an interacting, or otherwise "interesting" 2DES will show a different behaviour than a simple non-interacting potential barrier.

The theory of Komiyama *et al.* does not give a full explanation of the observed modulation of the Hall resistance. In particular it does not explain the alteration of the Hall resistance between the quantum Hall plateaux. However, it does present an interesting starting point.

8.3 Common Origin?

In this Chapter, the SdH-like oscillations and the modification of Hall resistance have been discussed as completely independent phenomena. This is not necessarily the case. In fact, it is rather likely that they have a common origin, since both of them seem to be related to the quantum Hall effect, be it through Landau levels or, more specifically, edge states. For each of the observations, an idea was given for a possible explanation. It may be that one of these approaches could actually explain both observations, even though it is not immediately clear how. Another possibility is that both ideas could be combined into one theory, which is not that far fetched as both are related to the edge state picture of the quantum Hall effect in presence of a non-trivial potential barrier. In particular, they are both linked to the transmission of edge states across this barrier. Of course, at this preliminary stage, it also cannot be ruled out that there is a completely different explanation for either or both of the observations.

Chapter 9

Conclusions and Outlook

9.1 Conclusions

This thesis presents, above all, an extensive study of transport on a mesoscopic length-scale in the low density regime of 2DES at varying disorder in modulation doped GaAs/AlGaAs heterostructures. The main focus is on the various aspects of magnetoresistance and temperature dependence of transport.

While a better understanding of transport on a small length-scale in 2D, which had been surprisingly neglected in high mobility systems, would have been a valid incentive by itself, the primary motivation for this work was to study the influence of short-range disorder on 2DES while avoiding the impact of long-range charge inhomogeneities that occur at low electron densities on a macroscopic length-scale.

Chapter 4 introduces a technique for measuring the electron density in mesoscopic electron systems. It does not present much new physical insight, but is a prerequisite for a useful analysis of many of the other experiments.

Chapter 8 describes two interesting observations that are closely related to the quantum Hall effect in the high density 2DEG on either side of the gate that defines the mesoscopic 2DES. At present, it is not entirely understood to what extent their origin is linked to the localised 2DES.

The main results are discussed in Chapters 5, 6 and 7. Each of them presents a fundamentally new observation, which has not been previously reported and was made possible due to the new approach used in experiments carried out for this thesis.

Chapter 5 focuses on the low field magnetoresistance and finds evidence, that the average hopping distance of charge carriers equals the average electron-electron separation. It also presents an universality and quantisation of the magnetoresistance prefactor.

Chapter 6 presents, perhaps, the most far reaching observation: The sudden breakdown of the insulating transport behaviour below a certain temperature seems to contradict what was assumed to be known about the (putatively) strongly localised regime of 2DES and even raises questions regarding its supposedly insulating ground state.

Finally, chapter 7 shows a strongly enhanced resistivity at certain densities when a strong perpendicular magnetic field is applied. While the origin of these resistance oscillations is not very well understood, it is certainly an exciting observation that warrants further investigations.

For all observations, possible scenarios were discussed, with the focus on interaction effects and a possible formation of an electron (quantum) solid, which could nicely explain many of the results. However, due to the complexity of the system, I would like to point out that it is absolutely possible, that completely different interpretation might turn out to be true.

Irrespective of the interpretation, I believe that the results presented in this thesis represent a significant contribution to the understanding of the nature of transport and localisation in presence of disorder and electron-electron interactions in two-dimensional electron systems.

9.2 Outlook

The results in this thesis were achieved entirely through transport measurements. There are still a few interesting further transport experiments that could be done, as discussed in Sect. 9.2.1 with some preliminary results. However, it seems likely that for really new further insight, one will have to move

on to different approaches. A few suggestions are given in Sect. 9.2.2.

9.2.1 Further Transport Experiments

There are some very simple extensions to the measurements already done. One possibility would be a systematic investigation of the size of 2DES at which the interesting observations occur. On one hand, it is clear that they are absent in macroscopic devices with dimensions of hundreds of microns, but appear at dimensions of a few microns. However, intermediate sizes have not been investigated, which could reveal information about the length-scales involved. On the other hand, at even smaller dimensions, a transition to direct tunnelling across the gate is expected, which should show a qualitatively different behaviour. Devices with gate length as small as 100 nm have been fabricated during this PhD, but have not been measured.

It would also be interesting to see if the metallic and saturated behaviour reported in Chapt. 6 persist to lower temperatures than those accessible in our cryogenic systems. Therefore, experiments in an ultra-cold systems would be desirable. Of course, one can never rigorously prove the existence of a metallic ground state by just measuring the temperature dependence of resistance to very low temperature, since an insulating behaviour could always set in at even lower T. Nevertheless, experiments reaching significantly less that 60 mK could shed further light on the question if the drop in resistance is just a phenomenon appearing at an intermediate temperature range, or not.

Furthermore, application of an in-plane magnetic field could reveal useful information. It has been shown that a perpendicular field can suppress the metallic phase (Chapt. 6) or induce resistance oscillations (Chapt. 7). Trying to reproduce these observations with an in-plane field could give insight on the origin of these observations, e.g. if they are orbital, interference- or spin-effects.

Hole Systems

Some preliminary experiments were done with hole gases. Holes have a significantly larger effective mass in GaAs than electrons ($m_{\mathrm{h}}^*/m_{\mathrm{e}}^* \approx 7$). This means that at the same carrier density, the interaction parameter r_{s} is much larger for holes than for electrons, and interaction effects are expected to be stronger

in hole systems. However, the main motivation for trying to reproduce the experiments from the electron systems with hole systems, was the possible universality in r_s of the peak positions and periodicity of the oscillations discussed in Sect. 7.2. A comparison with hole systems could give further insight if there exists an universality in r_s or n_s.

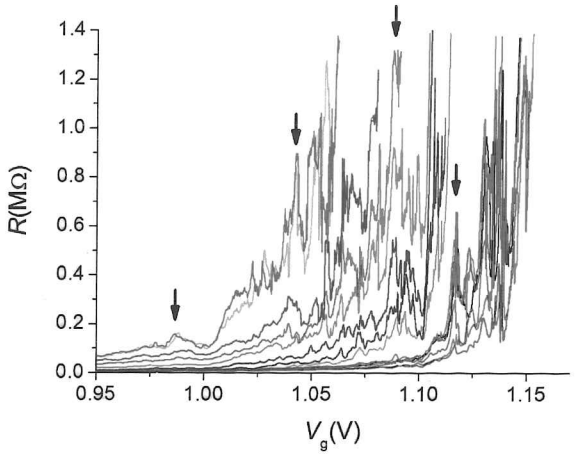

Figure 9.1: Resistance as a function of gate voltage at stepwise increasing perpendicular magnetic field ($B_\perp = 0 - 12\,\mathrm{T}$, $\Delta B_\perp = 1\,\mathrm{T}$) in a beryllium doped hole gas. Some indications of magnetically induced resistance peaks are observed (arrows), but a clear observation is hindered by the poor stability. T=300 mK, device A55a.

Devices of identical geometry to those in electron systems were fabricated for beryllium δ-doped heterostructers with spacers δ_{sp}=20, 40 and 60 nm. However, they turned out to be very unstable, with very strong switching events as the gate voltage was swept, an example is shown in Fig. 9.1. The switching is most likely caused by rearrangements of charges in the dopant layer, possibly enhanced because the stable DX-centres cannot form in p-type devices. When applying a strong perpendicular magnetic field, some signs of peak formation were observed, marked by arrows in Fig. 9.1, which did not move with changing magnetic field. However, the overall instability of the device made it difficult to unambiguously identify the peaks. Furthermore, a density measurement with

the method described in Chapt. 4 was not possible, which is not surprising as the large effective mass reduces the Landau level spacing and makes it harder to resolve the quantum Hall plateaux. Therefore, a determination of positions in n_s of these peaks was not possible.

Some devices with Si δ-doped hole systems, where a (311) oriented substrate was used in growth, were fabricated as well,but they were even less stable, and most likely overdoped. It would be interesting to see if silicon or carbon doped hole systems could be optimised to a satisfactory stability, but it was decided not to pursue this direction for the moment.

Biased Cooldowns

As mentioned briefly in Sects. 2.2.2 and 3.3.3, the remaining electrons in the dopant layer may play an important role in the experiments performed for this thesis. Correlation effects between electrons in the dopant layers have been predicted to reduce the long range disorder [25], which could be important for reducing the effect of long-range inhomogeneities of the 2DES. Monte Carlo calculations even predicted the formation of a Wigner-like crystal of the electrons in the doping layer although without long-range order [121, 122]. These calculations did not take DX-centres into account, which would reduce the probability of a long-range order because of their high freeze-out temperature. Nevertheless, if some kind of ordering was present in the dopant layer, this could have a strong impact in the 2DES. In particular it could lead to commensurability effects with a possible electron solid in the 2DES. In Sect. 7.4.2, this has been suggested as one possible explanation of the resistance oscillations discussed in Chapt. 7.

A way of investigating the importance of the remaining electrons in the dopant layer would be to change the filling factor $\eta = 1 - n_{d^+}/n_\delta$, which should change the degree of suppression of the long-range disorder as well as the length-scale of a putative ordering. It has been demonstrated that application of a gate bias on the topgate during the cooldown can change the filling factor with a negative bias reducing η [79].

An attempt to reproduce these experiments for mesoscopic device dimensions was done with device A78f, shown in Fig. 9.2 (unbiased cooldowns of this device are shown in Fig. 7.2). A bias $V_B = -1\,V$ worked without problems,

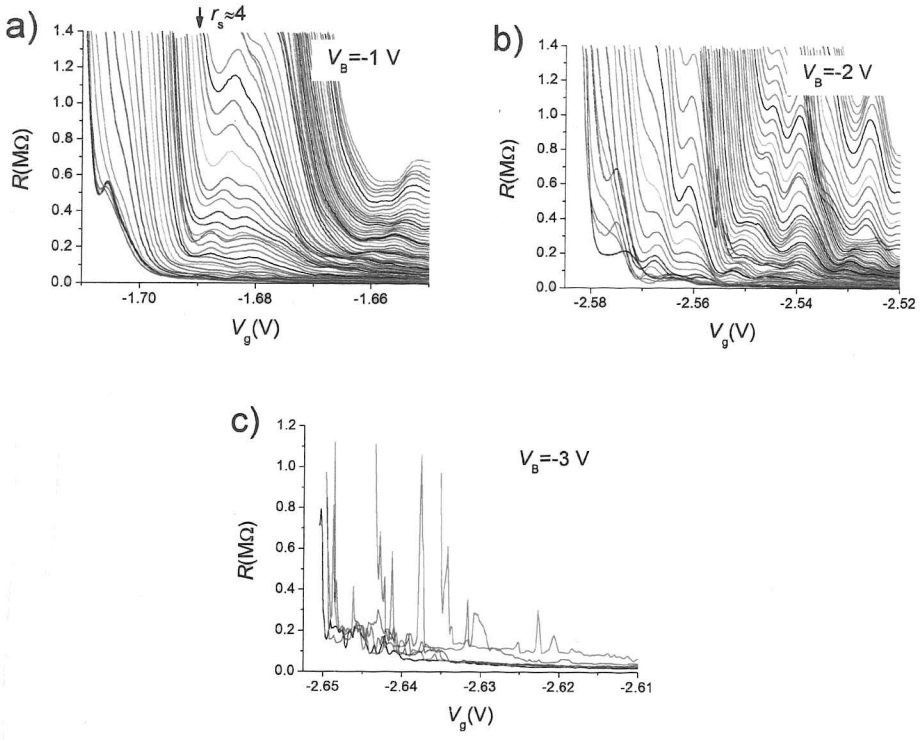

Figure 9.2: Biased cooldown experiments with device A78f.

a) and b): Resistance oscillations in stepwise increasing perpendicular magnetic field. For cooldown bias $V_B = -1\,V$, $r_s = 4$ is indicated by an arrow. For $V_B \leq -2\,V$, a reliable density measurement was not possible. c) Reproducibility gate sweeps at constant field $B_\perp = 0$. Strong switching and an overall drift is observed, making any reasonable measurement impossible.

but only lead to a small change of the filling factor to $\eta \approx 0.37$, from $\eta \approx 0.42$ at $V_B = 0$. A peak at approximately $r_s = 4$ was still observed. At $V_B = -2\,V$ ($\eta \approx 0.32$), some instabilities were observed (two shifts can be seen in Fig. 9.2 b)) and an electron density measurement failed, making a comparison of peak positions impossible. At $V_B \leq -3\,V$, the device became completely unstable, as shown in Fig. 9.2 c).

It is not entirely clear what caused these problems, but they made a useful analysis of varying η impossible. It was decides not to continue these biased

cooldown experiments.

9.2.2 Different Experimental Approaches

Compressibility Measurements

The compressibility, defined as $K^{-1} = n_s^2 \partial\mu/\partial n_s$, gives direct information about the density of states at the chemical potential μ. It would be very interesting to investigate the compressibility in mesoscopic devices as a function of electron density and compare it between metallic and saturated phase as discussed in Chapt. 6 or between peaks and troughs discussed in Chapt. 7.

For such an investigation, a design would have to be found, where transport over mesoscopic dimensions and the compressibility could be measured in the same device. A possibility for measuring the local compressibility in a small area is to use the sensitivity of a single-electron transistor (SET) to potential changes in its vicinity, a technique which has been used previously [123, 124]. Since the SET would have to be fabricated on the surface of the wafer, the mesoscopic 2DES could not be defined with a topgate anymore. A possible way around this problem would be to use a patterned backgate instead of the topgate. This would lead to a device equivalent to the ones used in the experiments described in this thesis, but with the surface left free for a SET.

Imaging

The sensitivity of SETs to variations in the electrical potential has also been applied for imaging, where an SET was fabricated on the tip of a scanning probe microscope (SPM) and used as an extremely sensitive electrometer [125–127]. These experiments focused on the localised states in the quantum Hall regime, where some evidence of a charge ordering was reported. It suggests itself that similar imaging could reveal important information about the nature of localisation in our devices. Again, it would be particularly interesting to see if there is a qualitative difference in the charge arrangement between different behaviours of the temperature dependence of resistance (Chapt. 6) or the magnetoresistance (Chapt. 7). In particular, one might be able to determine if these changes are caused by a change of behaviour of the whole 2DES or in

some dominating path between the leads.

The sample design would have to be similar to the one discussed above for the compressibility measurements, since those scanning probe measurement could, of course, not be done through a topgate. A patterned backgate would remove this problem.

A quite different approach would be to apply a technique developed by Topinka *et al.* [128, 129], who measured the conductance of a quantum point contact (QPC) while raster scanning a negatively charged SPM tip in the leads to the QPC. As briefly discussed in Sect. 8.1.4, a strongly interacting potential barrier might be much more sensitive to modification at the Fermi energy in the leads, which could be caused by the charged SPM tip. It would, therefore, be interesting to see if the resistivity of the mesoscopic 2DES is sensitive to a SPM tip in the leads, and if so, how the sensitivity depends on the electron density.

An advantage of this experiment is that it could be done with topgated devices used in this thesis, since, here, the scanning happens in the ungated part of the device. Therefore, the challenging task of fabricating patterned backgated devices could be avoided.

Noise Measurements

Shot noise arises from the quantisation of charge which results in small current fluctuations on a short time-scale. Measurements of this noise can reveal information that is not available through simple conductance measurements [130]. It can determine the charge and statistics of the (quasi-)particles relevant for transport and is generally more sensitive to electron-electron interactions than the average conductance.

In the mesoscopic 2DES used in this thesis, noise measurements could reveal information on the nature of the charge carriers, which is of particular interest in view of the picture of quantum diffusion of defects introduced in Sect. 6.2.1. On the other hand, a possible correlated hopping of electrons would also be expected to have a strong impact on the noise. While the SET measurements proposed above require very low operating temperatures, noise experiments could also be done at relatively high temperatures $T \gtrsim 1\,\mathrm{K}$, which would

allow an investigation of the transition from activated to saturated/metallic transport observed around 1 K (Chapt. 6). Initial experiments could be done on a device design identical to the ones already used.

Thermal Conductivity

Another property that might reveal information about the 2DES additional to simple transport measurements is the thermal conductance. Topgated devices could be used for this, however some additional features would have to be fabricated. One could start from a design similar to the one used previously, but add a heater on one side of the gate and some kind of "thermometer" on both sides. The heater could, for example, be a relatively high resistance metal evaporated in a suitable pattern on the surface, which would be insulated from the 2DES. Application of a relatively large current would heat up the side of the device where the heater is placed. To measure the local temperature one could use QPCs, which have a strongly temperature dependent conductance in the regime near pinch-off and could be calibrated against the cryostat temperature. The thermal conductance could then be determined as a function of gate voltage from the measured temperature gradient between the two sides of the gate.

Appendix A

Sample List

The following table contains a list of devices used in this thesis and their relevant properties.

- Wafer: The first letter in the wafer number determines the growth chamber.
- δ_{sp}: Spacer width between doping layer and 2DES.
- d_g: Total depth of the 2DES from the surface.
- n_s: Electron density as cooled down in the dark, determined in wafer assessment on macroscopic devices.
- μ: Mobility as cooled down in the dark, determined in wafer assessment on macroscopic devices.
- n_δ: Doping concentration.
- $L \times W$: Gate dimensions.

Device	Wafer	δ_{sp} (nm)	d_g (nm)	n_s (cm^{-2})	μ (cm^2/Vs)	n_δ (cm^{-2})	$L \times W$ ($\mu m \times \mu m$)	Description
A07a	A2407	20	120	2.9×10^{11}	0.6×10^{6}	2.5×10^{12}	2×8	Si δ-doped 2D electron system Fabricated by Dr. Arindam Ghosh
A07b	A2407	20	120	2.9×10^{11}	0.6×10^{6}	2.5×10^{12}	3×8	Si δ-doped 2D electron system Fabricated by Dr. Arindam Ghosh
A55a	A2855	20	120	2.35×10^{11}	0.23×10^{6}	2.5×10^{12}	4×8	Beryllium δ-doped 2D hole system
A77a	A2677	40	90	1.7×10^{11}	0.97×10^{6}	-	3×8	Si bulk-doped 2D electron system $n_\delta=2\times10^{18}cm^{-3}$ over a range of 40 nm
A77b	A2677	40	90	1.7×10^{11}	0.97×10^{6}	-	3×8	Si bulk-doped 2D electron system $n_\delta=2\times10^{18}cm^{-3}$ over a range of 40 nm
A77Lc	A2677	40	90	1.7×10^{11}	0.97×10^{6}	-	900×100	Si bulk-doped 2D electron system $n_\delta=2\times10^{18}cm^{-3}$ over a range of 40 nm
A78d	A2678	40	290	2.1×10^{11}	1.8×10^{6}	2.5×10^{12}	1.5, 1, 0.5 ×8	Si δ-doped 2D electron system Fabricated by Dr. Arindam Ghosh
A78e	A2678	40	290	2.1×10^{11}	1.8×10^{6}	2.5×10^{12}	2×8	Si δ-doped 2D electron system Fabricated by Dr. Arindam Ghosh
A78f	A2678	40	290	2.1×10^{11}	1.8×10^{6}	2.5×10^{12}	4×8	Si δ-doped 2D electron system
C67a	C2367	60	290	1.03×10^{11}	1.2×10^{6}	0.7×10^{12}	2, 1, 0.5 ×8	Si δ-doped 2D electron system
C67b	C2367	60	290	1.03×10^{11}	1.2×10^{6}	0.7×10^{12}	3×8	Si δ-doped 2D electron system
T46a	T546	80	300	0.8×10^{11}	0.9×10^{6}	1.9×10^{12}	3×8	Si δ-doped 2D electron system Fabricated by Dr. Arindam Ghosh

Appendix B

Abbreviations

2D Two dimensions/ two-dimensional
2DEG Two-dimensional electron gas
2DES Two-dimensional electron system
2DHG Two-dimensional hole gas
AL Andreev and Lifshitz (Ref. [49])
CBT Coulomb blockade thermometer
DOS Density of states
ES Electron solid
FL Fermi Liquid
FN-QMC Fixed node quantum Monte Carlo
FQHE Fractional quantum Hall effect
GWF Guiding wave function
IQHE Integer quantum Hall effect
LL Landau level
MBE Molecular beam epitaxy
MIT Metal-insulator transition
MOSFET Metaloxidesemiconductor field-effect transistor
MSD Mean square deviation
NNH Nearest-neighbour hopping
QMC Quantum Monte Carlo
QPC Quantum point contact
QS Quantum solid

SB Subband
SdH Shubnikov-de Haas
SET Single-electron transistor
SPM Scanning probe microscope
TK Tripathi and Kenneth (Refs. [97, 99])
VRH Variable-range hopping
WC Wigner crystal
WG Wigner glass

Bibliography

[1] Anderson, P. W. Absence of diffusion in certain random lattices. *Phys. Rev.* **109**(5), 1492 (1958).

[2] Mott, N. Electrons in disordered structures. *Adv. Phys.* **16**, 49–144 (1967).

[3] Mott, N. F. Conduction in glasses containing transition metal ions. *J. Non-cryst. Solids* **1**, 1–17 (1968).

[4] Abrahams, E., Anderson, P. W., Licciardello, D. C., and Ramakrishnan, T. V. Scaling theory of localization: Absence of quantum diffusion in two dimensions. *Phys. Rev. Lett.* **42**(10), 673 (1979).

[5] Mott, N., Pepper, N., Pollitt, S., Wallis, R. H., and Adkins, C. J. The Anderson transition. *Proc. R. Soc. Lond. A.* **345**, 169 (1975).

[6] Timp, G., Fowler, A. B., Hartstein, A., and Butcher, P. N. Absence of a Coulomb gap in a two-dimensional impurity band. *Phys. Rev. B* **33**(2), 1499 (1986).

[7] Tremblay, F., Pepper, M., Newbury, R., Ritchie, D. A., Peacock, D. C., Frost, J. E. F., Jones, G. A. C., and Hill, G. Hopping in a low-mobility GaAs-AlGaAs heterojunction in the limit of low electronic concentrations. *J. Phys.: Condens. Matter* **2**(35), 7367 (1990).

[8] Efros, A. L. and Shklovskii, B. I. Coulomb gap and low temperature conductivity of disordered systems. *J. Phys. C: Solid State Phys.* **8**(4), L49 (1975).

[9] Mason, W., Kravchenko, S. V., Bowker, G. E., and Furneaux, J. E. Experimental evidence for a Coulomb gap in two dimensions. *Phys. Rev. B* **52**(11), 7857 (1995).

[10] Khondaker, S. I., Shlimak, I. S., Nicholls, J. T., Pepper, M., and Ritchie, D. A. Two-dimensional hopping conductivity in a delta-doped GaAs/$Al_xGa_{1-x}As$ heterostructure. *Phys. Rev. B* **59**(7), 4580 (1999).

[11] Wigner, E. On the interaction of electrons in metals. *Phys. Rev.* **46**(11), 1002 (1934).

[12] Tanatar, B. and Ceperley, D. M. Ground state of the two-dimensional electron gas. *Phys. Rev. B* **39**(8), 5005 (1989).

[13] Goldman, V. J., Santos, M., Shayegan, M., and Cunningham, J. E. Evidence for two-dimentional quantum Wigner crystal. *Phys. Rev. Lett.* **65**(17), 2189 (1990).

[14] Jiang, H. W., Willett, R. L., Stormer, H. L., Tsui, D. C., Pfeiffer, L. N., and West, K. W. Quantum liquid versus electron solid around ν =1/5 landau-level filling. *Phys. Rev. Lett.* **65**(5), 633 (1990).

[15] Yoon, J., Li, C. C., Shahar, D., Tsui, D. C., and Shayegan, M. Wigner crystallization and metal-insulator transition of two-dimensional holes in GaAs at B=0. *Phys. Rev. Lett.* **82**(8), 1744 (1999).

[16] Manoharan, H. C., Suen, Y. W., Santos, M. B., and Shayegan, M. Evidence for a bilayer quantum Wigner solid. *Phys. Rev. Lett.* **77**(9), 1813 (1996).

[17] Ye, Q.-Y., Shklovskii, B. I., Zrenner, A., Koch, F., and Ploog, K. Hopping transport in delta -doping layers in GaAs. *Phys. Rev. B* **41**(12), 8477 (1990).

[18] Chen, Y., Lewis, R. M., Engel, L. W., Tsui, D. C., Ye, P. D., Pfeiffer, L. N., and West, K. W. Microwave resonance of the 2D Wigner crystal around integer Landau fillings. *Phys. Rev. Lett.* **91**(1), 016801 (2003).

[19] Abrahams, E., Kravchenko, S. V., and Sarachik, M. P. Metallic behavior and related phenomena in two dimensions. *Rev. Mod. Phys.* **73**(2), 251 (2001).

[20] Chui, S. T. and Tanatar, B. Impurity effect on the two-dimensional-electron fluid-solid transition in zero field. *Phys. Rev. Lett.* **74**(3), 458 (1995).

[21] Ando, T., Fowler, A. B., and Stern, F. Electronic properties of two-dimensional systems. *Rev. Mod. Phys.* **54**(2), 437 (1982).

[22] Arnold, E. Disorder-induced carrier localization in silicon surface inversion layers. *Appl. Phys. Lett.* **25**(12), 705–707 (1974).

[23] Jiang, C., Tsui, D. C., and Weimann, G. Threshold transport of high-mobility two-dimensional electron gas in GaAs/AlGaAs heterostructures. *Appl. Phys. Lett.* **53**(16), 1533–1535 (1988).

[24] Das Sarma, S., Lilly, M. P., Hwang, E. H., Pfeiffer, L. N., West, K. W., and Reno, J. L. Two-dimensional metal-insulator transition as a percolation transition in a high-mobility electron system. *Phys. Rev. Lett.* **94**(13), 136401 (2005).

[25] Efros, A. L. Density of states of 2D electron gas and width of the plateau of IQHE. *Solid State Comm.* **65**, 1281–1284 (1988).

[26] Finkelstein, G., Glicofridis, P. I., Ashoori, R. C., and Shayegan, M. Topographic mapping of the quantum Hall liquid using a few-electron bubble. *Science* **289**, 90–94 (2000).

[27] Chakraborty, S., Maasilta, I. J., Tessmer, S. H., and Melloch, M. R. Imaging a two-dimensional electron system with a scanning charged probe. *Phys. Rev. B* **69**(7), 073308 (2004).

[28] Ashcroft, N. W. and Mermin, N. D. *Solid State Physics.* Thomson Brooks/Cole, (1976).

[29] Adachi, S. GaAs, AlAs, and $Al_xGa_{1-x}As$ material parameters for use in research and device applications. *J. Appl. Phys.* **58**(3), R1–R29 (1985).

[30] Chadi, D. J. and Chang, K. J. Theory of the atomic and electronic structure of DX centers in GaAs and $Al_xGa_{1-x}As$ alloys. *Phys. Rev. Lett.* **61**(7), 873 (1988).

[31] Chadi, D. J. and Chang, K. J. Energetics of DX-center formation in GaAs and $Al_xGa_{1-x}As$ alloys. *Phys. Rev. B* **39**(14), 10063 (1989).

[32] Mäkinen, J., Laine, T., Saarinen, K., Hautojrvi, P., Corbel, C., Airaksinen, V. M., and Gibart, P. Observation of a vacancy at the DX center in Si- and Sn-doped AlGaAs. *Phys. Rev. Lett.* **71**(19), 3154 (1993).

[33] Buks, E., Heiblum, M., Levinson, Y., and Shtrikman, H. Scattering of a two-dimensional electron gas by a correlated system of ionized donors. *Semicond. Sci. Technol.* **9**(11), 2031 (1994).

[34] Ando, T. Self-consistent results for a $GaAs/Al_xGa_{1-x}As$ heterojunction. II. Low temperature mobility. *J. Phys. Soc. Jpn.* **51**, 3900–3907 (1982).

[35] Walukiewicz, W., Ruda, H. E., Lagowski, J., and Gatos, H. C. Electron mobility in modulation-doped heterostructures. *Phys. Rev. B* **30**(8), 4571 (1984).

[36] Efros, A. L., Pikus, F. G., and Samsonidze, G. G. Maximum low-temperature mobility of two-dimensional electrons in heterojunctions with a thick spacer layer. *Phys. Rev. B* **41**(12), 8295 (1990).

[37] Lin, B. J. F., Tsui, D. C., Paalanen, M. A., and Gossard, A. C. Mobility of the two-dimensional electron gas in GaAs-$Al_xGa_{1-x}As$ heterostructures. *Appl. Phys. Lett.* **45**(6), 695–697 (1984).

[38] Hirakawa, K. and Sakaki, H. Mobility of the two-dimensional electron gas at selectively doped n-type $Al_xGa_{1-x}As$/GaAs heterojunctions with controlled electron concentrations. *Phys. Rev. B* **33**(12), 8291 (1986).

[39] Efros, A. L., Pikus, F. G., and Burnett, V. G. Density of states of a two-dimensional electron gas in a long-range random potential. *Phys. Rev. B* **47**(4), 2233 (1993).

[40] Lee, P. A. and Ramakrishnan, T. V. Disordered electronic systems. *Rev. Mod. Phys.* **57**(2), 287 (1985).

[41] Mak, C. H., Egger, R., and Weber-Gottschick, H. Multilevel blocking approach to the fermion sign problem in path-integral Monte Carlo simulations. *Phys. Rev. Lett.* **81**(21), 4533 (1998).

[42] Waintal, X. On the quantum melting of the two-dimensional Wigner crystal. *Phys. Rev. B* **73**(7), 075417 (2006).

[43] Lozovik, Y. E. and Yudson, V. I. Crystallization of a two-dimensional electron gas in a magnetic field. *JETP Lett.* **22**, 11 (1975).

[44] Laughlin, R. B. Anomalous quantum Hall effect: An incompressible quantum fluid with fractionally charged excitations. *Phys. Rev. Lett.* **50**(18), 1395 (1983).

[45] Levesque, D., Weis, J. J., and MacDonald, A. H. Crystallization of the incompressible quantum-fluid state of a two-dimensional electron gas in a strong magnetic field. *Phys. Rev. B* **30**(2), 1056 (1984).

[46] Buhmann, H., Joss, W., von Klitzing, K., Kukushkin, I. V., Martinez, G., Plaut, A. S., Ploog, K., and Timofeev, V. B. Magneto-optical evidence for fractional quantum Hall states down to filling factor 1/9. *Phys. Rev. Lett.* **65**(8), 1056 (1990).

[47] Katomeris, G., Selva, F., and Pichard, J.-L. Andreev-Lifshitz supersolid revisited for a few electrons on a square lattice. I. *Eur. Phys. J. B* **31**, 401–412 (2003).

[48] Németh, Z. A. and Pichard, J.-L. Andreev-Lifshitz supersolid revisited for a few electrons on a square lattice. II. *Eur. Phys. J. B* **33**, 87–101 (2003).

[49] Andreev, A. F. and Lifshitz, I. M. Quantum theory of defects in crystals. *Sov. Phys. JETP* **29**, 1107 (1969).

[50] Falakshahi, H. and Waintal, X. Hybrid phase at the quantum melting of the Wigner crystal. *Phys. Rev. Lett.* **94**(4), 046801 (2005).

[51] Spivak, B. Phase separation in the two-dimensional electron liquid in MOSFET's. *Phys. Rev. B* **67**(12), 125205 (2003).

[52] Spivak, B. and Kivelson, S. A. Phases intermediate between a two-dimensional electron liquid and Wigner crystal. *Phys. Rev. B* **70**(15), 155114 (2004).

[53] Koulakov, A. A., Fogler, M. M., and Shklovskii, B. I. Charge density wave in two-dimensional electron liquid in weak magnetic field. *Phys. Rev. Lett.* **76**(3), 499 (1996).

[54] Jamei, R., Kivelson, S., and Spivak, B. Universal aspects of Coulomb-frustrated phase separation. *Phys. Rev. Lett.* **94**(5), 056805 (2005).

[55] Ortix, C., Lorenzana, J., Beccaria, M., and Di Castro, C. Screening effects in Coulomb-frustrated phase separation. *Phys. Rev. B* **75**(19), 195107 (2007).

[56] Noh, H., Lilly, M. P., Tsui, D. C., Simmons, J. A., Pfeiffer, L. N., and West, K. W. Linear temperature dependence of conductivity in the apparent insulating regime of dilute two-dimensional holes in GaAs. *Phys. Rev. B* **68**(24), 241308 (2003).

[57] Csathy, G. A., Tsui, D. C., Pfeiffer, L. N., and West, K. W. Possible observation of phase coexistence of the $\nu = 1/3$ fractional quantum Hall liquid and a solid. *Phys. Rev. Lett.* **92**(25), 256804 (2004).

[58] Tsui, D. C., Stormer, H. L., and Gossard, A. C. Two-dimensional magnetotransport in the extreme quantum limit. *Phys. Rev. Lett.* **48**(22), 1559 (1982).

[59] Stormer, H. L., Tsui, D. C., and Gossard, A. C. The fractional quantum Hall effect. *Rev. Mod. Phys.* **71**(2), S298 (1999).

[60] Klitzing, K. v., Dorda, G., and Pepper, M. New method for high-accuracy determination of the fine-structure constant based on quantized Hall resistance. *Phys. Rev. Lett.* **45**(6), 494 (1980).

[61] von Klitzing, K. The quantized Hall effect. *Rev. Mod. Phys.* **58**(3), 519 (1986).

[62] Eguiluz, A. G., Maradudin, A. A., and Elliott, R. J. Two-dimensional Wigner lattice in a magnetic field and in the presence of a random array of pinning centers. *Phys. Rev. B* **27**(8), 4933 (1983).

[63] Ruzin, I. M., Marianer, S., and Shklovskii, B. I. Pinning of a two-dimensional Wigner crystal by charged impurities. *Phys. Rev. B* **46**(7), 3999 (1992).

[64] Chui, S. T. A quantitative study of pinning of a 2D electron crystal in heterojunctions. *J. Phys.: Condens. Matter* **5**(33), L405–L408 (1993).

[65] Ferconi, M. and Vignale, G. Theory of the pinning gap in the phonon spectrum of a disordered Wigner crystal. *Phys. Rev. B* **48**(4), 2831 (1993).

[66] Aleiner, I. L. and Ruzin, I. M. Density of states of localized phonons in a pinned Wigner crystal. *Phys. Rev. Lett.* **72**(7), 1056 (1994).

[67] Chitra, R., Giamarchi, T., and Le Doussal, P. Pinned Wigner crystals. *Phys. Rev. B* **65**(3), 035312 (2001).

[68] Chitra, R. and Giamarchi, T. Zero field Wigner crystal. *Eur. Phys. J. B* **44**(4), 455–467 (2005).

[69] Fukuyama, H. and Lee, P. A. Pinning and conductivity of two-dimensional charge-density waves in magnetic fields. *Phys. Rev. B* **18**(11), 6245 (1978).

[70] Strandburg, K. J. Two-dimensional melting. *Rev. Mod. Phys.* **60**(1), 161 (1988).

[71] Gann, R. C., Chakravarty, S., and Chester, G. V. Monte Carlo simulation of the classical two-dimensional one-component plasma. *Phys. Rev. B* **20**(1), 326 (1979).

[72] Grimes, C. C. and Adams, G. Evidence for a liquid-to-crystal phase transition in a classical, two-dimensional sheet of electrons. *Phys. Rev. Lett.* **42**(12), 795 (1979).

[73] Ye, P. D., Engel, L. W., Tsui, D. C., Lewis, R. M., Pfeiffer, L. N., and West, K. Correlation lengths of the Wigner-crystal order in a two-dimensional electron system at high magnetic fields. *Phys. Rev. Lett.* **89**(17), 176802 (2002).

[74] Scott-Thomas, J. H. F., Field, S. B., Kastner, M. A., Smith, H. I., and Antoniadis, D. A. Conductance oscillations periodic in the density of a one-dimensional electron gas. *Phys. Rev. Lett.* **62**(5), 583 (1989).

[75] Cha, M.-C. and Fertig, H. A. Disorder-induced phase transitions in two-dimensional crystals. *Phys. Rev. Lett.* **74**(24), 4867 (1995).

[76] Thakur, J. S. and Neilson, D. Frozen electron solid in the presence of small concentrations of defects. *Phys. Rev. B* **54**(11), 7674 (1996).

[77] Shklovskii, B. I. Coulomb gap and variable range hopping in a pinned Wigner crystal. *phys. stat. sol. (c)* **1**(1), 46–50 (2004).

[78] White, G. K. and Meeson, P. J. *Experimental Techniques in Low-Temperature Physics.* Oxford Science Publications, (2002).

[79] Buks, E., Heiblum, M., and Shtrikman, H. Correlated charged donors and strong mobility enhancement in a two-dimensional electron gas. *Phys. Rev. B* **49**(20), 14790 (1994).

[80] Davies, J. H. *The Physics of Low-Dimensional Semiconductors.* Cambridge University Press, Cambridge, UK, (1998).

[81] Barnes, C. H. W. *Quantum Properties of Electron Systems in Semiconductors.* Lecture notes, University of Cambridge.

[82] Hook, J. R. and Hall, H. E. *Solid State Physics.* John Wiley and Sons, (1991).

[83] Ebert, G., Klitzing, K. v., Probst, C., and Ploog, K. Magneto-quantumtransport on GaAs-$Al_xGa_{1-x}As$ heterostructures at very low temperatures. *Solid State Comm.* **44**(2), 95–98 (1982).

[84] Chklovskii, D. B., Shklovskii, B. I., and Glazman, L. I. Electrostatics of edge channels. *Phys. Rev. B* **46**(7), 4026 (1992).

[85] Büttiker, M. Four-terminal phase-coherent conductance. *Phys. Rev. Lett.* **57**(14), 1761 (1986).

[86] Haug, R. J. Edge-state transport and its experimental consequences in high magnetic fields. *Semicond. Sci. Technol.* **8**(2), 131–153 (1993).

[87] Haug, R. J., MacDonald, A. H., Streda, P., and von Klitzing, K. Quantized multichannel magnetotransport through a barrier in two dimensions. *Phys. Rev. Lett.* **61**(24), 2797 (1988).

[88] Washburn, S., Fowler, A. B., Schmid, H., and Kern, D. Quantized Hall effect in the presence of backscattering. *Phys. Rev. Lett.* **61**(24), 2801 (1988).

[89] Shklovskii, B. I. Positive magnetoresistance in the variable-range hopping region. *Sov. Phys. Semicond.* **17**, 1311 (1983).

[90] Nguen, V. L. Two-dimensional hopping conduction in a magnetic field. *Sov. Phys. Semicond.* **18**, 207 (1984).

[91] Timp, G. and Fowler, A. B. Magnetoresistance in a two-dimensional impurity band. *Phys. Rev. B* **33**(6), 4392 (1986).

[92] Measurements partially recorded by Dr. Arindam Ghosh. All data processing and analysis done by Matthias Baenninger.

[93] Van Keuls, F. W., Mathur, H., Jiang, H. W., and Dahm, A. J. Localization scaling relation in two dimensions: Comparison with experiment. *Phys. Rev. B* **56**(20), 13263 (1997).

[94] Measurement recorded by Dr. Arindam Ghosh. All data processing and analysis done by Matthias Baenninger.

[95] Aleiner, I. L., Polyakov, D. G., and Shklovskii, B. I. Hopping transport and the quantum Hall effect. *Proc. 22nd Int. Conf. Phys. Semicond., Vancouver, 1994* **1**, 787 (1994).

[96] Müller, M. and Ioffe, L. B. Collective modes in quantum electron glasses and electron-assisted hopping. *Cond-mat* **arXiv:0711.2668v1** (2007).

[97] Tripathi, V. and Kennett, M. P. Magnetotransport in disordered delta-doped heterostructures. *Phys. Rev. B* **74**(19), 195334 (2006).

[98] Savchenko, A. K., Kuznetsov, V. V., Woolfe, A., Mace, D. R., Pepper, M., Ritchie, D. A., and Jones, G. A. C. Resonant tunneling through two impurities in disordered barriers. *Phys. Rev. B* **52**(24), R17021 (1995).

[99] Tripathi, V. and Kennett, M. P. Magnetic-field-induced Coulomb blockade in small disordered delta-doped heterostructures. *Phys. Rev. B* **76**(11), 115321 (2007).

[100] Kravchenko, S. V., Kravchenko, G. V., Furneaux, J. E., Pudalov, V. M., and D'Iorio, M. Possible metal-insulator transition at B=0 in two dimensions. *Phys. Rev. B* **50**(11), 8039 (1994).

[101] Huang, J., Xia, J. S., Tsui, D. C., Pfeiffer, L. N., and West, K. W. Disappearance of metal-like behavior in GaAs two-dimensional holes below 30 mK. *Phys. Rev. Lett.* **98**(22), 226801 (2007).

[102] Lilly, M. P., Reno, J. L., Simmons, J. A., Spielman, I. B., Eisenstein, J. P., Pfeiffer, L. N., West, K. W., Hwang, E. H., and Das Sarma, S. Resistivity of dilute 2D electrons in an undoped GaAs heterostructure. *Phys. Rev. Lett.* **90**(5), 056806 (2003).

[103] Punnoose, A. and Finkel'stein, A. M. Metal-insulator transition in disordered two-dimensional electron systems. *Science* **310**(5746), 289–291 (2005).

[104] Meir, Y. Percolation-type description of the metal-insulator transition in two dimensions. *Phys. Rev. Lett.* **83**(17), 3506 (1999).

[105] Das Sarma, S. and Hwang, E. H. Charged impurity-scattering-limited low-temperature resistivity of low-density silicon inversion layers. *Phys. Rev. Lett.* **83**(1), 164 (1999).

[106] Pushkarov, D. I. Quantum diffusion. *Cond-mat* **0310283** (2003).

[107] Kim, E. and Chan, M. H. W. Probable observation of a supersolid helium phase. *Nature* **427**(6971), 225–227 (2004).

[108] Rittner, A. S. C. and Reppy, J. D. Disorder and the supersolid state of solid ^{4}He. *Phys. Rev. Lett.* **98**(17), 175302 (2007).

[109] Basko, D. M., Aleiner, I. L., and Altshuler, B. L. On the problem of many-body localization. *Cond-mat* **0602510** (2006).

[110] Ramakrishnan, T. V. Private communication (2007).

[111] van Houten, H., Beenakker, C. W. J., and Staring, A. A. M. Coulomb-blockade oscillations in semiconductor nanostructures. *Cond-mat* **0508454** (2005).

[112] Shepelyansky, D. L. Coherent propagation of two interacting particles in a random potential. *Phys. Rev. Lett.* **73**(19), 2607 (1994).

[113] Cockayne, E. and Elser, V. Energetics of point defects in the two-dimensional Wigner crystal. *Phys. Rev. B* **43**(1), 623 (1991).

[114] Shklovskii, B. I. Variable-range hopping conductivity in a strong magnetic field. *JETP Lett.* **36**, 51 (1982).

[115] Pepper, M. Conductance oscillations in a two-dimensional impurity band. *J. Phys. C: Solid State Phys.* **12**(16), L617–L625 (1979).

[116] Smith, C. G. Low-dimensional quantum devices. *Rep. Prog. Phys.* **59**(2), 235–282 (1996).

[117] Kastner, M. A. The single-electron transistor. *Rev. Mod. Phys.* **64**(3), 849 (1992).

[118] Siegert, C., Ghosh, A., Pepper, M., Farrer, I., and Ritchie, D. A. The possibility of an intrinsic spin lattice in high-mobility semiconductor heterostructures. *Nature Phys.* **3**(5), 315–318 (2007).

[119] Freyn, A. and Pichard, J.-L. Effect of measurement probes upon the conductance of an interacting nanosystem: Detection of an attached ring by nonlocal many body effects. *Phys. Rev. Lett.* **98**(18), 186401 (2007).

[120] Komiyama, S., Hirai, H., Ohsawa, M., Matsuda, Y., Sasa, S., and Fujii, T. Inter-edge-state scattering and nonlinear effects in a two-dimensional electron gas at high magnetic fields. *Phys. Rev. B* **45**(19), 11085 (1992).

[121] Grill, R. and Döhler, G. H. Effect of charged donor correlation and Wigner liquid formation on the transport properties of a two-dimensional electron gas in modulation δ -doped heterojunctions. *Phys. Rev. B* **59**(16), 10769 (1999).

[122] Stopa, M. Single-mode quantum wires. *Phys. Rev. B* **53**(15), 9595 (1996).

[123] Wei, Y. Y., Weis, J., Klitzing, K. v., and Eberl, K. Edge strips in the quantum Hall regime imaged by a single-electron transistor. *Phys. Rev. Lett.* **81**(8), 1674 (1998).

[124] Ilani, S., Yacoby, A., Mahalu, D., and Shtrikman, H. Microscopic structure of the metal-insulator transition in two dimensions. *Science* **292**(5520), 1354–1357 (2001).

[125] Zhitenev, N. B., Fulton, T. A., Yacoby, A., Hess, H. F., Pfeiffer, L. N., and West, K. W. Imaging of localized electronic states in the quantum Hall regime. *Nature* **404**(6777), 473–476 (2000).

[126] Ilani, S., Martin, J., Teitelbaum, E., Smet, J. H., Mahalu, D., Umansky, V., and Yacoby, A. The microscopic nature of localization in the quantum Hall effect. *Nature* **427**(6972), 328–332 (2004).

[127] Martin, J., Ilani, S., Verdene, B., Smet, J., Umansky, V., Mahalu, D., Schuh, D., Abstreiter, G., and Yacoby, A. Localization of fractionally charged quasi-particles. *Science* **305**(5686), 980–983 (2004).

[128] Topinka, M. A., LeRoy, B. J., Shaw, S. E. J., Heller, E. J., Westervelt, R. M., Maranowski, K. D., and Gossard, A. C. Imaging coherent electron flow from a quantum point contact. *Science* **289**(5488), 2323–2326 (2000).

[129] Topinka, M. A., LeRoy, B. J., Westervelt, R. M., Shaw, S. E. J., Fleischmann, R., Heller, E. J., Maranowski, K. D., and Gossard, A. C. Coherent branched flow in a two-dimensional electron gas. *Nature* **410**(6825), 183–186 (2001).

[130] Blanter, Y. M. and Büttiker, M. Shot noise in mesoscopic conductors. *Phys. Rep.* **336**(1-2), 1–166 (2000).